

INELASTIC PROTON SCATTERING FROM  $^{138}\text{Ba}$  AND  $^{144}\text{Sm}$   
AND ITS MICROSCOPIC INTERPRETATION

Thesis for the Degree of Ph. D.  
MICHIGAN STATE UNIVERSITY  
DUANE CLARK LARSON  
1972



This is to certify that the

thesis entitled

*inelastic scattering from  $^{138}\text{Ba}$   
and  $^{144}\text{Sm}$  and its microscopic interpretation*

presented by

*Duane Clark Larson*

has been accepted towards fulfillment  
of the requirements for

*Ph. D.* degree in *Physics*

*B. H. Wildenthal*

Major professor

Date *Nov. 6, 1972*



**PLACE IN RETURN BOX** to remove this checkout from your record.  
**TO AVOID FINES** return on or before date due.  
**MAY BE RECALLED** with earlier due date if requested.

DATE DUE	DATE DUE	DATE DUE

## ABSTRACT

### INELASTIC PROTON SCATTERING FROM $^{138}\text{Ba}$ and $^{144}\text{Sm}$ AND ITS MICROSCOPIC INTERPRETATION

By

Duane Clark Larson

Differential cross sections for elastic and inelastic scattering of 30 MeV protons by  $^{138}\text{Ba}$  and  $^{144}\text{Sm}$  have been measured. The total resolution for the inelastic peaks was 7-10 keV FWHM, which permitted the observation of 20 excited states in  $^{138}\text{Ba}$  and 18 states in  $^{144}\text{Sm}$  below  $E_x=3.4$  MeV, and measurement of excitation energies accurate to 2 keV or less for these states. Based on characteristic shapes derived from angular distributions to states of known  $J^\pi$ , spin-parity assignments are made for the majority of the observed states. Collective model DWBA calculations were performed and deformation parameters extracted for all states of assigned  $J^\pi$ . Microscopic DWBA calculations which included the exchange amplitude were performed for the  $2_{1,2}^+$ ,  $4_{1,2}^+$  and  $6_{1,2}^+$  states in both nuclei, using large-basis shell model wave functions to describe the nuclear states. These wave functions also provide an excellent description of the excited states in  $^{138}\text{Ba}$ , and a good description of the energy levels in  $^{144}\text{Sm}$ , as measured in our experiments. The two-body force used in



Duane Clark Larson

The inelastic scattering calculations was obtained from a recent survey of inelastic scattering analyses. Polarization charges for the nucleons were extracted, and found to be essentially state and multipole independent. Two sets of shell model wave functions were employed for the  $^{138}\text{Ba}$  calculation, and it was found that inelastic proton scattering clearly distinguished between the two sets, thus providing a sensitive test of the wave functions. Careful consideration of the transition densities derived from the wave functions enable one to directly study the properties of the wave functions.

INELASTIC PROTON SCATTERING FROM  $^{138}\text{Ba}$  AND  $^{144}\text{Sm}$   
AND ITS MICROSCOPIC INTERPRETATION

By

Duane Clark Larson

A THESIS

Submitted to  
Michigan State University  
in partial fulfillment of the requirements  
for the degree of

DOCTOR OF PHILOSOPHY

Department of Physics

1972

6 79001

## ACKNOWLEDGEMENTS

I would like to thank the entire Cyclotron staff for their many kindnesses which made these experiments possible. Specific thanks are due the following people:

Dr. Stan Fox for his cool head during difficult experimental times;

Drs. Helmut Laumer and Lolo Panaggabean for standby help during data taking;

Richard Au for immeasurable computer assistance;

Norval Mercer and the machine shop staff for various favors;

Andy Kaye for procuring materials and photographs with utmost efficiency;

Professor Hugh McManus, Dr. Fred Petrovich and the rest of the theoretical group for many valuable discussions;

Julie Perkins for typing this thesis;

Dr. Barry Freedom for taking time to relate the story of DWBA theory, and many useful discussions;

My thesis advisor, Professor Sam Austin for his help in all aspects of this work, especially during the data taking and the writing of this paper;

Professor Hobson Wildenthal, whose influences are present in all aspects of this work, for introducing me to many facets of nuclear physics, especially the shell model, and for providing a home for my tractor;

My wife, Dr. Nancy Larson, for help in data taking, and frequent discussions of theoretical problems associated with this work, as well as cooking my meals;

My parents, for their continuous encouragement of my educational pursuits;

and finally, I acknowledge the financial support of the NSF, and a three year NASA Traineeship during my graduate studies.

# TABLE OF CONTENTS

	Page
ACKNOWLEDGEMENTS . . . . .	ii
LIST OF TABLES. . . . .	vi
LIST OF FIGURES . . . . .	vii
I. INTRODUCTION . . . . .	1
II. EXPERIMENTAL . . . . .	6
A. Proton Beam and Particle Detection. . . . .	6
B. Preparation of Targets. . . . .	8
C. High Resolution System. . . . .	9
III. EXPERIMENTAL RESULTS. . . . .	11
A. Energies of States in $^{138}\text{Ba}$ and $^{144}\text{Sm}$ . . . . .	11
B. Angular Distributions . . . . .	12
C. Discussion of States in $^{138}\text{Ba}$ . . . . .	14
1. $2^+$ States. . . . .	15
2. $3^-$ States. . . . .	16
3. $4^+$ States. . . . .	16
4. $6^+$ States. . . . .	19
5. Other States. . . . .	20
D. Discussion of States in $^{144}\text{Sm}$ . . . . .	21
1. $2^+$ States. . . . .	21
2. $3^-$ States. . . . .	22
3. $4^+$ States. . . . .	22
4. $6^+$ States. . . . .	23
5. Other States. . . . .	24
IV. N=82 WAVE FUNCTIONS . . . . .	26
A. Conventional Shell-Model . . . . .	26
B. Other Structure Calculations. . . . .	29
V. OPTICAL MODEL . . . . .	31

	Page
VI. DWBA THEORY. . . . .	34
A. Collective Model. . . . .	34
B. Microscopic Model . . . . .	36
1. Distorted Wave Calculations. . . . .	36
2. Spectroscopic Amplitudes. . . . .	37
3. Elements of the DWBA Formalism (Direct Amplitudes). . . . .	38
4. Transition Density. . . . .	42
5. Discussion of Selection Rules and Non-Normal Parity States . . . . .	46
VII. DISCUSSION OF RESULTS . . . . .	50
A. Comparison of Shell Model Calculations to Experiment . . . . .	50
B. Collective Model Results . . . . .	52
C. Microscopic Model Analysis . . . . .	54
1. Microscopic DWBA Calculations for <sup>138</sup> Ba . . . . .	56
2. Calculations with Other Forces. . . . .	62
3. Microscopic DWBA Calculations for <sup>144</sup> Sm . . . . .	64
VIII. CONCLUSION . . . . .	67
REFERENCES . . . . .	70
APPENDIX	
A. TABLES . . . . .	74
B. FIGURES . . . . .	81
C. COMPILATION OF EXPERIMENTAL ANGULAR DISTRIBUTIONS . . . . .	105

# LIST OF TABLES

Table		Page
1.	Energy Levels of $^{138}\text{Ba}$ and $^{144}\text{Sm}$ . . . . .	75
2.	Optical Model Parameters for $^{138}\text{Ba}(^{144}\text{Sm})$ . . . . .	76
3.	Deformation Lengths and Transition Strengths for $^{138}\text{Ba}$ and $^{144}\text{Sm}$ . . . . .	77
4.	Polarization Charges for Transitions in $^{138}\text{Ba}$ . . . . .	78
5.	Major Components of $0_1^+$ and $6_2^+$ Wave Functions Calculated with Both Interactions, and the Resulting Transition Densities. . . . .	79
6.	Comparison of Direct and Direct + Exchange Cross Sections for Various Interactions in $^{138}\text{Ba}$ . . . . .	80

## LIST OF FIGURES

Figure		Page
1.	Slit and counter arrangement of high resolution measurement-optimization-stabilization system located in the focal plane of the spectrograph. The experimental parameters are adjusted until the maximum amount of elastically scattered beam passes between the brass jaws, thus insuring minimum line widths of the groups of scattered particles along the focal plane. .	82
2.	Spectrum of $^{138}\text{Ba}(p,p')$ at 35 degrees, with resolution of about 10 keV, FWHM. The broad bumps correspond to protons which scatter from Mg and Si impurities and because of kinematic differences have planes of focus in the spectrograph. The yields of the $2^+$ state at 1436 keV and of the $3^-$ state at 2881 keV were too intense to be counted on this plate . . . . .	83
3.	Spectrum from $^{144}\text{Sm}(p,p')$ at 40 degrees, with resolution of about 7 keV, FWHM. The broad bumps under certain of the peaks correspond to protons which scatter from Mg and Si impurities, as in the $^{138}\text{Ba}$ spectrum. The yield of the $3^-$ state at 1811 keV was too intense to be counted on this plate . .	84
4.	Elastic scattering angular distributions measured for $^{138}\text{Ba}$ and $^{144}\text{Sm}$ . The curves are results of optical model calculations made with the optical model parameters of Becchetti and Greenlees (Ref. 34) . . . .	85
5.	Characteristic curves obtained by averaging our measured angular distributions from groups of states in $^{138}\text{Ba}$ and $^{144}\text{Sm}$ which had previously assigned $J^\pi$ values . . . .	86



Figure		Page
6.	States in $^{138}\text{Ba}$ which have angular distributions in agreement with the characteristic $2^+$ shape, which is the line drawn through the data. We assign all of these states $J^\pi=2^+$ with the exception of the state at 3050 keV. . . . .	87
7.	States in $^{144}\text{Sm}$ which have angular distributions in agreement with the characteristic $2^+$ shape, which is the line drawn through the data. We assign all of these states $J^\pi=2^+$ .	88
8.	States in $^{138}\text{Ba}$ and $^{144}\text{Sm}$ which have angular distributions in agreement with the characteristic $3^-$ shape, which is the line drawn through the data. We assign these states $J^\pi=3^-$ . . . . .	89
9.	States in $^{138}\text{Ba}$ which have angular distributions in agreement with the characteristic $4^+$ shape, which is the line drawn through the data. We assign all of these states $J^\pi=4^+$ .	90
10.	States in $^{144}\text{Sm}$ which have angular distributions in agreement with the characteristic $4^+$ shape, which is the line drawn through the data. We assign all of these states $J^\pi=4^+$ . . . . .	91
11.	Angular distributions for the previously assigned $6^+$ state at 2090 keV, and the weak 2201 keV member of a doublet. Both the $4^+$ and $6^+$ characteristic curves are drawn through this angular distribution. The 2324 keV state in $^{144}\text{Sm}$ has been assigned $6^+$ , but due to the rise of the data at forward angles, this state may be a close lying doublet. We assign $J=6^+$ to the 3308 keV state in $^{144}\text{Sm}$ . . . . .	92
12.	Angular distributions of states in $^{138}\text{Ba}$ for which no $J^\pi$ assignment could be made from this work. Spins of $5^+$ and $3^+$ have been suggested for the states at 2415 and 2445 keV respectively (Ref. 37). . . . .	93

Figure		Page
13.	Angular distributions of states in $^{144}\text{Sm}$ for which no $J^\pi$ assignment could be made from this work. The state at 3123 keV has been assigned $J^\pi=(7^\pm)$ in Ref. 11 . . .	94
14.	Comparison of results of shell model calculations discussed in Sec. IVA with experimentally known energy levels in $^{138}\text{Ba}$ .	95
15.	Comparison of results of shell model calculations discussed in Sec. IVA with experimentally known energy levels in $^{144}\text{Sm}$ .	96
16.	Results of collective model calculations for inelastic scattering on $^{138}\text{Ba}$ . The optical model parameters given in Table 2, Set SII were used, and both the real and imaginary parts of the optical model were deformed. The calculations shown are for the lowest $2^+$ , $3^-$ , $4^+$ and $6^+$ states . . . . .	97
17.	Results of collective model calculations for $^{144}\text{Sm}$ . The optical model parameters given in Table 2, Set SI were used, and both the real and imaginary parts of the optical model were deformed. The calculations shown are for the lowest $2^+$ , $3^-$ , $4^+$ and $6^+$ states . . . . .	98
18.	Microscopic model DWBA calculations for the inelastic scattering to the $2_1^+$ , $4_1^+$ and $6_1^+$ states in $^{138}\text{Ba}$ . The calculations are identical except for the wave functions; the left hand column employed the A=136-140 set while the A=136-145 set was used for the right hand column. Both sets of wave functions predict very similar angular distributions . . . . .	99
19.	Microscopic model DWBA calculations for the inelastic scattering to the $2_2^+$ , $4_2^+$ and $6_2^+$ states in $^{138}\text{Ba}$ . The calculations are identical except for the wave functions; the left hand column employed the A=136-140 set while the A=136-145 set was used for the right hand column. These calculations indicate that the A=136-140 set of wave functions provides the better description of the low lying states in $^{138}\text{Ba}$ . . . . .	100

20. Transition densities for the  $2_{1,2}^+$ ,  $4_{1,2}^+$  and  $6_{1,2}^+$  states in  $^{138}\text{Ba}$  calculated with both sets of wave functions. The  $2_{1,2}^+$ ,  $4_{1,2}^+$  and  $6_{1,2}^+$  densities are very similar, and predict very similar cross sections. The differences in the  $2_{1,2}^+$ ,  $4_{1,2}^+$  and  $6_{1,2}^+$  cross sections are directly related to the differences in the transition densities for these states . . . 101
21. Composition of the  $6_2^+$  transition density in  $^{138}\text{Ba}$ , calculated with both sets of wave functions. The left hand figure is calculated with the A=136-140 set while the right hand column is calculated with the A=136-145 set . . . . . 102
22. Microscopic model DWBA calculations for inelastic scattering to the  $3_1^+$  and  $5_1^+$  states in  $^{138}\text{Ba}$  calculated with the A=136-140 set of wave functions. The two-body force included central, tensor and LS terms, but no collective enhancement was included. Only the Direct + Exchange calculations are shown . . . . . 103
23. Microscopic model DWBA calculations for the inelastic scattering to the  $2_{1,2}^+$ ,  $4_{1,2}^+$  and  $6_{1,2}^+$  states in  $^{144}\text{Sm}$  calculated with the A=136-145 set of wave functions. The inadequacy of the basis space is demonstrated in the calculated angular distributions for the  $2_{1,2}^+$ ,  $4_{1,2}^+$  and  $6_{1,2}^+$  states . . . . . 104

## I. INTRODUCTION

The recent interest in the  $N=82$  nuclei stems from a number of sources. Foremost among these is the observation that in a shell model picture, low-lying states in these nuclei are expected to be formed predominantly from proton configurations, the neutron shells being closed with 82 neutrons. Experimental evidence from proton<sup>(1-2)</sup> and neutron<sup>(3-5)</sup> transfer experiments confirm this expectation. Both proton stripping and pickup reactions on the  $N=82$  nuclei populate only the  $1g_{7/2}$ ,  $2d_{5/2}$ ,  $2d_{3/2}$ ,  $3s_{1/2}$ , and  $1h_{11/2}$  single particle orbitals, thus indicating that proton orbitals other than these do not play a significant role in the wave functions for states of these nuclei. Neutron pickup reactions indicate that the orbitals above the last filled neutron major shell are empty, and conversely, neutron stripping reactions populate only the orbitals above the closed major shell, thus indicating that neutron shells below this are filled. The picture of the  $N=82$  nuclei which emerges from these experiments is that of a closed 82 neutron, 50 proton core, with low-lying states in these nuclei being formed by couplings of various numbers of valence protons in the aforementioned orbitals.

The single particle nature of these nuclei has been thoroughly studied with the proton and neutron transfer reactions described previously. Isobaric analog resonance experiments<sup>(6)</sup> have been used to determine, among other things, the positions of the low-lying neutron particle-hole states, which signal the breakdown of our model. Electromagnetic decay aspects of the N=82 nuclei have been measured through  $(\beta, \gamma)$ ,<sup>(7-8)</sup>  $(n, \gamma)$ ,<sup>(9)</sup>  $(n, n' \gamma)$ <sup>(10)</sup> and  $(\alpha, xn \gamma)$ <sup>(11)</sup> studies. These studies have been useful in making precise energy level assignments, as well as often limiting the possible  $J^\pi$  assignments to a few values. The  $(\alpha, xn \gamma)$  studies have led to the observation of a series of isomeric  $6^+$  states in the even-even N=82 isotones.

Charged particle inelastic scattering studies have been limited mainly to the observation of the strongly excited states. Early inelastic scattering experiments<sup>(12)</sup> determined the positions of the first collective  $2^+$  and  $3^-$  states. The  $(p, p' \gamma)$  and  $(d, d' \gamma)$  reactions<sup>(13)</sup> on the even-even isotones were performed in an attempt to locate the positions of excited  $0^+$  states in these nuclei by observing the E0 conversion electrons emitted in the transition to the ground state. More recently, the reactions  $^{139}\text{La}(\alpha, \alpha')$ ,<sup>(14)</sup>  $^{140}\text{Ce}(\alpha, \alpha')$ ,<sup>(14)</sup>  $^{141}\text{Pr}(\alpha, \alpha')$ ,<sup>(15)</sup>  $^{138}\text{Ba}(\alpha, \alpha')$ ,<sup>(16)</sup>  $^{144}\text{Sm}(\alpha, \alpha')$ ,<sup>(17)</sup>  $^{144}\text{Sm}(p, p')$ ,<sup>(17)</sup> and  $^{144}\text{Sm}(h, h')$ <sup>(18)</sup> have been used to study the collective nature of the strongly excited states in these nuclei. The angular distributions

obtained from the latter five reactions were analyzed with the standard collective model formalism<sup>(19)</sup> and from that work  $J^\pi$  assignments were made, and deformation parameters  $\beta_L$  extracted. The  $^{139}\text{La}$  and  $^{140}\text{Ce}$  experiments have also been analyzed with the collective model approach, and in addition, microscopic calculations have been performed using a Gaussian two-body interaction and zero-order pseudo-spin orbit wave functions to describe the nuclear states. However, since alpha particles are strongly absorbed near the surface of the nucleus, only the tails of the wave functions are important and this reaction is thus rather insensitive to the details of the wave functions.

In this paper we present results from inelastic proton scattering experiments performed at a bombarding energy of 30 MeV on  $^{138}\text{Ba}$  and  $^{144}\text{Sm}$ . Use of the high resolution system developed at Michigan State by Blosser, et al.<sup>(20)</sup> resulted in a total energy resolution for the inelastic peaks of typically 7-10 keV FWHM. Excitation energies accurate to 2 keV were extracted and found to be in good agreement with those obtained by other methods. Using empirical characteristic shapes derived from angular distributions to known states, we assign spins and parities to the majority of the observed states.

Most previous microscopic DWBA calculations for inelastic scattering have been restricted to regions of the periodic table where particle-hole<sup>(21,22)</sup> or simple

shell-model wave functions<sup>(23,24)</sup> were adequate for the description of the nuclear states. A second aspect of this work, in addition to spectroscopy, was to attempt to determine if large basis shell model wave functions can account for (p,p') measurements on nuclei with several valence nucleons. To this end, we have modified the Oak Ridge-Rochester shell-model codes<sup>(25)</sup> to calculate the necessary structure amplitudes in a form convenient for DWBA calculations. By using two sets of shell-model wave functions<sup>(26,27)</sup> in the DWBA calculations for  $^{138}\text{Ba}$ , we show that inelastic proton scattering provides a sensitive test for these wave functions, and allows us to choose one set as preferable to the other. Information concerning the structure of the wave functions can be extracted by a detailed consideration of the resulting transition densities.

Use of a model proposed by Atkinson and Madsen,<sup>(28)</sup> and McManus<sup>(29)</sup> for including effects due to excitations of nucleons out of the core enables us to extract information concerning the polarization charge of the nucleons in this mass region.

In Section II we describe the experimental details of this work, followed in Section III with an individual discussion of all states observed up to  $E_x=3.3$  MeV, and assignments of excitation energies and spin-parities, where possible. Section IV is a discussion of the shell model calculation which we use in this work, and Section V

presents the optical model parameters we obtained from our elastic scattering. Section VI outlines the relevant aspects of the DWBA theory used to analyze our angular distributions, and lastly Section VII is a discussion of the results of this experiment.



## II. EXPERIMENTAL

### A. Proton Beam and Particle Detection

The measurements were made with a 30 MeV beam of protons from the Michigan State University sector focussed cyclotron. An Enge split-pole spectrograph was used to detect the scattered particles. The amount of beam on target was monitored both with a current integrator in conjunction with a Faraday cup, and with a 5 mm thick silicon detector placed at  $60^\circ$  with respect to the incident beam. A set of removable slits located immediately prior to the spectrograph scattering chamber was used periodically to check the position of the beam on target. The typical size of the beam spot was 2 mm high by 4-5 mm wide. The entrance aperture of the spectrograph was  $2^\circ$  wide by  $1.6^\circ$  high, corresponding to a solid angle of 0.98 msr. During data accumulation this entrance aperture was the only slit between the cyclotron and the focal plane of the spectrograph. The absolute energies of the proton beams were obtained from NMR calibrations of the transport system magnets. The uncertainty in this absolute scale was  $\pm 0.1\%$ . The absolute beam energies for this experiment were 29.8 MeV for  $^{138}\text{Ba}$  and 29.9 MeV for  $^{144}\text{Sm}$ .

Angular distributions for elastic scattering and for scattering from the strong first  $2^+$  and  $3^-$  states in both nuclei were measured using a 300 micron thick solid state position sensitive detector mounted at the focal plane of the spectrograph.<sup>30</sup> Signals proportional to  $E$ , the total energy loss of the particles passing through the detector, and  $xE$ , where  $x$  is the position along the detector, were analyzed for the type of particle and its location along the detector using a two dimensional data taking program.<sup>31</sup> The  $xE$  signal was divided by the  $E$  signal, and energy vs. position spectra were displayed on a storage scope, where suitable lines were drawn defining the proton band. The computer then identified all events falling between the lines as proton events and stored them in a position spectrum. The resolution obtained with the position sensitive detector was typically 30 keV FWHM. Its charge collection efficiency was mapped by gridding the peak from the elastically scattered particles across its surface in 3 mm steps. During data accumulation, the particles to be detected were positioned in a region which had been determined to have uniform efficiency.

The remainder of the inelastic scattering data were measured with Kodak NTB 25 or 50 micron nuclear emulsions placed in the focal plane of the spectrograph. Aluminum absorbers were used to stop all particles of greater stopping power than protons. Emulsions were exposed every

$5^\circ$  between  $20^\circ$  and  $80^\circ$  for  $^{138}\text{Ba}$  and from  $12^\circ$  to  $95^\circ$  for  $^{144}\text{Sm}$ . Two exposures were made at each angle, a short exposure to obtain data from the first  $2^+$  and  $3^-$  states (for normalization purposes), and a sufficiently long exposure to obtain data with good statistics for most of the remaining states. The agreement between the position sensitive detector data and the emulsion data for the  $2^+$  and  $3^-$  states was within statistics, so the data were averaged to obtain angular distributions for these states.

#### B. Preparation of Targets

Isotopically enriched compounds of  $\text{Ba}(\text{NO}_3)_2$  (99.8%) and  $\text{Sm}_2\text{O}_3$  (95.1%) obtained from Oak Ridge National Laboratory were used in the fabrication of the targets. The desired compound was placed in a Zr boat and heated in a vacuum, causing reduction of the compound to the enriched metal and simultaneous evaporation of the metal onto the target backing, which consisted of a  $20 \mu\text{g}/\text{cm}^2$  carbon foil plus a  $3\text{--}5 \mu\text{g}/\text{cm}^2$  layer of formvar supporting the carbon. The target material was evaporated over a surface  $5/8"$  in diameter and appeared to be quite uniform. Typical target thicknesses ranged between 50 and  $300 \mu\text{g}/\text{cm}^2$ . The targets were stored and transferred under vacuum to reduce oxidation. Since complete oxidation occurred in only a few seconds for a thin  $^{138}\text{Ba}$  target, and a few minutes for a  $^{144}\text{Sm}$  target, thickness was therefore estimated

by comparing the measured elastic scattering to optical model predictions for the scattering.

The observed contaminants in the targets were carbon, oxygen, magnesium, and silicon, determined from analysis of the inelastic scattering spectrum.

### C. High Resolution System

The emulsion data were all taken using the high resolution system developed at Michigan State by Blosser, et al.<sup>(20)</sup> This system relies on dispersion matching,<sup>(32)</sup> kinematic compensation, and a feedback system which compensates for possible drift of any magnets in the cyclotron-beam transport-spectrograph system. In a dispersion matched system the line width of the scattered particles at the focal plane of the spectrograph is nearly independent of the energy spread of the incident beam. This is accomplished by using the focussing and dispersive elements of the beam transport system to adjust the dispersion of the beam on target to match the dispersion of the spectrograph. Kinematic compensation corrects for the change in energy of the scattered particles across the finite entrance slit width, which arises from recoil of the target nucleus. This is accomplished by shifting the kinematic focal plane from its zero order position (position for scattering from an infinitely heavy target nucleus). The approximate beam transport quadrupole settings for

dispersion matching and correct position of the focal plane for kinematic compensation are calculated for a given reaction via a computer code.<sup>(33)</sup> Final minimization of the line width of the scattered protons is accomplished by using a stepped slit and detector device located at the focal plane of the spectrograph and illustrated in Figure 1. Fractional transmission of the elastically scattered protons through the 4 mil slit is maximized (thus minimizing the line width) by adjusting the dispersive elements of the beam transport system and other parameters of the experimental setup. After minimization of the line width, this device serves as a feedback system, controlling the spectrograph magnet to keep the elastically scattered protons centered on the transmission slit. This insures that the scattered protons remain at fixed points on the focal plane, independent of drifts in the system. Using this high resolution system we routinely obtained resolutions of 7-10 keV FWHM at 30 MeV incident proton energy for the inelastically scattered particles. Figure 2 shows a spectrum obtained from  $^{138}\text{Ba}$  at a laboratory angle of  $35^\circ$ , and Figure 3 shows a spectrum from  $^{144}\text{Sm}$  obtained at  $40^\circ$ . Typical beam currents on target were 100 na for  $^{138}\text{Ba}$  (target limited) and 900 na for  $^{144}\text{Sm}$ .

### III. EXPERIMENTAL RESULTS

#### A. Energies of States in $^{138}\text{Ba}$ and $^{144}\text{Sm}$

The high resolution system described in the previous section, in conjunction with nuclear emulsions, was used to obtain precise energies for 20 excited states in  $^{138}\text{Ba}$  and 18 states in  $^{144}\text{Sm}$  below  $E_x = 3.4$  MeV.

Peak centroids and intensities were extracted from the spectra obtained from the scanned emulsions at each angle. This was done with an automatic peak-fitting program, which aided in removing ambiguities in the background subtraction and afforded a consistent method of separating members of close lying doublets. The final adjustments to the basic energy calibration of the spectrograph were determined by fitting certain strong, isolated peaks in our (p,p') spectra to excitation energies previously determined for these levels by Ge(Li) spectrometer studies of gamma rays emitted in ( $\beta$ , $\gamma$ ) experiments. These calibration energies, along with their errors, are noted in Table 1. This calibration of the spectrograph was then used for interpolation and extrapolation to other excitation energies. These results enabled us to assign an excitation energy to each observed peak at each angle, provided the peak was not obscured by a contaminant. The

extracted energies were averaged over all angles of observation, and the mean error in the centroid was calculated. The energies we have assigned to levels in  $^{138}\text{Ba}$  and  $^{144}\text{Sm}$ , along with the combined random and systematic errors, are listed in Table 1. These energies are in excellent agreement with energies from  $(\beta, \gamma)$  work on  $^{138}\text{Ba}$  and  $(\alpha, 2n\gamma)$  work on  $^{144}\text{Sm}$ .

### B. Angular Distributions

Angular distributions have been measured for 18 of the 20 states observed in  $^{138}\text{Ba}$  and 15 of the 18 observed states in  $^{144}\text{Sm}$ , and for elastic scattering from both nuclei.

The elastic scattering angular distributions from  $^{138}\text{Ba}$  and  $^{144}\text{Sm}$  are shown in Figure 4. The curves through the data are optical model calculations using parameters of Becchetti and Greenlees.<sup>(34)</sup> The elastic angular distribution data were normalized to the optical model calculations to obtain an absolute normalization. A comparison with calculations using other sets of optical model parameters<sup>(35)</sup> results in an estimate of 10% uncertainty in the experimental absolute cross sections. Relative uncertainties in our  $(p, p')$  cross sections arising from scanning errors, monitoring errors and statistical errors are typically 7%.

To facilitate a systematic analysis of our (p,p') data we derived from our data empirical characteristic shapes for  $2^+$ ,  $3^-$ ,  $4^+$ , and  $6^+$  angular distributions in the following way. Examination of angular distributions for the known  $2^+$  states in both  $^{138}\text{Ba}$  and  $^{144}\text{Sm}$  reveals that they all have essentially the same shape. Using this fact, one average  $2^+$  shape was obtained from all of the known  $2^+$  distributions in both nuclei. This characteristic  $2^+$  shape was then used as a standard and compared to angular distributions for states of unknown  $J^\pi$ . Identical techniques were applied to the angular distributions of all assigned  $3^-$ ,  $4^+$ , and  $6^+$  states in these nuclei to obtain  $3^-$ ,  $4^+$ , and  $6^+$  characteristic shapes. The resulting empirical characteristic shapes for  $2^+$ ,  $3^-$ ,  $4^+$ , and  $6^+$  angular distributions are compared in Figure 5. We emphasize that the characteristic shape for a given  $J^\pi$  is an average of angular distribution data for all known states of that  $J^\pi$  from both nuclei. The states used in the determination of the empirical shapes are noted in Table 1. The angular distribution data, along with the characteristic shape of the appropriate  $J^\pi$  which best approximates the data, are shown in Figures 6 through 11. The remaining states, whose angular distributions are not similar to any of the characteristic shapes, are shown in Figures 12 and 13. They may be grouped into two classes; either they are very weakly



excited in this reaction, or they peak farther out in angle than the  $6^+$  states, implying they may be high spin states.

As explained in Sec. VIB5, direct DWBA theory would predict L-transfers of 2, 3, 4, and 6 for transitions from a  $0^+$  ground state to states with  $J^\pi=2^+, 3^-, 4^+$ , and  $6^+$ , respectively. There are sufficient differences between the characteristic shapes, as seen in Figure 5, to allow us to uniquely assign an L-transfer of 2, 3, 4, or 6 to the majority of the observed transitions. This in turn leads to assignments of  $J^\pi=L$ , with parity  $(-)^L$ , if it is assumed that non-normal parity states are weakly excited. In Sec. VIB5 we discuss the evidence which indicates that this assumption is valid. For example, an angular distribution for a state of unknown  $J^\pi$  which matches the  $4^+$  characteristic shape has an L-transfer of 4. This in turn leads to a  $J^\pi$  assignment of  $4^+$ , and not the non-normal parity  $3^+$  or  $5^+$ , as direct DWBA theory would also allow.

Our assignments for the spin and parity of excited states we observe in  $^{138}\text{Ba}$  and  $^{144}\text{Sm}$ , based on the agreement of the measured angular distributions with the empirical characteristic shapes, are given in Table 1.

### C. Discussion of States in $^{138}\text{Ba}$

To organize the discussion of our experimental results, it is convenient to divide the levels which we observe into groups, each group being identified by its appropriate  $J^\pi$  assignment.

### 1. $2^+$ States (Figure 6)

The states at 1436, 2218, 2639, 3339, and 3368 keV are all in good agreement with the  $2^+$  characteristic shape; we thus assign  $J^\pi=2^+$  to these states. The state at 1436 keV is firmly established as  $2^+$  from Coulomb excitation,<sup>(36)</sup> conversion coefficient measurements,<sup>(37)</sup> and  $(\alpha,\alpha')$  inelastic scattering.<sup>(16)</sup> The state at 2218 keV is observed to have a strong decay branch to the ground state in neutron capture<sup>(9)</sup> and  $(\beta,\gamma)$ <sup>(7-8,37)</sup> decay experiments. This limits the spin to 1 or 2. Achterberg, et al.<sup>(37)</sup> assign positive parity to this state from conversion coefficient measurements. Thus our assignment of  $J^\pi=2^+$  is consistent with previous data. The level at 2639 keV, observed in  $(n,\gamma)$ <sup>(9)</sup> and  $(\beta,\gamma)$ <sup>(7-8)</sup> studies, also has a strong decay branch to the ground state, thus limiting its spin to  $J=1,2$ . However, a log ft value of 7.4 for  $\beta$  decay from the  $J^\pi=3^-$  state of  $^{138}\text{Cs}$  given by Carraz, et al.<sup>(8)</sup> eliminates  $J=1$ . The two levels at 3339 and 3368 keV also decay directly to the ground state, limiting their spins to  $J=1,2$ . Angular distributions from  $(\alpha,\alpha')$  studies<sup>(16)</sup> also suggest a spin of  $J=2$  for these states. The angular distribution for the state we observe at 3050 keV is not in agreement

with the  $2^+$  characteristic shape at forward angles, thus we leave it unassigned. Hill and Fuller<sup>(7)</sup> assign  $J=1,2$  to this state.

## 2. $3^-$ States (Figure 8)

The only  $3^-$  state we observe in  $^{138}\text{Ba}$  is the one previously assigned<sup>(12,16)</sup> at 2881 keV. It is the strongest state in the  $(p,p')$  spectrum, and is strongly populated in  $(d,d')$ <sup>(13)</sup> and  $(\alpha,\alpha')$ <sup>(16)</sup> experiments and in  $(n,\gamma)$ <sup>(9)</sup> studies, where it decays strongly to the  $2^+$  state at 1436 keV.

## 3. $4^+$ States (Figure 9)

The states at 1898, 2308, 2584, 2779, and 3156 keV have angular distributions which are in good agreement with the characteristic  $4^+$  shape; we assign  $J^\pi=4^+$  to these states. The level at 1898 keV is established as  $4^+$  from  $(\alpha,\alpha')$ <sup>(16)</sup> angular distributions,  $(d,^3\text{He})$ <sup>(2)</sup> measurements which suggest an assignment of  $4^+$  or  $6^+$ , and conversion coefficient<sup>(37)</sup> studies which, when combined with the  $(d,^3\text{He})$  work, limit the spin to  $4^+$ .

The state at 2308 keV is assigned  $J^\pi=3^+, 4^+$  from conversion coefficient studies of Achterberg, et al.<sup>(37)</sup> A  $J=3,4$  assignment has also been suggested by  $(n,\gamma)$ <sup>(9)</sup> and  $(\beta,\gamma)$ <sup>(7)</sup> studies based

on the strong decay to both the first  $2^+$  and  $4^+$  states. Since non-normal parity states such as  $3^+$  are very weakly excited in inelastic scattering on heavy nuclei, we assign  $J^\pi=4^+$  to this state, which is also the suggested assignment from  $(\alpha, \alpha')$  <sup>(16)</sup> studies.

Hill and Fuller <sup>(7)</sup> and Mariscotti, et al. <sup>(9)</sup> observe a state in the vicinity of the state we see at 2584 keV. Hill and Fuller limit the spin of this state to  $J=1,2$  on the basis of a gamma ray branch to the ground state. However, the angular distribution we measure has a  $4^+$  shape. Thus, we believe there are two distinct levels in this vicinity since the state seen by Hill and Fuller is clearly not a  $4^+$  by virtue of the gamma ray to the ground state, and ours is not a  $J=1$  or  $2$  by virtue of the angular distribution. It is informative to consider ratios of intensities of two gamma rays depopulating this level, as measured by Hill and Fuller in their  $(\beta, \gamma)$  work and Mariscotti, et al. in their  $(n, \gamma)$  studies.

$$\frac{I(2583 \rightarrow 1436)}{I(2583 \rightarrow 0)} = \sim 7.8 \quad (n, \gamma)$$

$$\frac{I(2583 \rightarrow 1436)}{I(2583 \rightarrow 0)} = \sim 2.3 \quad (\beta, \gamma)$$

$$\text{Thus } \frac{(n,\gamma)}{(\beta,\gamma)} = \sim 3.3$$

Similar ratios for the 2583-2218 keV transition relative to the ground state transition are also in the ratio of  $\sim 3:1$ . The non-equality of these ratios can be taken as an indication that the  $(n,\gamma)$  and  $(\beta,\gamma)$  experiments are populating two levels with different intensities in the vicinity of 2583 keV. In addition, Hill and Fuller see a broadening of the gamma ray line connecting their state at 2583 keV with the 2445 keV state. They attribute this to the decay of the 2445 keV to the 2307 keV state, but we suggest this could also be due to a state at 2584 keV decaying to the 2445 keV state. The broadened decay line they observe would then correspond not to two but to three different transitions. We will find in Sec. VIIA that the shell model predicts a  $1^+-4^+$  doublet near this energy, which would be in excellent agreement with experimental observation. A  $1^+$  state would decay to ground via an M1 transition, but since it is a non-normal parity state we would not expect to populate it strongly in  $(p,p')$ . The angular distribution we measure for this doublet would then assume the shape characteristic of the  $4^+$  member of the doublet.

The state at 2779 keV is observed in  $(\beta, \gamma)$ ,<sup>(7)</sup> but not  $(n, \gamma)$ <sup>(9)</sup> work and decays to both the first excited  $2^+$  and  $4^+$  levels, thus limiting its spin to  $J=2, 3, 4$ . It may also correspond to the state at 2.79 MeV in  $(d, {}^3\text{He})$ <sup>(2)</sup> experiments.

The state at 3156 keV which we observe is probably not the same state reported by Hill and Fuller<sup>(7)</sup> at 3164 keV, since the 8 keV difference in energies is well outside the combined errors. However, they assign spin limits of  $J=2, 3, 4$  to their state based on its decay to the first excited  $2^+$  and  $4^+$  states. These two experiments are the only ones which report a state near this energy.

#### 4. $6^+$ States (Figure 11)

We assign  $J^\pi=6^+$  to the state at 2090 keV, and a tentative  $(6^+)$  to the level at 2201 keV. Angular distributions for known  $6^+$  states are scarce in the literature. We have obtained an angular distribution for the state at 2090 keV, which has been assigned  $6^+$  by Carraz, et al.<sup>(8)</sup> on the basis of its measured half life of 0.8  $\mu\text{sec}$ . This assignment is consistent with systematics of  $6^+$  states in  $N=82$  nuclei; isomeric  $6^+$  states have been identified<sup>(38)</sup> in all even-even isotones from  ${}^{134}\text{Te}$  to  ${}^{146}\text{Gd}$ . A  $6^+$  assignment is also consistent with the absence

of this state in the  $(n,\gamma)$  <sup>(9)</sup> work, and its negligible feeding in the  $\beta$  decay of the  $3^-$  ground state of  $^{138}\text{Cs}$ .

The state at 2201 keV is the subject of some controversy. Carraz, et al. <sup>(8)</sup> propose that this state has  $J^\pi=(5^-)$ , while Achterberg, et al. <sup>(37)</sup> propose  $J^\pi=(4^+,5^+)$ , based on the measurement of  $\log ft$  values from the decay of  $^{138\text{m,g}}\text{Cs}$  and the assumption of  $J^\pi=3^-, (6^-)$  for the ground and isomeric states respectively of  $^{138}\text{Cs}$ . This state is quite weak in our spectra, and not well resolved from the strong  $2^+$  at 2218 keV. Our angular distribution for this state is not inconsistent with any of these tentative assignments. Both the  $4^+$  and  $6^+$  characteristic shapes are drawn through the angular distribution for this state in Figure 11. We would favor a  $(6^+)$  assignment for this state, based on the predictions of shell model calculations, and to some extent, on the shape of the angular distribution.

##### 5. Other States (Figure 12)

We make no  $J^\pi$  assignments for the states we observe at 2415, 2445, 3254, and 3285 keV. The transitions to these states are all very weak, the largest cross section at any angle being less than

10  $\mu\text{b/sr}$ . Achterberg, et al.<sup>(37)</sup> have assigned  $J = 3^+$  to the state at 2445 keV, based on angular correlation and conversion-coefficient measurements. They also suggest a  $J^\pi = 5^+$  assignment for the state at 2415, based on log ft values of the  $\beta$  decay feeding it from  $^{138\text{m,g}}\text{Cs}$ . Our angular distributions for these states, by virtue of their magnitude, support non-normal parity assignments. The two remaining states at 3254 and 3285 keV are not seen in previous work on this nucleus, and our angular distributions do not shed any light on possible  $J^\pi$  assignments for them. The 2929 and 2990 keV states which were observed only at one angle are very weak and are therefore not likely to be low spin normal parity states. Hill and Fuller<sup>(7)</sup> suggest spins of  $J=1,2$  and  $1,2,3,4$  respectively for these states.

#### D. Discussion of States in $^{144}\text{Sm}$

##### 1. $2^+$ States (Figure 7)

We assign  $J^\pi = 2^+$  to the states at 1661, 2423, and 2800 keV. The 1661 keV level is the first excited state in  $^{144}\text{Sm}$ ; its  $J^\pi$  is firmly established from Coulomb excitation,<sup>(39)</sup>  $(\beta, \gamma)$ <sup>(40)</sup> studies and  $(\alpha, \alpha')$  and  $(p, p')$ <sup>(17)</sup> experiments. Barker and Hiebert<sup>(17)</sup> observe a  $2^+$  state at  $2.45 \pm 0.02$  MeV



via  $(p,p')$  and  $(\alpha,\alpha')$  reactions which we assume corresponds to our level at 2423 keV. The state at 2800 keV has been assigned  $J^\pi=2^+$ , from comparison of its angular distribution with the  $2^+$  characteristic shape. It has also been observed weakly in the  $\beta^+$  decay<sup>(40)</sup> of the  $1^+$  ground state of  $^{144}\text{Eu}$ .

## 2. $3^-$ States (Figure 8)

We assign  $J^\pi=3^-$  to the states at 1811 and 3227 keV. The state at 1811 keV is well established to have  $J=3^-$  from  $(\alpha,\alpha')$  and  $(p,p')$  experiments,<sup>(17)</sup> and is the strongest state observed in our  $^{144}\text{Sm}$  spectra. The angular distribution of the previously unobserved state at 3227 keV is very similar to that of the 1811 keV state, as well as the angular distribution for the collective  $3^-$  state in  $^{138}\text{Ba}$ . On this basis we assign the 3227 keV state  $J^\pi=3^-$ .

## 3. $4^+$ States (Figure 10)

We assign  $J^\pi=4^+$  to the states at 2191, 2588, 2883, and 3020 keV on the basis of agreement of their angular distributions with the  $4^+$  characteristic shape. The level at 2191 keV has previously been assigned  $J^\pi=4^+$  on the basis of gamma ray systematics,<sup>(38)</sup> and recent  $(\alpha,\alpha')$  and  $(p,p')$  experiments<sup>(17)</sup> verify this assignment. We assume that this is the level at  $2.21 \pm 0.02$  MeV observed in

(d,d') and (p,p') studies.<sup>(13)</sup> The states at 2588, 2883, and 3020 keV have not been previously reported. They are in good agreement with the characteristic  $4^+$  shape, with the possible exception of the 3020 keV state, which falls off somewhat too rapidly for angles larger than  $50^\circ$ . These  $4^+$  assignments are consistent with the fact that Kownacki, et al.<sup>(11)</sup> have not observed these states in the  $^{142}\text{Nd}(\alpha, 2n)^{144}\text{Sm}$  reaction which preferentially populates states with  $J \geq 8$ . Studies of the  $\beta$  decay of the  $^{144}\text{Eu}$   $1^+$  ground state<sup>(40)</sup> also show no evidence for levels at these energies, which is in agreement with our  $4^+$  assignments since population of  $4^+$  states via this decay would be unique second forbidden.

#### 4. $6^+$ States (Figure 11)

The Stockholm group<sup>(38)</sup> has assigned the state at 2324 keV a spin-parity of  $6^+$ , based on its lifetime of 0.88  $\mu\text{sec}$ . This agrees with systematics of  $6^+$  states in the  $N=82$  nuclei. However, our angular distribution for this state is only in qualitative agreement with the characteristic  $6^+$  shape due to the rise of the data at forward angles. This could be due to a very close-lying low spin state which would cause the experimental angular

distribution to rise at forward angles. This possibility is weakly supported by the fact that the FWHM of this peak is consistently 10-15% larger than that of other nearby peaks. We also assign  $J^\pi = 6^+$  to the previously unobserved state at 3308 keV on the basis of the shape of its angular distribution.

#### 5. Other States (Figure 13)

We make no  $J^\pi$  assignments for the states we observe at 2826, 3123, 3196, and 3266 keV. The state at 3123 keV has been assigned  $7^{(\pm)}$  by the Stockholm group<sup>(11)</sup> in their search for high spin states using the  $^{142}\text{Nd}(\alpha, 2n)^{144}\text{Sm}$  reaction and coincidence techniques. Our angular distribution for this state is consistent with a high spin state; if this is the same state seen by the Stockholm group, we would favor a  $7^-$  rather than  $7^+$  assignment. The angular distributions for the levels at 2826 and 3196 keV peak far out in angle, suggestive of a high spin state, but the Stockholm group does not place any levels at these energies. The 2800 ( $2^+$ ) and 2826 keV levels are seen as a doublet in the  $(\alpha, \alpha')$  and  $(p, p')$  work of Barker and Hiebert.<sup>(17)</sup> We also note the similarity of the 3123 and 3196 keV

angular distributions, which leads one to doubt that they are both doublets. The state at 3266 keV has not been observed previously, and is excited very weakly in the present experiment. The angular distribution for this state does not allow us to make any suggestions for its spin and parity.

#### IV. N=82 WAVE FUNCTIONS

##### A. Conventional Shell Model

As discussed in the Introduction, we have used large basis shell-model wave functions to describe the nuclear states involved in the present experiment. This section describes the details of the conventional shell model calculation<sup>(26-27)</sup> which was done with the Oak Ridge-Rochester shell model code.<sup>(25)</sup>

The basis space for the shell-model wave functions consists of the  $1g_{7/2}$  and  $2d_{5/2}$  orbits, plus one-proton excitations from this subspace into the  $3s_{1/2}$  or  $2d_{3/2}$  orbits. The two-body interaction between the valence nucleons was parameterized in terms of a modified surface delta interaction (MSDI), with the four single particle energies and the two MSDI parameters fixed by fitting to energy levels of known  $J^\pi$  in the N=82 nuclei.

Two Hamiltonians were calculated. The MSDI parameters for the first Hamiltonian were obtained by fitting to levels of known  $J^\pi$  in N=82 nuclei from  $^{136}\text{Xe}$  through  $^{145}\text{Eu}$  (A=136-145), while those for the second Hamiltonian were obtained by fitting to levels from  $^{136}\text{Xe}$  through  $^{140}\text{Ce}$  (A=136-140). The A=136-145 interaction was applicable

to both  $^{138}\text{Ba}$  and  $^{144}\text{Sm}$ , while  $A=136-140$  was designed for the lower mass  $N=82$  isotones, and hence was used only for  $^{138}\text{Ba}$ . Thus two sets of wave functions were calculated for  $^{138}\text{Ba}$ , but only one set for  $^{144}\text{Sm}$ . The basis space was the same for all calculations; only the parameters of the Hamiltonian differed.

The basic difference between the two Hamiltonians is the  $g_{7/2}-d_{5/2}$  single particle energy splitting, which increased from 500 keV for the  $A=136-145$  interaction to 900 keV for the  $A=136-140$  interaction. It is found that the eigenvalues and eigenvectors calculated with the  $A=136-140$  interaction yield better agreement with experimentally known spectra, pickup and stripping spectroscopic factors and electromagnetic data for the lower  $N=82$  isotones than do those calculated with the  $A=136-145$  interaction. In particular, the  $A=136-140$  calculations are in excellent agreement<sup>(27)</sup> with recent data on  $^{133}\text{Sb}$  and  $^{134}\text{Te}$ , the one and two proton  $N=82$  isotones, although levels from these nuclei were not included in the search procedure which fixed the parameters of the Hamiltonian. It is reasonable that the  $A=136-145$  Hamiltonian might give poorer results for the lighter  $N=82$  isotones. For the upper  $N=82$  isotones, the effects of the limited basis space appear to be important. For example  $^{144}\text{Sm}$ , which has 12 valence protons, effectively has a basis space consisting of two holes in the  $g_{7/2}-d_{5/2}$

orbits and one-particle excitations out of these orbits. The physical low-lying states of  $^{144}\text{Sm}$  presumably have substantial amplitudes in their wave functions for configurations outside of the allowed basis space, such as  $(1h_{11/2})^2$ ,  $(2d_{3/2})^2$  and  $(3s_{1/2})^2$ . Including these states in the searching procedure which determines the parameters of the  $A=136-145$  Hamiltonian could well distort the parameters to compensate for components outside of the basis space. This would in turn decrease the accuracy of the calculations in the lower isotones. In light of this, the superiority of results calculated for  $^{138}\text{Ba}$  with the  $A=136-140$  interaction over those calculated with the  $A=136-145$  interaction is expected. Moreover, it is expected that the best results calculated for  $^{138}\text{Ba}$  should be superior to the best for  $^{144}\text{Sm}$ , since the basis space is more complete for  $A \leq 140$ . We have used both the  $A=136-140$  and  $A=136-145$  sets of wave functions in the DWBA calculations for  $^{138}\text{Ba}$ , to see if inelastic proton scattering can identify one set of wave functions as definitively better than the other. Only the  $A=136-145$  interaction was used in the  $^{144}\text{Sm}$  calculation, as previously noted. With the basis space used in this calculation, states in  $^{138}\text{Ba}$  have between 50 and 220 components in their wave functions, while states in  $^{144}\text{Sm}$  have between 10 and 45 components. The notation used to discuss the different states will be  $J_i^\pi$ , where  $i$  refers to the first or second excited state of spin and parity  $J^\pi$ .

## B. Other Structure Calculations

Properties of the  $N=82$  nuclei have also been calculated by methods other than the conventional shell model approach of Wildenthal.<sup>(26)</sup> Rho<sup>(41)</sup> performed a two-quasiparticle calculation for the even  $N=82$  nuclei, employing a Gaussian form as the residual nucleon-nucleon interaction. At the time of that work, the single particle energies needed in the calculation were not experimentally known. The results of this calculation are in qualitative agreement with experiment, but no  $0^+$  or  $6^+$  levels were calculated. In a later calculation, Waroquier and Hyde<sup>(42)</sup> used an approach similar to Rho, but employed the inverse gap equation technique<sup>(43)</sup> to obtain the single particle energies for their calculation. In addition they calculated the  $0^+$  and  $6^+$  states and in general obtained good agreement with existing data. Comparisons of their calculated energy levels and those of the conventional shell model which we use in this work are given in Ref. 42.

A new coupling scheme, developed by Hecht and Adler,<sup>(44)</sup> and employed by Baker and Tickle,<sup>(14)</sup> Baer, et al.<sup>(15)</sup> and Jones, et al.<sup>(2)</sup> in their work on  $N=82$  nuclei, predicts energy levels in good agreement with our experimental results for  $^{138}\text{Ba}$ . This pseudo spin-orbit coupling scheme takes advantage of the fact, observed in the shell-model calculation,<sup>(26)</sup> that for the  $N=82$  nuclei each group of levels with seniority  $v$  has some of these



levels depressed in energy. Calculations performed<sup>(2)</sup> with this coupling scheme and using a basis space very similar to that of Wildenthal result in wave functions with at most 23 components. It is encouraging that this scheme, with its apparent simplicity, is able to reproduce the salient features of the conventional shell-model which we have employed in this work. A comparison of the energy levels predicted by the pseudo spin-orbit scheme and the conventional shell model are given for  $^{138}\text{Ba}$  in Ref. 2. This coupling scheme also predicts approximate selection rules for relative strengths of excited states observed in inelastic scattering. This will be discussed further in Sec. VIB5.

## V. OPTICAL MODEL

Essential ingredients in any DWBA calculation are the optical model parameters which describe the elastic scattering in the entrance and exit channels. A number of optical model parameter studies<sup>(34-35,45)</sup> have been made for 30 MeV protons incident on nuclei with A between 40 and 208. From these parameterization studies, formulae result which allow one to interpolate the "best fit" parameters to nuclei and energies other than those specifically used in the studies. However, there is a large gap from tin (A=120) to lead (A=208) for which very little precise elastic scattering data exists, and thus no information for the region was included in the optical model studies. It was not clear, therefore, that the parameters which these studies predict would properly account for the elastic scattering from  $^{138}\text{Ba}$  and  $^{144}\text{Sm}$ .

Fortunately, parameters predicted by two previous studies<sup>(34-35)</sup> yield results which are in very good agreement with our elastic scattering data. The optical model parameters of Becchetti and Greenlees<sup>(34)</sup> predict an elastic scattering angular distribution for  $^{138}\text{Ba}(^{144}\text{Sm})$  which results in a chi square per point between theory and

experiment of 3.4 (5.3), while Set II from Satchler's analysis<sup>(35)</sup> yields a fit with  $X^2/N=4.0$  (6.0). As discussed previously in Sec. IIIB, these excellent theoretical fits allowed us to normalize our elastic angular distribution data to theory in order to obtain absolute cross sections for the inelastic scattering data. After this normalization was determined, the predicted parameters were allowed to vary in a search to obtain the optimum parameters for use in the DWBA calculations.

The optical model potential used in our analysis has the usual form

$$V(r) = -V_R(1+e^{X_R})^{-1} - i(W_{vol}-4W_{surf} \frac{d}{dx_{IM}})(1+e^{X_{IM}})^{-1} \\ + (\frac{\hbar}{m_\pi c})^2 V_{LS} \frac{1}{r} \frac{d}{dr}(1+e^{X_{LS}})^{-1} \quad (\text{Eq. 1})$$

where  $X_R = (r-r_RA^{1/3})/a_R$

$$X_{IM} = (r-r_{IM}A^{1/3})/a_{IM}$$

$$X_{LS} = (r-r_{LS}A^{1/3})/a_{LS}.$$

The Coulomb potential is that of a uniformly charged sphere with radius  $r_c A^{1/3}$ .

To obtain an optimum set of optical model parameters, three different sets were utilized as starting parameters for the searching procedure. They are 1) the set predicted

from the global optical model analysis by Becchetti and Greenlees,<sup>(34)</sup> 2) Set I, and 3) Set II from the work of Satchler<sup>(35)</sup> on 30 MeV proton elastic scattering.

The final best fit parameters for each set are presented in Table 2. The final values are all within 5% of the starting values, with the exception of the surface absorption strength in Satchler, Set I, which decreases by 15% for  $^{138}\text{Ba}$ . The total DWBA cross sections for the first  $2^+$ ,  $4^+$ , and  $6^+$  states in  $^{138}\text{Ba}$  calculated with each set of parameters are also given in Table 2. These give an indication of the sensitivity of the DWBA calculations to changes in optical model parameters. The cross section ratios for  $J=2:4:6$  are essentially constant; hence the main difference between the various sets is an overall normalization which is at most 10%. For the calculations presented in this paper, Set SII in Table 2 was chosen for  $^{138}\text{Ba}$  as it gave the smallest  $\chi^2/N$ , and resulted in total cross sections intermediate in value between BG and SI. The  $^{144}\text{Sm}$  calculations were done with Set SI.

## VI. DISTORTED WAVE BORN APPROXIMATION (DWBA) THEORY

### A. Collective Model DWBA

We have performed conventional collective model<sup>(19)</sup> DWBA calculations, deforming both the real and imaginary terms of the optical model potential. This type of analysis has been thoroughly studied for 30 MeV (p,p') reactions.<sup>(46)</sup> We have extracted deformation parameters  $\beta'$  for all states which have been assigned a  $J^\pi$  value by normalizing the calculated angular distribution to the measured distribution using a chi-squared fitting program,<sup>(47)</sup> and emphasizing the forward angle data. The resulting  $\beta'$  values may be used to estimate the strength of the corresponding B(EL) transition between the ground state and the state of interest. The formalism of Bernstein<sup>(48)</sup> has been designed to describe the extraction of isoscalar transition rates from inelastic  $\alpha$  scattering. However, the method can be applied to our results if one assumes 1) that spin and isospin flip amplitudes are small, which is reasonable for this mass region, and 2) the contribution from the interior of the nucleus, which contributes to proton but not alpha inelastic scattering, can be neglected. There is some

evidence that these are reasonable assumptions, since deformation lengths  $\delta' = \beta'R'$  obtained from inelastic proton and alpha scattering are often in good agreement. (17,48)

The most accurate comparisons can be obtained for the relative strengths for a fixed  $L$  transfer in a limited mass region, since theoretical and experimental errors will tend to cancel out. In this case, the  $B(EL)$  values which this method of analysis yields will be useful as a guideline for comparison to  $B(EL)$  values predicted by nuclear structure models, such as the shell model. The isoscalar transition rates are calculated (in single particle units) from the equation (48)

$$G_L = \frac{(Z\beta_m)^2 (3+L)^2}{4\pi(2L+1)} \quad (\text{Eq. 2})$$

where  $\beta_m$ , the mass deformation parameter, is obtained from the prescription of Bernstein (48)

$$\beta'R' = \beta_m R_m \quad (\text{Eq. 3})$$

where  $\beta'$  is obtained from the relation  $\frac{\sigma_{\text{expt}}}{\sigma_{\text{thy}}} = (\beta')^2$ .

$R'$  is the imaginary radius obtained from optical model fits to elastic scattering, and  $R_m = 1.2 A^{1/3}$ , the cutoff radius for a uniform charge density model of the nucleus. The results for  $G_L$  for a more realistic Fermi charge distribution can be obtained by multiplying the result from Eq. 2 by a tabulated correction factor given

in Ref. 48. The results of this analysis will be presented in Sec. VIIB.

## B. Microscopic DWBA

### 1. Distorted Wave Calculations

The microscopic DWBA calculations were performed with the code DWBA70 written by Raynal and Schaeffer.<sup>(49)</sup> This code is based on the helicity formalism of Raynal<sup>(50)</sup> which automatically accounts for all values of orbital angular momentum  $L$  and spin angular momentum  $S$  that can be transferred in a given transition from a  $J^\pi=0^+$  ground state. The knock-on exchange term, which describes exchange between the projectile and target nucleons, is included in the scattering amplitude. Central, tensor and L-S interactions can be included in the two-body force between the projectile and target nucleon.

The cross section is defined such that

$$\frac{d\sigma}{d\Omega} = \frac{1}{2} \sum_{\sigma_i \sigma_f} f_{\sigma_f}^* f_{\sigma_i} \quad (Eq. 4)$$

where

$$f_{\sigma_f}^{M, \sigma_i} = - \frac{m}{2\pi h^2} \sum_{j_h j_p} z_{j_h j_p}^{JT} \langle \chi_{k_f \sigma_f}^{(-)} (j_p j_h) J_\mu | v | \chi_{k_i \sigma_i}^{(+)} \rangle \quad (Eq. 5)$$

1.  $\sigma_i, \sigma_f$  are the helicities of the incoming and outgoing particles, respectively.
2.  $M$  is the helicity of the residual nucleus.
3.  $\underline{k}_i, \underline{k}_f$  are the momenta of the incoming and outgoing particles, respectively.

A target nucleus with spin zero ground state is assumed, and the final state of angular momentum  $J$  is described by a particle in orbital  $j_p$  and a hole in orbital  $j_h$ .  $v$  is the two-body interaction between the projectile and target nucleons.

The quantity  $Z_{j_h j_p}^{JT}$  is the spectroscopic amplitude<sup>(51)</sup> for the transition and contains all of the nuclear structure information needed to describe the initial and final states of the target nucleus. A full description of the helicity formalism is given in Ref. 50.

## 2. Spectroscopic Amplitudes

The spectroscopic amplitudes  $Z_{j_h j_p}^{JT}$  are of major interest in this paper. The procedures used to calculate these quantities depend upon the model used to describe the states of the target nucleus. In this work the target states are described by the large basis shell model wave functions described in Sec. IVA. We have modified the Oak Ridge-Rochester shell model codes<sup>(25)</sup> to calculate the



spectroscopic amplitudes  $Z_{j_h j_p}^{JT}$  in a form convenient for DWBA calculations. The j-j coupling formalism, used by most workers performing DWBA calculations, is more familiar than the helicity formalism previously discussed. The following discussion will therefore be based on notation very similar to that of Satchler<sup>(23)</sup> and Petrovich.<sup>(52)</sup> For the direct term of the scattering amplitude, the spectroscopic amplitudes are related to the single particle matrix elements defined by Satchler.<sup>(23,24)</sup>

$$[M_L^T(j_p j_h) \delta_{S,0} + N_{L1J}^T(j_p j_h) \delta_{S,1}] \equiv M_{LSJ}^T(j_p j_h) = \frac{\sqrt{2} \hat{T} \hat{J}_I \hat{j}_p}{J_F}$$

$$* \langle \frac{1}{2} T \tau_a, \tau_b - \tau_a | \frac{1}{2} \tau_b \rangle * Z_{j_p j_h}^{JT} * \langle \ell_p j_p \frac{1}{2} || T_{LSJ}(\theta, \phi, \sigma) \tau || \ell_h j_h \frac{1}{2} \rangle$$

(Eq. 6)

where  $T_{LSJ}$  is the spin angle tensor, and  $\tau$  is the isospin operator.

### 3. Elements of the DWBA Formalism (Direct Amplitude)

The transition density can now be defined

$$F_{(r_1)}^{LSJ,T} = \sum_{j_p j_h} M_{LSJ}^T(j_p j_h) u_{n_p \ell_p}(r_1) u_{n_h \ell_h}(r_1) \quad (\text{Eq. 7})$$

where  $u_{n\ell}(r)$  are the bound state wave functions of the active valence particles. We use harmonic

oscillator wave functions for the bound state, with the oscillator parameter given by

$$\hbar\omega = \frac{45}{A^{1/3}} - \frac{25}{A^{2/3}} \quad (\text{Eq. 8})$$

The form factor  $G_{(r_0)}^{\text{LSJ},T}$  for the direct term of the scattering amplitude is related to the transition density through the relation

$$G_{(r_0)}^{\text{LSJ},T} = \int F_{(r_1)}^{\text{LSJ},T} V_L^{\text{ST}}(r_0, r_1) r_1^2 dr_1 \quad (\text{Eq. 9})$$

where  $V_L^{\text{ST}}(r_0, r_1)$  is the  $L^{\text{th}}$  multipole in the decomposition of the two-body force between the bound nucleon and the incident projectile. The form factor  $G_{(r_0)}^{\text{LSJ},T}$  thus contains all of the structure information which describes the states of the target nucleus, as well as the information concerning the form of the interaction between the projectile and target nucleon.

The form factor  $G_{(r_0)}^{\text{LSJ},T}$  is then folded in with the incident and exit channel optical model wave functions, and squared to get the direct contribution to the DWBA cross section. It is clear from the previous discussion that the magnitude and the shape of the angular distribution is dependent on  
1) the optical model parameters which describe the

elastic scattering from the target nucleus, 2) the form of the two-body force between the projectile and target nucleons, and 3) the transition density. We now consider these elements of the cross section in turn.

The procedure for determining the optical model parameters is well defined. The various parameters of the optical model are adjusted until one obtains the best fit to the measured elastic scattering from the target nucleus, as was discussed in Sec. V.

The form of the two-body force is, however, not well defined. The most desirable two-body force to use would be one which describes two-nucleon scattering, such as the Hamada-Johnston potential.<sup>(53)</sup> However, due to its hard core, this potential cannot be used in its original form. A common technique is to apply the Scott-Moszkowski separation method<sup>(54)</sup> to the attractive-even state components of the Hamada-Johnston potential, and neglect the odd state parts on the basis that they are much weaker than the even state components. This results in an even state force similar to the Serber force. This approach, used by Love and Satchler,<sup>(24)</sup> results in a potential which retains the basic features of the

original potential at low energies and is usable in inelastic nucleon-nucleus scattering calculations as well as in bound state calculations. Petrovich, et al.<sup>(55)</sup> have used a similar approach with the Kallio-Kolltveit<sup>(56)</sup> interaction as the effective interaction and they find that this realistic force gives a good account of proton scattering from  $^{12}\text{C}$  and  $^{40}\text{Ca}$ . Other often-used interactions have Yukawa or Gaussian radial shapes with strengths and ranges chosen to reproduce low energy nucleon-nucleon scattering data. Comparisons between these various interactions are given in Ref. 24.

Many different exchange mixtures other than the Serber mixture have been used in nuclear structure calculations. Often they have large odd-state components, thus differing quite sharply with the forces predicted by realistic interactions. We have tried seven of the more commonly used structure forces<sup>(57)</sup> to see how their predictions for inelastic scattering compare with those for the central force which we use in this work. This force is an even state Yukawa force with a range of 1.4 F, and a strength chosen to be consistent with a recent survey of inelastic scattering analyses.<sup>(58)</sup> The results of this study will be presented in Sec. VIIC2.

For a zero range force, it is clear from Eq. 9 that the form factor  $G_{(r_0)}^{LSJ,T}$  is given by  $r^2$  times the transition density. As the range of the two-body force increases, the form factor continues to reflect the radial shape of the transition density  $F_{(r_1)}^{LSJ,T}$ . This brings us back to the least well defined element in the cross section, namely, the transition density.

#### 4. Transition Density

Referring back to Eqs. 6 and 7, we see that this quantity is determined by the wave functions which describe the states of the target nucleus. At this point it is useful to present a short review of the properties of single particle wave functions  $u_{n\ell}$  which occur in the transition density. In this work we use harmonic oscillator wave functions, hence the single particle wave functions are completely specified by the principal quantum number  $n$  and the orbital angular momentum  $\ell$ . The quantum number  $n$  specifies the number of nodes in the wave function; we use the convention that  $n$  starts from 1. We recall from Sec. IVA that the single particle orbitals which form the shell model basis are the  $1g_{7/2}$ ,  $2d_{5/2}$ ,  $2d_{3/2}$ , and  $3s_{1/2}$ . The single particle

wave functions of interest in this work are therefore  $u_{14}$ ,  $u_{22}$ , and  $u_{30}$ , which have 1, 2, and 3 nodes respectively. The transition density will be constructed from a sum of products of single particle wave functions, each product being weighted by the appropriate  $M_{LSJ}^T(j_p j_h)$ , which in turn is dependent upon the spectroscopic amplitude  $Z_{j_h j_p}^{JT}$ . It is clear that a term such as  $u_{14}u_{14}$  in the sum will contribute an unstructured shape, while a term such as  $u_{22}u_{30}$  will have a very structured contribution. An example of a typical transition density is that for the transition to the  $2_1^+$  state in  $^{138}\text{Ba}$ . It is given by

$$F_{(r_1)}^{202,0} = -0.339u_{14}u_{14} + 0.135u_{14}u_{22} - 0.089u_{22}u_{22} + 0.031u_{22}u_{30}$$

The coefficients  $M_{202}^0(j_p j_h)$  are determined by the wave functions for the  $0_{g.s.}^+$  and  $2_1^+$  states. Different wave functions will give different coefficients, and thus a transition density of different shape. This will in turn modify the shape of the form factor, and also the cross section, as discussed earlier. The magnitude of each  $M_{LSJ}^T(j_p j_h)$  is related to the coherence properties of the amplitudes of the components of the wave functions; in general

a larger  $M_{LSJ}^T(j_p j_h)$  will imply constructive interference between the amplitudes while a small number will imply destructive interference. However, in our case the smallness of the  $M_{LSJ}^T(j_p j_h)$  involving the  $2d_{3/2}$  or  $3s_{1/2}$  orbitals is also in part due to the restriction on the occupation of these levels, as discussed in Sec. IVA. Hence, there are two aspects of the transition density which affect the cross section; the first being the magnitude of the individual components, and the second being the interference among the terms of the sum. Specific examples of transition densities will be illustrated in Sec. VIIC1, where we compare the transition densities for  $^{138}\text{Ba}$  calculated with both the  $A=136-140$  and  $A=136-145$  sets of wave functions. We will find that one can easily distinguish the two sets of wave functions by virtue of the resulting transition densities and the angular distributions which they predict.

We note at this point that other methods exist for extracting the necessary transition density. One promising approach is through inelastic electron scattering.<sup>(59)</sup> It can be shown that the transition density is simply related to the measured form factor in  $(e, e')$ , and high quality  $(e, e')$  data over a wide range of momentum transfer can fully determine

the proton transition density, since electrons are only sensitive to protons in a nucleus. This can then lead to a determination of the neutron transition density if proper account is taken of core polarization effects.

Since 30 MeV protons are not strongly absorbed the cross section is sensitive not only to the tail of the transition density and its value in the vicinity of the nuclear surface as in  $(\alpha, \alpha')$ , but also to the transition density inside of the nucleus. For this reason, medium energy inelastic proton scattering provides a very sensitive test of the wave functions involved in a transition.

The previous discussion has been concerned only with the direct DWBA contribution to the scattering amplitude. The transition density is not defined as such for the exchange amplitude, since for exchange, the bound state wave functions have different radial co-ordinates. However, a corresponding quantity to  $M_{LSJ}^T(j_p j_h)$  for the direct term exists for the exchange term, <sup>(24)</sup> and can be used to obtain an estimate of the magnitude of the exchange contribution to a given transition. In the case of the exchange amplitude, the form factor is different for each pair of partial waves, and involves many



multipoles of the two-body force for an orbital angular momentum transfer  $L$ .

However, it has been found by a number of authors<sup>(24,60-62)</sup> that the direct and exchange amplitudes are constructively coherent in general, and identically so for a zero-range even state force. Atkinson and Madsen<sup>(28)</sup> have done a particularly complete study of the properties of the direct and exchange amplitudes for transitions in single closed shell nuclei (such as the  $N=82$  nuclei). They find that with a Serber force the shapes of the exchange contributions to the angular distributions are very similar to those for the direct term. Since we have also used a Serber force, the previous transition density discussion appears to remain valid when the exchange amplitude is included in the cross section; the main effect of the exchange amplitude being a renormalization of the magnitude of the cross section.

##### 5. Discussion of Selection Rules and Non-Normal Parity States

In terms of the transferred orbital angular momentum  $L$ , spin  $S$ , total angular momentum  $J$  and isospin  $T$ , the selection rules for the direct amplitude in the DWBA are

$$\vec{J}_i + \vec{J}_f = \vec{J}$$

$$\vec{L} + \vec{S} = \vec{J} \quad S = 0, 1$$

$$\vec{T}_i + \vec{T}_f = \vec{T} \quad T = 0, 1$$

$$\Delta\pi = (-)^L$$

where  $\Delta\pi$  denotes the change in parity. Both  $^{138}\text{Ba}$  and  $^{144}\text{Sm}$  have  $J_i^\pi = 0^+$ , so  $J = J_f$ .

For the exchange term in the DWBA amplitude, the selection rule  $\Delta\pi = (-)^L$  no longer holds. Thus for exchange, all four triads  $(LSJ) = (J0J), (J1J), (J-1 \ 1J),$  and  $(J+1 \ 1J)$  can contribute to the cross section, while for the direct term, only the first or second pair can contribute. The terms which the second pair of triads give rise to are commonly referred to as non-normal parity terms and are found in general to be small except in the case of transitions to high spin states, where they can become non-negligible. (24)

The only experimental angular distributions for non-normal parity states (states for which  $\pi \neq (-)^J$ ) in masses  $A > 80$  of which we are aware are those for the  $3^+$  and  $(5^+)$  states in  $^{138}\text{Ba}$ , which we observe, and an angular distribution for a  $4^-$  state in

$^{208}\text{Pb}$ . (63) In all cases, the cross sections are less than 20  $\mu\text{b/sr}$  at all angles. The fact that so few non-normal parity states are observed in inelastic scattering is evidence in itself that cross sections to such states must be small. In conclusion, both theory and experiment indicate that non-normal parity states (also often referred to as spin-flip states) are very weakly excited in medium energy inelastic proton scattering on heavy nuclei.

As mentioned in Sec. IVB, the pseudo spin-orbit coupling scheme of Hecht and Adler<sup>(44)</sup> predicts a selection rule for inelastic scattering. This selection rule is based on the assumption that the transition densities are independent of the quantum numbers  $j_p j_h$  and depend only on the orbital angular momentum transfer  $L$ . For  $(\alpha, \alpha')$  this is a reasonable assumption, since the alpha particles are strongly absorbed by the nucleus and are sensitive to the transition density only at the nuclear surface where for the case of  $N=82$  nuclei, the transition densities are quite similar as illustrated in Ref. 14. However, this may not be a good assumption for protons, which are not strongly absorbed. The selection rule states that  $\Delta B=0$  where  $B$  is the total

pseudospin. For an even number of protons,  $B$  ranges from  $v/2$  to 0, where  $v$  is the seniority of the state. The wave functions for  $^{138}\text{Ba}$  which we have used have mixed seniority, but projecting out wave functions of good seniority reveals that the low-lying  $J \neq 0$  states are more than 80% seniority two states. In the Hecht-Adler scheme, the lowest  $2^+$ ,  $4^+$ , and  $6^+$  states have  $v=2$ ,  $B=0$  and transitions to these states from the  $v=0$ ,  $B=0$  ground state are allowed. Our data show them to be relatively strongly excited. The next group of states have  $v=2$ ,  $B=1$  so transitions to these states would violate the  $\Delta B=0$  rule. With two exceptions, Figure 2 shows that the positive parity states between 2.2-3.2 MeV are weakly excited. The third group of states predicted in the pseudo spin scheme are  $v=4$ ,  $B=0$  states. The relatively strong  $2^+$  states at 3339 and 3368 keV in  $^{138}\text{Ba}$  are perhaps members of this group, since the shell model also predicts these levels to be mostly seniority four states.

We thus find that the pseudo spin orbit selection rules predict results which are in qualitative agreement with our data.

## VII. DISCUSSION OF RESULTS

In this section we present results of the calculations described in Sections IV and VI, and compare the theoretical predictions from those sections with the experimental results from Section III.

### A. Comparison of Shell-Model Calculations to Experiment

We begin by contrasting the results of the shell model calculations for  $^{138}\text{Ba}$  and  $^{144}\text{Sm}$  described in Sec. IVA with the experimental energy level spectra obtained in Sec. IIIA. The energy level spectra for  $^{138}\text{Ba}$  resulting from shell model calculations with both the A=136-145 and A=136-140 Hamiltonians, together with the experimental level spectrum as determined from our measurements, are shown in Figure 14. The calculated energy level spectrum, using the A=136-140 interaction, is in excellent agreement with experiment. There is one-to-one correspondence between theory and experiment up to 2.9 MeV of excitation, with the exception of the experimentally missing excited  $0^+$  state. Each of the states predicted by theory up to 2.85 MeV are in agreement with their experimental counterparts to within 200 keV, and for most states the agreement is better than

100 keV. In Sec. IIIC4 we noted that the angular distribution for the state at 2201 keV did not enable us to assign this state  $J^\pi=6^+$ , although a  $6^+$  assignment is not inconsistent with the data, as seen in Figure 11. Comparing experiment to theory, one clearly finds additional support for a  $6^+$  assignment to this state. The states at 2415 and 2445 keV, which have been assigned  $(5^+)$  and  $3^+$  respectively,<sup>(37)</sup> have structureless angular distributions and are excited very weakly in our  $(p,p')$  measurements, thus leading us to concur with the non-normal parity assignments. These  $J^\pi$  assignments are also in excellent agreement with the shell model predictions. Recalling from Sec. IIIC3 the discussion of a  $1^+-4^+$  doublet at 2583-2584 keV, we see such a proposal is strongly supported by predictions of the shell model.

In the discussion of Sec. IVA, we indicated that the parameters in the A=136-145 interaction may reflect deficiencies in the basis space for the upper N=82 isotones, since states of these isotones used in the determination of the interaction parameters may have configurations lying outside the present basis space. We observe from Figure 14 that the A=136-145 interaction does not reproduce the <sup>138</sup>Ba energy levels with the accuracy of the A=136-140 Hamiltonian. The major differences are in the first  $4^+-6^+$  splitting, and in the spacing of the levels from 2.3 to 2.6 MeV. A more sensitive test of the relative quality of

the wave functions resulting from these interactions is found in the microscopic DWBA calculations, which will be discussed shortly.

The experimental energy level spectrum for  $^{144}\text{Sm}$  along with the predicted energy level spectrum calculated from the A=136-145 interaction is shown in Figure 15. The general characteristics of the experimental spectrum are reproduced; however the specific state-by-state agreement is not as impressive as the agreement between theory and experiment for  $^{138}\text{Ba}$ . Allowing more than one proton excitations into the  $3s_{1/2}$  and  $2d_{3/2}$  orbits, and inclusion of pairs of particles in the  $1h_{11/2}$  orbit would be expected to improve the agreement between theory and experiment.

## B. Collective Model Results

In this section we present the results of a collective model analysis of all states in  $^{138}\text{Ba}$  and  $^{144}\text{Sm}$  for which  $J^\pi$  assignments have been made. Figures 16 and 17 show our measured angular distributions for the lowest-lying  $2^+$ ,  $3^-$ ,  $4^+$ , and  $6^+$  states in  $^{138}\text{Ba}$  and  $^{144}\text{Sm}$ , along with the collective model predictions for these states. The optical model parameters labeled Set SII (Set SI) in Table 2 have been used in the calculations for  $^{138}\text{Ba}$  ( $^{144}\text{Sm}$ ), but any of the three sets give fits of similar quality. As seen in Figures 16 and 17, the predicted angular distributions

are in good agreement with the data for the  $2^+$  and  $3^-$  states, but this agreement deteriorates as one goes to the higher spin states. Results of calculations for the remaining states observed in our measurements are not shown, since our use of characteristic shapes indicates that all experimental angular distributions for a given  $J^\pi$  are very similar in shape. The empirical observation that the shapes of the angular distributions appear to be independent of excitation energy in the energy range from 1-3.5 MeV has been verified through our collective model DWBA calculations.

Deformation parameters  $\beta_L'$ , as discussed in Sec. VIA, have been extracted by normalizing the experimental and theoretical cross sections over the angular range of the data. The results of this analysis are given in Table 3. The smallness of these parameters, except for the lowest  $3^-$  states, is another indication that the states are not strongly collective. Barker and Hiebert<sup>(17)</sup> have also studied  $^{144}\text{Sm}(p,p')$  at 30 MeV, and the results of their collective model analysis are in good agreement with ours for the four states which they observe (see Table 3).

In Table 3 we also list the isoscalar transition strengths  $G_L$ , in single particle units, calculated from Eqs. 2 and 3. We note they are only about one-half the value obtained from Coulomb excitation measurements for the



$2_1^+$  states. This phenomenon persists for other nuclei in this mass region,<sup>(16)</sup> which seems to be the only region which does not exhibit equality between the isoscalar and electromagnetic transition rates when they are extracted using this model.

### C. Microscopic Model Analysis

As discussed in the introduction, one of the main purposes in undertaking this work was to determine if large basis shell-model wave functions could accurately account for both the shape and magnitude of measured angular distributions obtained from inelastic proton scattering. To this end, we have applied the microscopic DWBA theory discussed in Sec. VIB to calculate angular distributions for the  $2_1^+$ ,  $2_2^+$ ,  $4_1^+$ ,  $4_2^+$ , and  $6_1^+$ ,  $6_2^+$  states observed in  $^{138}\text{Ba}$  and  $^{144}\text{Sm}$ .

The pertinent details of the inelastic scattering calculation are as follows. The optical model parameters labeled Set SII(Set SI) in Table 2 are used to describe the incident and exit channels of  $^{138}\text{Ba}(^{144}\text{Sm})$ . The bound states are described by harmonic oscillator wave functions, with an harmonic oscillator constant obtained from Eq. 8. The two-body interaction between the projectile and target nucleons was central only, with a Serber exchange mixture and a Yukawa radial dependence. The range of the force was taken to be 1.4 F and its strength  $(V_{pp}^{S=0} = -8.4 \text{ MeV})$ ,

where  $v_{pp}^{S=0}$  is the  $S=0$  part of the proton-proton interaction) was chosen to be the mean of the strengths obtained in a recent survey of inelastic scattering analyses. (58)

Core polarization, i.e. the effect due to contributions to the cross section from nucleons outside the explicit shell-model basis space, must be included for a proper description of inelastic scattering. (64) In the case of electromagnetic transitions these effects also appear and are accounted for by renormalizing the charge on the nucleons, i.e., by introducing a "polarization charge". Madsen (28) and McManus (29) have shown that one can similarly correct for finite basis-space effects in inelastic scattering by renormalizing the strength of the two-body force which mediates the transition. Thus one has an "effective force" for  $(p,p')$  which is analogous to the "effective charge" for electromagnetic transitions. (65)

One can get an idea of the amount of core participation in the low-lying states of  $^{138}\text{Ba}$  by noting that for the wave functions used here, the calculated  $B(E2; 2_1^+ \rightarrow 0_1^+)$  is a factor of 3.2 too small (66) if no polarization charge  $\delta_e$  is used. This implies that  $(1+\delta_e)^2=3.2$ , or  $\delta_e=0.8$ . To account for the contribution to the  $(p,p')$  reaction of protons excited from the core, one therefore renormalizes the interaction strength  $v_{pp}$  to  $(1+\delta_e)v_{pp}$ . However, neutron

core excitations also contribute to  $(p,p')$  cross sections and are, in fact, more important than those for protons, since the proton-neutron two-body interaction  $V_{pn}$  is stronger than  $V_{pp}$ . If it is assumed, as has been found by Bernstein<sup>(67)</sup> and Astner, et al.<sup>(68)</sup> that contributions from neutron and proton core excitations are approximately in the ratio of  $N/Z$  (the ratio expected in a collective model picture), we need an additional term,  $N/Z \delta_e V_{pn}$ . For the Serber exchange mixture we use,  $V_{pn}=2V_{pp}$ . Thus one obtains a total effective force of  $(1+\delta_e)V_{pp}+2N/Z\delta_e V_{pp}=[1+\delta_e(1+2N/Z)]V_{pp}$ , i.e. the strength is increased by a factor of  $(1+\delta_e(1+2N/Z))$ . We use this result in all calculations in this paper. We have also inverted this process and used the measured enhancement factors to extract polarization charges for other transitions in  $^{138}\text{Ba}$ , for which electromagnetic transition data are not available. Calculations of cross sections were performed for the  $2_1^+$ ,  $2_2^+$ ,  $4_1^+$ ,  $4_2^+$ ,  $6_1^+$ , and  $6_2^+$  states in  $^{138}\text{Ba}$ . The enhancement factors were extracted by normalizing the experimental and theoretical integrated cross sections over the angular range of the data. The results are shown in Column 3 of Table 4 and we see that the  $\delta_e$  are constant within the probable overall uncertainty in the analysis.

#### 1. Microscopic DWBA Calculations for $^{138}\text{Ba}$

For  $^{138}\text{Ba}$ , we have calculated angular distributions using both sets ( $A=136-140$  and  $A=136-145$  Hamiltonians) of

wave functions for the aforementioned 6 states. Figures 18 and 19 show the angular distributions predicted by each set of wave functions, together with the appropriate data. We see that the magnitudes and shapes of the calculated angular distributions are in good agreement with the data for the  $2_1^+$ ,  $4_1^+$ , and  $6_1^+$  states for both sets of wave functions. However, the agreement between theory and experiment for the  $2_2^+$ ,  $4_2^+$ , and  $6_2^+$  states is much better for the A=136-140 set of wave functions than for the A=136-145 set, which predicts cross sections which are an order of magnitude low, and also exhibit poorer agreement in shape. From this analysis it appears that the A=136-140 set of wave functions gives the better description of low-lying states of  $^{138}\text{Ba}$ .

To find the reason for this behavior, recall from Sec. VIB4 that all of the nuclear structure information entering the DWBA calculation is contained in the transition densities. Thus it is informative to compare their differences in structure as calculated from each set of wave functions. Figure 20 shows such a comparison. The magnitude of the transition density is plotted versus the radial coordinate in units of  $r_0 A^{1/3}$ ; thus unity corresponds to the nuclear surface. Inspection shows that the transition densities for the  $2_1^+$ ,  $4_1^+$ , and  $6_1^+$  states are quite similar for both sets of wave functions. They peak slightly inside

the nuclear surface, which is a general characteristic<sup>(52)</sup> of these quantities. We recall that the cross sections calculated for these states were very similar for both sets of wave functions. However, looking at the transition densities for the  $2_2^+$ ,  $4_2^+$ , and  $6_2^+$  transitions, we note distinct differences. The A=136-145 wave functions yield transition densities with a pronounced decrease of the surface peaking, and an increase in magnitude of the peak near 0.6 of the nuclear surface, relative to the A=136-140 results. For the  $6_2^+$  state, this effect is so great that the transition density resembles that for a much lighter nucleus. Since the transition density (and therefore the form factor) peak too far inside the nuclear surface for this transition, the diffraction pattern predicted by the DWBA is pushed out, as if the target nucleus were indeed much lighter. This is exactly what we observe for the calculated  $6_2^+$  cross section for the A=136-145 set of wave functions.

We can infer specifically what is wrong with this set of wave functions by considering the individual contributions to the total transition density for the  $6_2^+$  state, for example. Figure 21 shows this transition density broken down into its component parts  $u_{nl}=u_{14}$ ,  $u_{14}$  and  $u_{14}u_{22}$ . The A=136-140 set of wave functions enhances the  $u_{14}u_{22}$  term relative to the  $u_{14}u_{14}$  term, which results

in the surface peaking. However, this enhancement is not present for the A=136-145 wave functions, which results in the transition density being very small at the surface due to a cancellation effect. Tracing back one step farther, we can look at the spectroscopic amplitudes which contribute to  $u_{14}u_{14}$  and  $u_{14}u_{22}$  and thus directly study the wave functions. Only the  $\langle g_{7/2} | a^+ a | g_{7/2} \rangle$  matrix element contributes to  $u_{14}u_{14}$ , while both the  $\langle g_{7/2} | a^+ a | d_{5/2} \rangle$  and  $\langle d_{5/2} | a^+ a | g_{7/2} \rangle$  matrix elements contribute to the  $u_{14}u_{22}$  term of the sum. Table 5 shows the structure of the largest components of the pertinent wave functions, as well as the individual contributions to the  $6_2^+$  transition density calculated with both sets of wave functions. The two transition densities are thus

$$F_{(r_1)}^{606,0} = 0.1292 u_{14}u_{14} + 0.3223 u_{14}u_{22} \quad A=136-140$$

$$F_{(r_1)}^{606,0} = 0.1765 u_{14}u_{14} + 0.1978 u_{14}u_{22} \quad A=136-145$$

The quantity of interest is the ratio  $u_{14}u_{22}/u_{14}u_{14}$  which has the value 2.50(1.12) for the A=136-140 (A=136-145) interaction. The major reason for the smaller ratio from the A=136-145 wave functions is the smallness of the  $u_{14}u_{22}$  term. Even though this set of wave functions has the smaller  $g_{7/2}-d_{5/2}$  single particle splitting and hence would be expected to have the larger  $u_{14}u_{22}$  term, a detailed comparison of the wave functions in Table 5 show this is

not true. The largest contributions to  $u_{14}u_{22}$  for the  $A=136-140$  set come from the  $(g_7)^6 + (g_7)^5(d_5)^1$  and  $(g_7)^4(d_5)^2 \rightarrow (g_7)^4(d_5)^2$  amplitudes, which for the  $A=136-145$  wave functions are much smaller. This arises from the observation that the smaller  $g_{7/2}-d_{5/2}$  splitting leads to a fragmentation of the strength of the  $6_2^+$  wave function over many components. Many of these components cannot be connected by the one body  $(p,p')$  operator  $(a^\dagger a)$  to the strong components of the much less fragmented ground state, and hence do not contribute significantly to the transition density. It thus appears that this decreased mixing between the  $g_{7/2}$  and  $d_{5/2}$  orbitals is the required ingredient in obtaining a reasonable fit to the angular distribution for the  $6_2^+$  state. A similar analysis applied to the transition densities for the  $4_2^+$  states arrives at the same conclusion—namely that there appears to be too much mixing of the  $g_{7/2}-d_{5/2}$  orbitals in the higher lying states as calculated with the  $A=136-145$  interaction. Specific information concerning the structure of the wave functions can thus be obtained by analyzing the composition of the transition densities in this manner.

Comparing the DWBA calculations result from the collective model (Fig. 16) and microscopic model (18) for the  $2_1^+$  state, we see that the collective model does a somewhat better job of fitting the data. This is due mainly

to the  $2_1^+$  microscopic calculation slipping out of phase with the maxima and minima of the data. We have performed a collective model calculation using the form factor obtained by deforming only the real part of the optical model potential, and obtained an angular distribution nearly identical to the angular distribution obtained from the microscopic model. This implies that if one were to combine the form factor obtained by deforming the imaginary part of the optical model with the real form factor used in the microscopic analysis, the resulting angular distribution would be in as good agreement with the data as that of the full deformed collective model. Unfortunately, the computer code we use for the microscopic DWBA calculations does not at present have the option of using a complex form factor; thus the above conclusion is rather speculative. However, it has recently been found that using a complex microscopic form factor results in appreciably better fits to angular distribution<sup>(69)</sup> and asymmetry<sup>(70)</sup> data. It would also be interesting to determine if the addition of an imaginary term to the form factor, which appears to improve the fit to the  $2_1^+$ , would destroy the relatively good fits to the  $4_1^+$  and  $6_1^+$  states obtained with the present microscopic approach.



It must be noted that our calculations use a multiplicative constant in the form factor to account for core polarization and the angular distributions take the shape predicted by the purely microscopic calculation. Other microscopic calculations<sup>(64)</sup> frequently employ an additive term in the form factor based on the collective model to simulate the effects of core polarization. Often times, using this latter procedure, the collective term is the dominant contributor to the cross section, so the predicted shape for the angular distribution is in reality due to the collective model contribution. Thus, these "microscopic" calculations achieve good agreement with the data as regards the shape of the angular distribution, due to the fact that collective model predictions for the shape are in general better than those calculated from a purely microscopic model such as we have used.

## 2. Calculations with Other Forces

A Serber exchange mixture, which is an even state force, is generally employed in microscopic inelastic scattering calculations. It has been found to contain about the correct exchange strength to give the required enhancement for different L transfers. However, in nuclear structure calculations, many other types of forces have been employed, and we have tried a number of these to see if they give as good a description of the inelastic scattering

process as does the Serber mixture. We have made calculations for each of the forces "Cal", "Cop", Clark Elliot I, Ferrell-Visscher, Rosenfeld and Soper summarized in Ref. 57, all of which contain non-negligible odd-state components. The triplet-even parts of the various forces have all been normalized to  $V_{TE} = -40$  MeV. The range of the two-body force, which had a Gaussian radial shape, was 1.67 F; this translates into 1.346 F for a corresponding Yukawa radial dependence which we use. The strength of the Serber force is very similar to the strength we have used in the calculations discussed previously. The results are shown in Table 6, along with the results obtained with the Serber mixture.

We observe that only the Clark-Elliot I and Soper interactions (which have weak odd state components) yield results similar to the Serber mixture, which reproduced the data. The forces with strong odd-state components cause the direct and exchange cross sections to exhibit the wrong dependence upon L-transfer and in addition, often the theoretical angular distributions acquire shapes which do not resemble the data. We conclude that while such forces may be acceptable for nuclear structure calculations, the strong odd-state components make them inadequate to describe inelastic proton scattering.

We have also performed calculations including tensor forces, consistent with OPEP<sup>(58)</sup> and find that the tensor force contributions to the cross section are at most 7%, and this is for the  $6^+$  states, where the non-normal exchange amplitudes are becoming non-negligible.<sup>(24)</sup> The spin-orbit force may be important<sup>(71)</sup> for the  $6^+$  states, and this possibility is being investigated further.

In addition, we have calculated angular distributions for the non-normal parity  $3^+$  and  $5^+$  states, using only the A=136-140 set of wave functions. Such states are not expected to be enhanced due to collective effects, but should be sensitive to the tensor and LS forces. The predicted cross sections calculated with central, and central plus tensor plus LS forces obtained from the Hamada Johnston potential and given in Ref. 58, are presented in Figure 22, along with the data. The enhancement due to core polarization is not included, and the direct plus exchange calculations underestimate the data by a factor of 3-5 for the central plus tensor plus LS force.

### 3. Microscopic DWBA Calculations for $^{144}\text{Sm}$

Only the A=136-145 Hamiltonian was applicable to  $^{144}\text{Sm}$ , so only the set of wave functions corresponding to this interaction was employed in the DWBA calculations. The results are shown in Fig. 23. The D+E angular distributions for the  $2_1^+$  and  $4_1^+$  states are a factor of two smaller

than the data at forward angles, while the  $6_1^+$  calculation is not in good agreement with the experimental distribution. However, we recall from Sec. IIID4 that this state is possibly a doublet, which would make any theoretical conclusion based on this state tenuous at best. The underestimation of the magnitude is undoubtedly due in part to the restricted basis space in which the shell model calculation was performed. This inadequacy of the basis space is clearly pointed out when one considers the calculation for the  $2_2^+$  state. All of the strength has been concentrated in  $2_1^+$ , causing the angular distribution for the  $2_2^+$  state to fall a factor of 25 below the data. In addition, the shape is not qualitatively correct; the maxima at  $40^\circ$  is larger than the first at  $20^\circ$ . The calculated  $4_2^+$  angular distribution is a factor of 3 lower than the data, while the calculation for the  $6_2^+$  bears no resemblance to the data. This can easily be predicted from observation of the transition density for the  $6_2^+$  state; it is negligible at the surface of the nucleus. All of its strength is concentrated around 0.6 of the nuclear radius, as in the similar case for the  $6_2^+$  transition density in  $^{138}\text{Ba}$  calculated with this set of wave functions. Most disturbing about this  $^{144}\text{Sm}$  microscopic calculation is the fact that a constant polarization charge does not reproduce the magnitude of the angular distribution for different

L-transfers. One is required to use a state dependent polarization charge, whereas a state independent charge was found to be adequate for states in  $^{138}\text{Ba}$ . (65) However, we feel this also is a manifestation of the limited basis space for the  $^{144}\text{Sm}$  shell-model calculation.

### VIII. CONCLUSION

High resolution medium energy inelastic proton scattering has been shown to be an effective method for obtaining precise information concerning the excited states of a nucleus. We have obtained excitation energies for levels in  $^{138}\text{Ba}$  which are in excellent agreement with previous gamma ray work on this nucleus, and in addition we are able to reduce the uncertainty on previous spin-parity assignments, and in most cases suggest an absolute assignment. We have increased the number of known levels up to  $E_x=3.4$  in  $^{144}\text{Sm}$  from 8 to 18 and suggested spin-parity assignments for the majority of these states. The experimental information concerning the levels up to  $E_x=3.4$  MeV in  $^{138}\text{Ba}$  and  $^{144}\text{Sm}$  has been reviewed, and found to be in good agreement with recent shell model calculations for this region.

Collective model DWBA calculations have been carried out for both nuclei, using a form factor obtained by deforming the real and imaginary parts of the optical model potential. The results were analyzed using the formalism of Bernstein to obtain estimates of the strengths of the corresponding electromagnetic transition rates.

Microscopic DWBA calculations including the exchange amplitude were performed for the  $2_{1,2}^+$ ,  $4_{1,2}^+$ , and  $6_{1,2}^+$  states in  $^{138}\text{Ba}$  and  $^{144}\text{Sm}$ , using shell model wave functions<sup>(19-20)</sup> and a realistic two-nucleon force. The necessary structure amplitudes were calculated with a modified version of the Oak Ridge-Rochester shell model code. In the case of  $^{138}\text{Ba}$ , two sets of shell model wave functions were calculated, and it was determined from the DWBA calculations that inelastic proton scattering clearly distinguished one set as superior to the other. With this result the transition densities, which provide the link between the wave functions and the DWBA reaction model, were then analyzed to see if one could determine the undesirable properties of the poorer set of wave functions. The results of this analysis indicated that the large mixing between the  $g_{7/2}$  and  $d_{5/2}$  orbitals was the problem in the set of wave functions which yielded the poorer result. We find that a careful consideration of the transition density between two states can provide useful information concerning the structure of the wave functions for these states.

The use of large basis shell model wave functions such as we have used in this work appears to yield quite satisfactory results and this technique should be useful in performing consistent studies of inelastic nucleon scattering. Such an analysis will hopefully enable one

to study the effects of core polarization and the nature of the polarization charge of the core nucleons.



## REFERENCES

1. B. H. Wildenthal, E. Newman, and R. L. Auble, Phys. Rev. C3, 1199 (1971).
2. W. P. Jones, L. W. Borgman, K. T. Hecht, J. Bardwick, and W. C. Parkinson, Phys. Rev. C4, 580 (1971).
3. R. K. Jolly and E. Kashy, Phys. Rev. C4, 887 (1971).
4. R. K. Jolly and E. Kashy, Phys. Rev. C4, 1398 (1971).
5. D. von Ehrenstein, G. C. Morrison, J. A. Nolen, and N. Williams, Phys. Rev. C1, 2066 (1970).
6. P. A. Moore, P. J. Riley, C. M. Jones, M. D. Mancusi, and J. L. Foster, Jr., Phys. Rev. C1, 1100 (1970);  
P. A. Moore, P. J. Riley, C. M. Jones, M. D. Mancusi, and J. L. Foster, Jr., Phys. Rev. Letters 22, 356 (1969);  
G. C. Morrison, N. Williams, J. A. Nolen, Jr., and D. von Ehrenstein, Phys. Rev. Letters 19, 592 (1967);  
P. von Brentano, W. J. Braithwaite, J. G. Cramer, W. W. Eidson, and G. W. Phillips, Phys. Letters 26B, 448 (1968).  
K. Madersbach, A. Heusler, and J. P. Wurm, Nucl. Phys. A146, 477 (1970).
7. John C. Hill and D. F. Fuller, Phys. Rev. C5, 532 (1972).
8. L. C. Carraz, E. Monnard, and A. Moussa, Nucl. Phys. A171, 209 (1971).
9. M. A. J. Mariscotti, W. Gelletly, J. A. Moragues, and W. R. Kane, Phys. Rev. 174, 1485 (1968).
10. P. Van der Merwe, I. J. Van Heerden, W. R. McMurray, and J. G. Malan, Nucl. Phys. A124, 433 (1969).
11. J. Kownacki, H. Ryde, V. G. Sergejev, and Z. Sujkowski, Annual Report, AFI Stockholm (1971).
12. O. Hansen and O. Nathan, Nucl. Phys. 42, 197 (1963).
13. Per Rex Christensen and Fu-Chia-Yang, Nucl. Phys. 72, 657 (1965).
14. F. T. Baker and R. Tickle, Phys. Rev. C5, 182 (1972).
15. H. W. Baer, H. C. Griffin, and W. S. Gray, Phys. Rev. C3, 1398 (1971).
16. J. H. Barker and J. C. Hiebert, to be published.

17. J. H. Barker and J. C. Hiebert, Phys. Rev. C4, 2256(1971).
18. P. B. Woollam, R. J. Griffiths, and N. M. Clarke, Nucl. Phys. A189, 321(1972).
19. R. H. Bassel, G. R. Satchler, R. M. Drisko, and E. Rost, Phys. Rev. 128, 2693(1962).
20. H. G. Blosser, G. M. Crawley, R. deForest, E. Kashy, and B. H. Wildenthal, Nucl. Instr. and Methods 91, 1(1971).
21. S. M. Austin, P. J. Locard, S. N. Bunker, J. M. Cameron, J. R. Richardson, J. W. Verba, and W. T. H. vanOers, Phys. Rev. C3, 1514(1971).
22. R. Reif and J. Höhn, Nucl. Phys. A137, 65(1969).
23. G. R. Satchler, Nucl. Phys. 77, 481(1966).
24. W. G. Love and G. R. Satchler, Nucl. Phys. A159, 1(1970).
25. J. B. French, E. C. Halbert, J. B. McGrory, and S. S. M. Wong, Advances in Nuclear Physics, Vol. III, eds. M. Baranger and E. Vogt (Plenum Press, New York, 1969).
26. B. H. Wildenthal, Phys. Rev. Letters 22, 1118(1969).
27. B. H. Wildenthal and D. Larson, Phys. Letters 37B, 266(1971).
28. J. Atkinson and V. A. Madsen, Phys. Rev. C1, 1377(1970).
29. H. McManus in The Two-Body Force in Nuclei, eds. S. M. Austin and G. M. Crawley (Plenum Press, New York, 1972).
30. R. K. Jolly, G. F. Trentelman, and E. Kashy, Nucl. Instr. and Methods 87, 325(1970).
31. D. L. Bayer, Ph.D. Thesis, Michigan State University 1970 (unpublished).
32. B. L. Cohen, Rev. Sci. Instr. 30, 415(1959).
33. G. F. Trentelman and R. G. H. Robertson, unpublished.
34. F. D. Becchetti, Jr., and G. W. Greenlees, Phys. Rev. 182, 1190(1969).
35. G. R. Satchler, Nucl. Phys. A92, 273(1967).
36. J. R. Kerns and J. X. Saladin, preprint.

37. E. Achterberg, F. C. Iglesias, A. E. Jech, J. A. Moragues, D. Otero, M. L. Perez, A. M. Proto, J. J. Rossi, W. Scheuer, and J. F. Suárez, Phys. Rev. C5, 1759(1972).
38. J. Kownacki and K. G. Rensfelt, Phys. Letters 35B, 153 (1971).
39. D. Eccleshall, M. J. L. Yates, and J. J. Simpson, Nucl. Phys. 78, 481(1966).
40. S. Raman, private communication.
41. M. Rho, Nucl. Phys. 65, 497(1965).
42. M. Waroquier and K. Heyde, Nucl. Phys. A164, 113(1971).
43. V. Gillet and M. Rho, Phys. Letters 21, 82(1966).
44. K. T. Hecht and A. Adler, Nucl. Phys. A137, 129(1969).
45. G. W. Greenlees and G. J. Pyle, Phys. Rev. 149, 836(1966).
46. S. A. Fulling and G. R. Satchler, Nucl. Phys. A111, 81 (1968).
47. D. L. Show, unpublished.
48. A. M. Bernstein, Advances in Nuclear Physics, Vol III, eds. M. Baranger and E. Vogt (Plenum Press, New York, 1969).
49. R. Schaeffer and J. Raynal, unpublished.
50. J. Raynal, Nucl. Phys. A97, 572(1967).
51. V. A. Madsen, Nucl. Phys. 80, 177(1966).
52. F. Petrovich, Michigan State University Thesis, 1970 (unpublished).
53. T. Hamada and I. D. Johnston, Nucl. Phys. 34, 382(1962).
54. S. A. Moszkowski and B. L. Scott, Annals of Phys. 11, 65(1960).
55. F. Petrovich, H. McManus, V. A. Madsen, and J. Atkinson, Phys. Rev. Letters 22, 895(1969).
56. A. Kallio and K. Kolltveit, Nucl. Phys. 53, 87(1964).
57. V. Gillet, A. M. Green, and E. A. Sanderson, Nucl. Phys. 88, 321(1966).

58. S. M. Austin in The Two-Body Force in Nuclei, eds. S. M. Austin and G. M. Crawley (Plenum Press, New York, 1972).
59. R. M. Haybron, M. B. Johnson, and R. J. Metzger, Phys. Rev. 156, 1136(1967).
60. J. Atkinson and V. A. Madsen, Phys. Rev. Letters 21, 295(1968).
61. K. A. Amos, V. A. Madsen, I. E. McCarthy, Nucl. Phys. A94, 103(1967).
62. H. V. Geramb and K. A. Amos, Nucl. Phys. A163, 337(1971).
63. A. Scott, private communication.
64. W. G. Love and G. R. Satchler, Nucl. Phys. A101, 424 (1967).
65. D. Larson, S. M. Austin, and B. H. Wildenthal, to be published in Phys. Letters.
66. D. Larson and B. H. Wildenthal, B. A. P. S. 17, 512(1972).
67. A. M. Bernstein, Phys. Letters 29B, 335(1969).
68. G. Astner, I. Bergström, J. Blomqvist, B. Fant, and K. Wikström, Nucl. Phys. A182, 219(1972).
69. G. R. Satchler, Phys. Letters 35B, 279(1971).
70. R. H. Howell and G. R. Hammerstein, to be published.
71. W. G. Love, Phys. Letters 35B, 371(1971).

**APPENDIX A**  
**TABLES**

Table 1: Energy Levels of  $^{138}\text{Ba}$  and  $^{144}\text{Sm}$ .

$^{138}\text{Ba}$		$^{144}\text{Sm}$	
Present Work $E_x[J^\pi]^{a,d}$	Previous Work $E_x[J^\pi]^b$	Present Work $E_x[J^\pi]^{a,d}$	Previous Work $E_x[J^\pi]^c$
1436 <sup>g</sup> $\pm 1.0$ $2^+$	1435.7 $2^+$	1661 <sup>g*</sup> $\pm 1.0$ $2^+$	1660.6 $\pm 1.0$ $2^+$
1898 <sup>g*</sup> $\pm 1.0$ $4^+$	1898.4 $\pm 0.3$ $4^+$	1811 <sup>g</sup> $\pm 1.2$ $3^-$	1810.1 $3^-$
2090 <sup>g*</sup> $\pm 1.0$ $6^+$	2090.1 $\pm 0.6$ (6) <sup>+</sup>	2191 <sup>g*</sup> $\pm 1.0$ $4^+$	2190.6 $\pm 1.0$ $4^+$
2201 $\pm 2.0$	2203.2 <sup>f</sup>	2324 <sup>e</sup> $\pm 1.0$	2323.2 $6^+$
2218 $\pm 1.0$ $2^+$	2217.9 $2$	2423 <sup>*</sup> $\pm 1.0$ $2^+$	2423.4 $\pm 1.0$
2308 <sup>*</sup> $\pm 1.0$ $4^+$	2307.4 $\pm 0.3$ (3,4)	2478 $\pm 1.9$	2478.3 $0^+$
2415 $\pm 1.2$	2414.9 (5 <sup>+</sup> ) <sup>h</sup>	2588 $\pm 1.0$ $4^+$	
2445 $\pm 1.2$	2445.4 $3^+$ <sup>h</sup>	2661 $\pm 1.6$	
	2582.8 $1,2$	2800 $\pm 1.6$ $2^+$	
2584 $\pm 1.0$ $4^+$		2826 $\pm 1.8$	2830
2639 $\pm 1.2$ $2^+$	2639.3 $2$	2883 $\pm 1.9$ $4^+$	
2779 <sup>*</sup> $\pm 1.0$ $4^+$	2779.2 $\pm 0.5$ 2,3,4	3020 $\pm 2.0$ $4^+$	
2881 <sup>g</sup> $\pm 1.2$ $3^-$	2880.5 $3^-$	3080 $\pm 2.0$	
(2929) $\pm 2.0$	2931.1 $1,2$	3123 $\pm 1.8$	3123.8
(2990) $\pm 2.0$	2990.8 $1,2,3,4$	3196 $\pm 1.9$	
3050 <sup>*</sup> $\pm 1.0$	3049.9 $\pm 1.0$ $1,2$	3227 $\pm 2.0$ $3^-$	
3156 $\pm 1.2$ $4^+$		3266 $\pm 2.3$	
	3163.5 $2,3,4$	3308 $\pm 2.1$ $6^+$	
3254 $\pm 1.2$			
3285 $\pm 1.4$			
3339 $\pm 1.4$ $2^+$	3339.5 $1,2$		
	3352.2 $1,2$		
3368 $\pm 1.8$ $2^+$	3365.9 $1,2$		

<sup>a</sup>Excitation energies in keV.<sup>b</sup>From Ref. 7, except see (f,h) below.<sup>c</sup>From Ref. 17 and references cited therein and Ref. 40.<sup>d</sup>Subset of levels used in energy calibration is marked with an asterisk (\*).<sup>e</sup>Unresolved doublet whose angular distribution is consistent with a spin  $6^+$  state plus a lower spin state.<sup>f</sup>From Ref. 8.<sup>g</sup>Used in determination of characteristic shapes.<sup>h</sup>From Ref. 37.

Table 2. Optical Model Parameters for  $^{138}\text{Ba}(^{144}\text{Sm})$ .

	Adjusted Becchetti-Greenlees		Satchler Set SI		Satchler Set SII	
$R_C$	1.25	(1.25)	1.2	(1.2)	1.2	(1.2)
$V_R$	53.26	(53.20)	56.80	(56.10)	54.80	(55.16)
$r_R$	1.162	(1.172)	1.122	(1.13)	1.14	(1.139)
$a_R$	0.75	(0.75)	0.75	(0.75)	0.75	(0.75)
$W_{VOL}$	3.74	(3.50)	3.0	(2.70)	3.0	(2.65)
$r_{VOL}$	1.32	(1.32)	1.33	(1.33)	1.33	(1.33)
$a_{VOL}$	0.66	(0.615)	0.696	(0.667)	0.672	(0.65)
$W_{SURF}$	6.27	(6.11)	6.49	(6.72)	6.86	(7.09)
$r_{SURF}$	1.32	(1.32)	1.33	(1.33)	1.33	(1.33)
$a_{SURF}$	0.66	(0.615)	0.696	(0.667)	0.672	(0.65)
$V_{LS}$	6.20	(6.20)	6.4	(6.4)	6.1	(6.1)
$r_{LS}$	1.01	(1.01)	1.12	(1.12)	1.14	(1.125)
$a_{LS}$	0.75	(0.75)	0.75	(0.75)	0.75	(0.75)
$X^2/N$	1.4	(2.6)	1.4	(1.6)	1.1	(1.8)
$\sigma_{D+E}^{(2^+)}_1$	0.215	(.212)	0.235	(.208)	0.229	(.203)
$\sigma_{D+E}^{(4^+)}_1$	0.0674	(.0629)	0.0727	(.0613)	0.0717	(.0599)
$\sigma_{D+E}^{(6^+)}_1$	0.0431	(.0256)	0.0456	(.0241)	0.0455	(.0237)

Table 3. Deformation Lengths and Transition Strengths for  $^{138}\text{Ba}$  and  $^{144}\text{Sm}$ .

$^{138}\text{Ba}$				$^{144}\text{Sm}$			
Ex Energy	J	$\beta_L R'$	G(L)	Ex Energy	J	$\beta_L R'$	G(L)
1436	$2^+$	0.43	6.1	1661	$2^+$	$0.46(0.44)^a$	$8.7(6.6)^a$
2218	$2^+$	0.23	1.7	2423	$2^+$	$0.29(0.29)$	$3.5(2.9)$
2639	$2^+$	0.07	0.2	2800	$2^+$	0.14	0.8
3339	$2^+$	0.15	0.7	1811	$3^-$	$0.87(0.82)$	$34.0(24.4)$
3368	$2^+$	0.17	1.0	3227	$3^-$	0.07	0.3
2881	$3^-$	0.75	18.4	2191	$4^+$	$0.33(0.32)$	$5.8(4.3)$
1898	$4^+$	0.31	4.1	2588	$4^+$	0.21	2.3
2308	$4^+$	0.21	1.9	2883	$4^+$	0.25	3.2
2584	$4^+$	0.08	0.2	3020	$4^+$	0.23	2.8
2779	$4^+$	0.12	0.6	2324	$(6^+)$	$0.11^b$ 0.18	$1.0^b$ 2.8
3156	$4^+$	0.07	0.2	3308	$6^+$	0.15	1.8
2090	$6^+$	0.26	5.1				
2201	$(6^+)$	0.15	1.7				

<sup>a</sup>Numbers in parenthesis are from Ref. 13.

<sup>b</sup>These numbers represent the extreme credible fits to the data.



Table 4. Effective Charges for Transitions in  $^{138}\text{Ba}$ .

Transition	$L^{b)}$	$\delta_e^{c)}$
$0^+ 2_1^+$	2	0.82 .2
$0^+ 4_1^+$	4	0.86 .2
$0^+ 6_1^+$	6	0.61 .2
$0^+ 2_2^+$	2	0.98 .2
$0^+ 4_2^+$	4	1.07 .2
$0^+ (6_2^+)^a)$	6	0.73 .2

<sup>a</sup>This state has not been unambiguously assigned  $6^+$ , but its angular distribution, together with the shell-model predictions, suggest this assignment.

<sup>b</sup>This is the L-transfer for the dominant amplitude. Non-normal parity amplitudes also contribute to the cross section, and are included in the calculations. See Ref. 24.

<sup>c</sup>Calculated from the relationship  $[(1+\delta_e(1+2N/Z))]^2 = \sigma_{\text{exp}}/\sigma_{\text{theory}}$  where the theoretical cross section  $\sigma_{\text{theory}}$  is calculated using the shell model wave functions described in the text.

Table 5. Major Components of  $0_1^+$  and  $6_2^+$  Wave Functions Calculated With Both Interactions, and the Resulting Transition Densities.

$ 0^+\rangle_{\text{g.s.}}$	$= -0.675 (g_7)^6\rangle - 0.674 (g_7)^4(d_5)^2\rangle - 0.286 (g_7)^2(d_5)^4\rangle$	$>: A=136-140$	
$ 0^+\rangle_{\text{g.s.}}$	$= -0.517 (g_7)^6\rangle - 0.740 (g_7)^4(d_5)^2\rangle - 0.419 (g_7)^2(d_5)^4\rangle$	$>: A=136-145$	
$ 6_2^+\rangle$	$= 0.599 (g_7)^6\rangle - 0.559 (g_7)^5(d_5)^1\rangle - 0.318 (g_7)^3(d_5)^3\rangle - 0.316 (g_7)^4(d_5)^2\rangle$	$>: A=136-140$	
$ 6_2^+\rangle$	$= 0.573 (g_7)^6\rangle - 0.303 (g_7)^5(d_5)^1\rangle - 0.246 (g_7)^3(d_5)^3\rangle - 0.621 (g_7)^4(d_5)^2\rangle$	$>: A=136-145$	
	$\langle g_{7/2}   a^\dagger a   g_{7/2} \rangle$	$\langle g_{7/2}   a^\dagger a   d_{5/2} \rangle$	$\langle d_{5/2}   a^\dagger a   g_{7/2} \rangle$
A=136-140	0.1292	0.1049	0.2174
A=136-145	0.1765	0.0800	0.1178

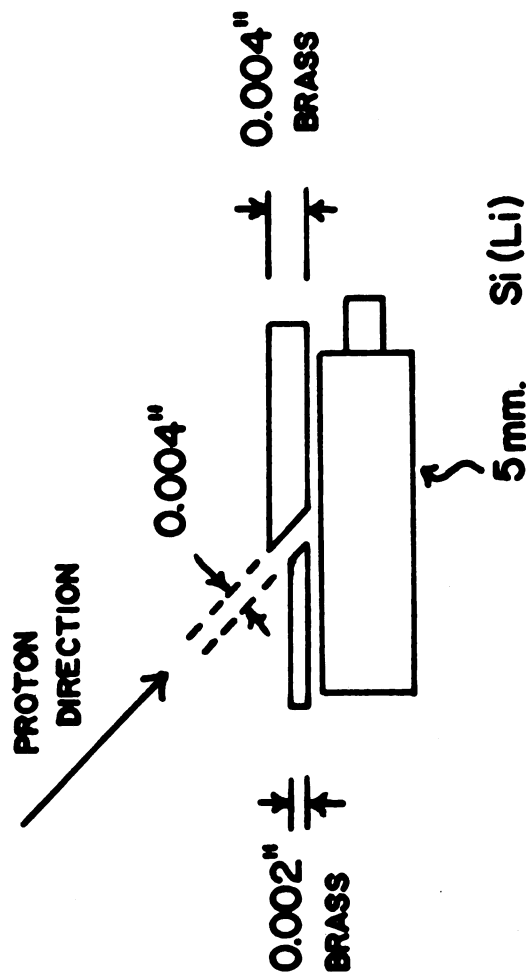
Table 6. Comparison of D and D+E Cross Sections for Various Interactions in  $^{138}\text{Ba}$

	$2_1^+D$	$2_1^+D+E$	$4_1^+D$	$4_1^+D+E$	$6_1^+D$	$6_1^+D+E$	$4_1^+D+E$ $2_1^+D+E$	$6_1^+D+E$ $2_1^+D+E$
CAL	.00994	0.299	.00417	0.170	0.00562	0.195	0.569	0.652
COP	3.456	0.936	0.846	0.241	0.343	0.460	0.257	0.491
CE-I	0.357	1.832	0.0921	0.818	0.0489	0.767	0.447	0.419
F-V	0.268	0.191	0.0691	0.191	0.0357	0.334	1.00	1.749
ROSENFELD	0.437	0.166	0.110	0.166	0.0517	0.320	1.00	1.928
SOPER	1.360	1.584	0.330	0.426	0.129	0.210	0.269	0.133
SERBER	2.135	3.691	0.521	1.196	0.210	0.777	0.324	0.211

**APPENDIX B**

**FIGURES**

# DETECTOR SETUP — ELASTIC PEAK



## DETECTOR

Figure 1. Slit and counter arrangement of high resolution measurement-optimization-stabilization system located in the focal plane of the spectrograph. The experimental parameters are adjusted until the maximum amount of elastically scattered beam passes between the brass jaws, thus insuring minimum line widths of the groups of scattered particles along the focal plane.

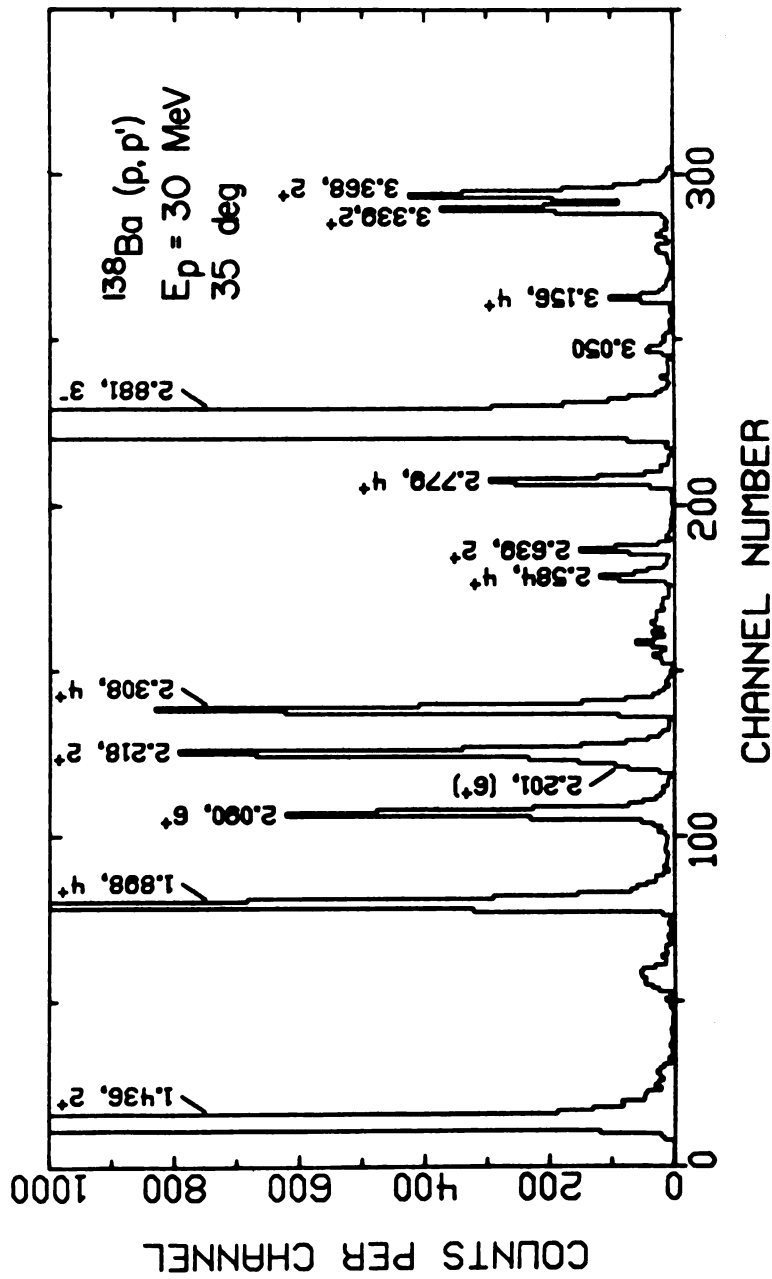


Figure 2. Spectrum of  $^{138}\text{Ba}(p, p')$  at 35 degrees, with resolution of about 10 keV, FWHM. The broad bumps correspond to protons which scatter from Mg and Si impurities and because of kinematic differences have different planes of focus in the spectrograph. The yields of the  $2^+$  state at 1436 keV and of the  $3^-$  state at 2881 keV were too intense to be counted on this plate.

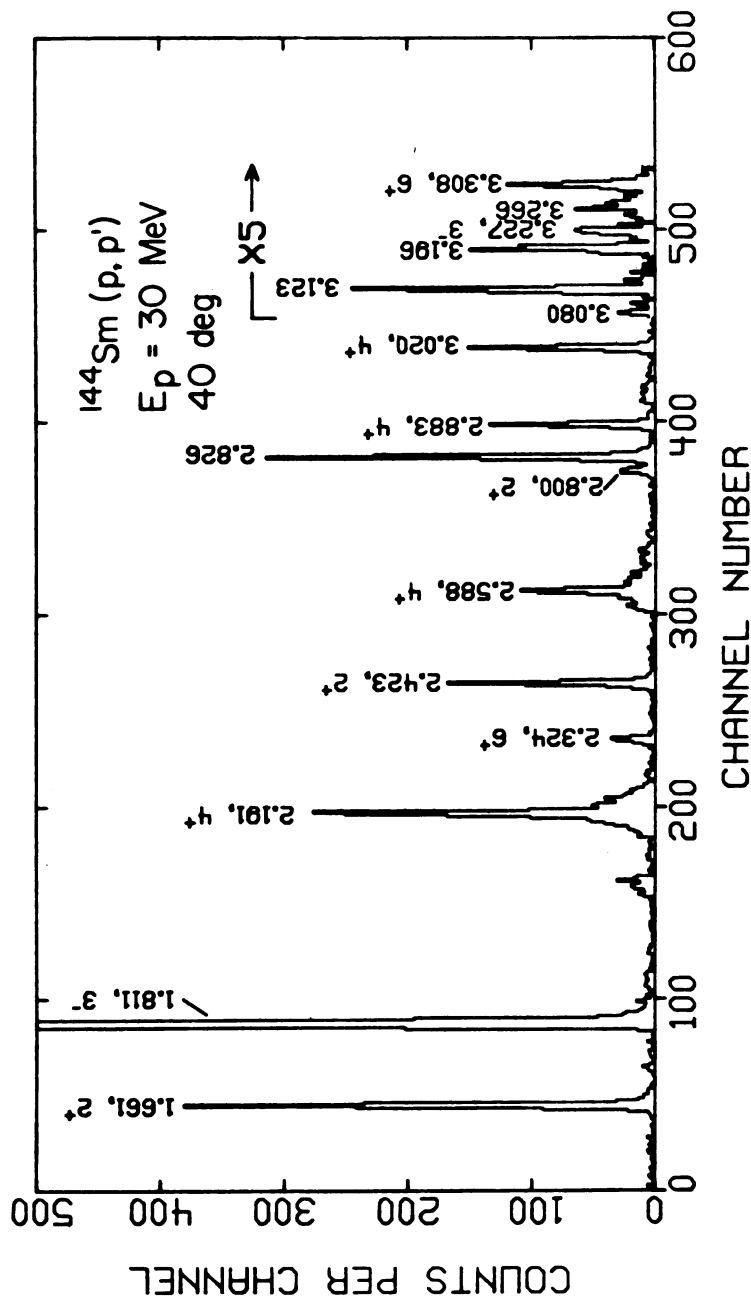


Figure 3. Spectrum from  $^{144}\text{Sm}(p,p')$  at 40 degrees, with resolution of about 7 keV, FWHM. The broad bumps under certain of the peaks correspond to protons which scatter from Mg and Si impurities, as in the  $^{138}\text{Ba}$  spectrum. The yield of the  $3^-$  state at 1811 keV was too intense to be counted on this plate.

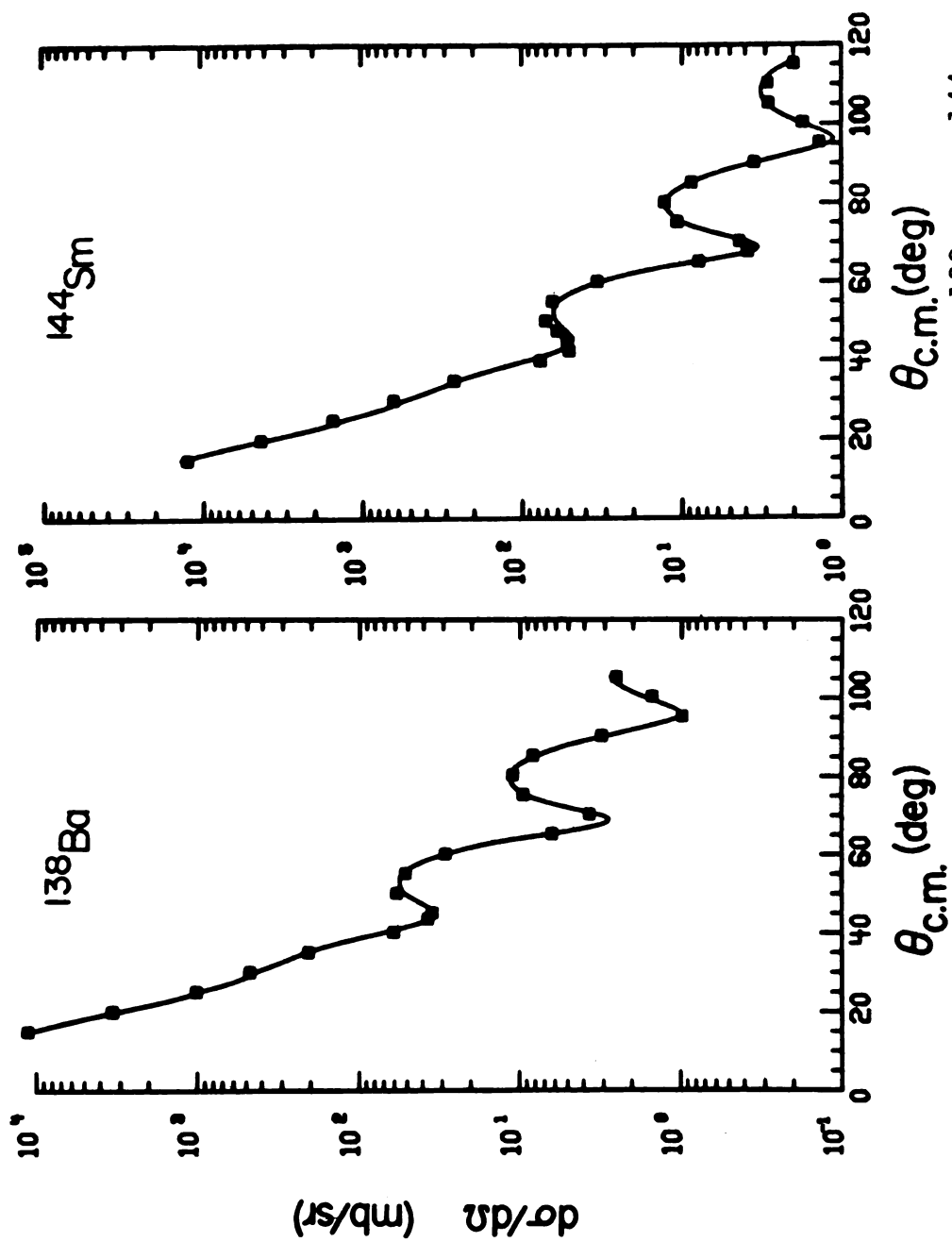


Figure 4. Elastic scattering angular distributions measured for  $^{138}\text{Ba}$  and  $^{144}\text{Sm}$ . The curves are results of optical model calculations made with the optical model parameters of Becchetti and Greenlees (Ref. 34).



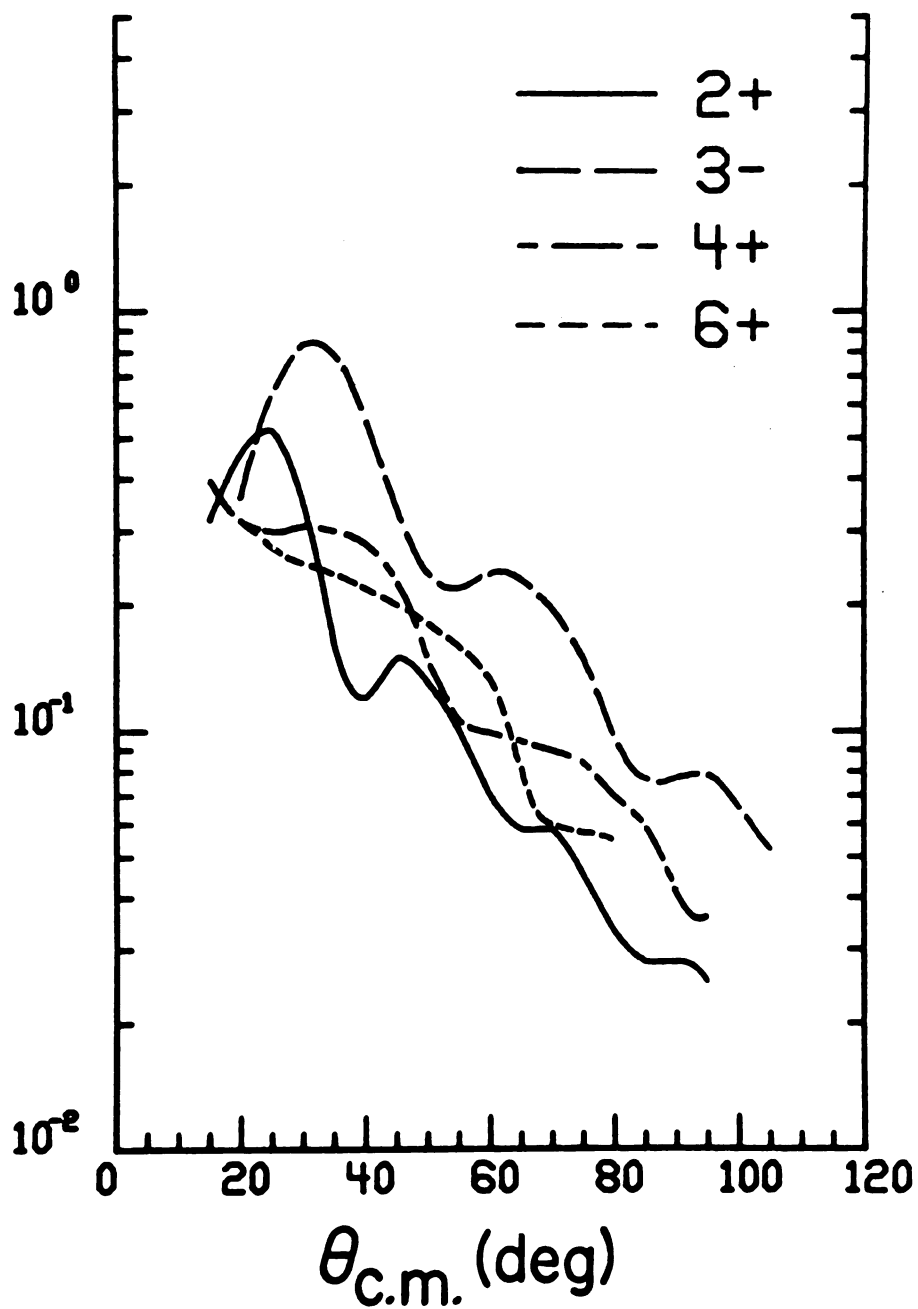


Figure 5. Characteristic curves obtained by averaging our measured angular distributions from groups of states in  $^{138}\text{Ba}$  and  $^{144}\text{Sm}$  which had previously assigned  $J^\pi$  values.

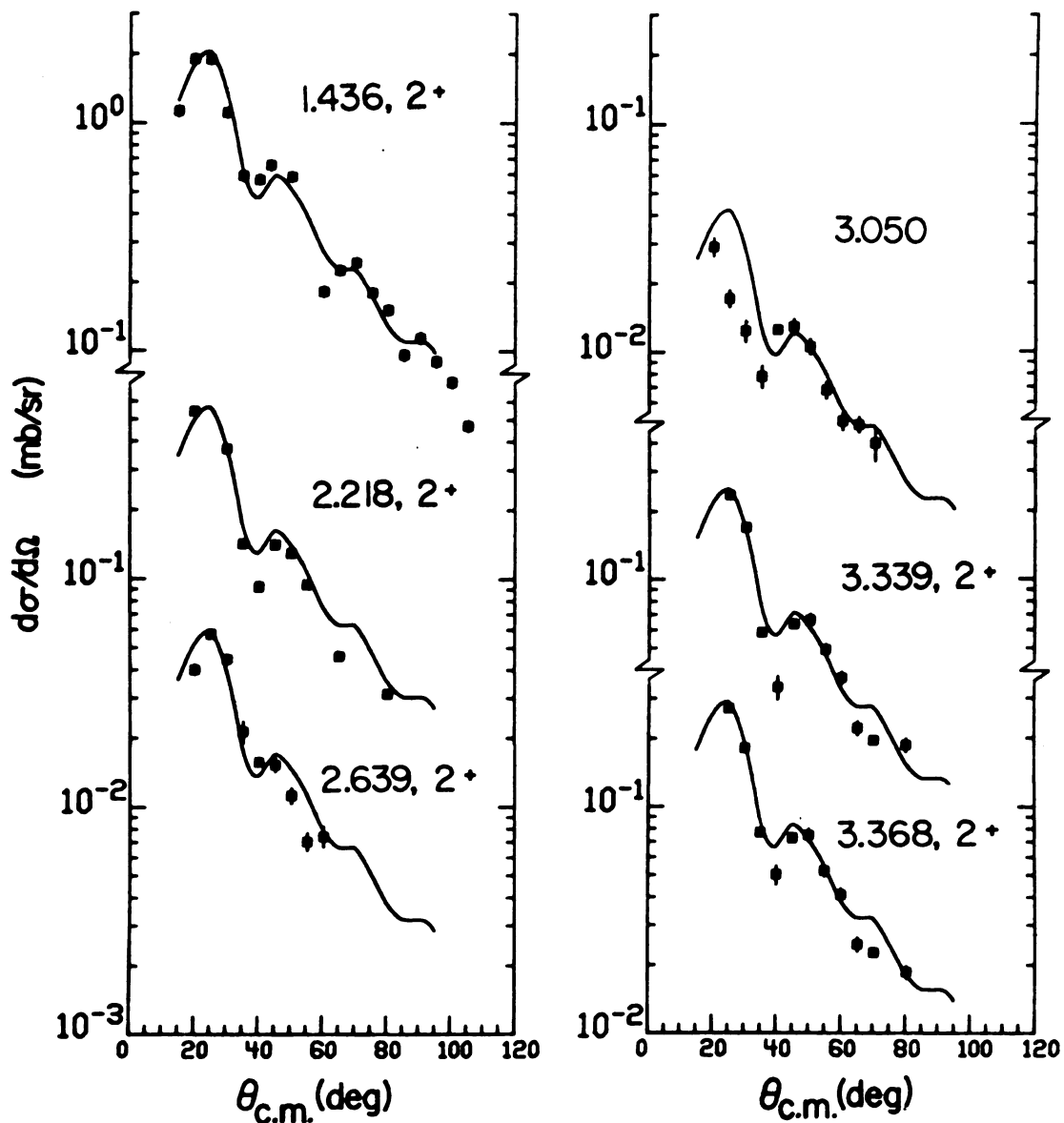


Figure 6. States in  $^{138}\text{Ba}$  which have angular distributions in agreement with the characteristic  $2^+$  shape, which is the line drawn through the data. We assign all of these states  $J^\pi = 2^+$  with the exception of the state at 3050 keV.

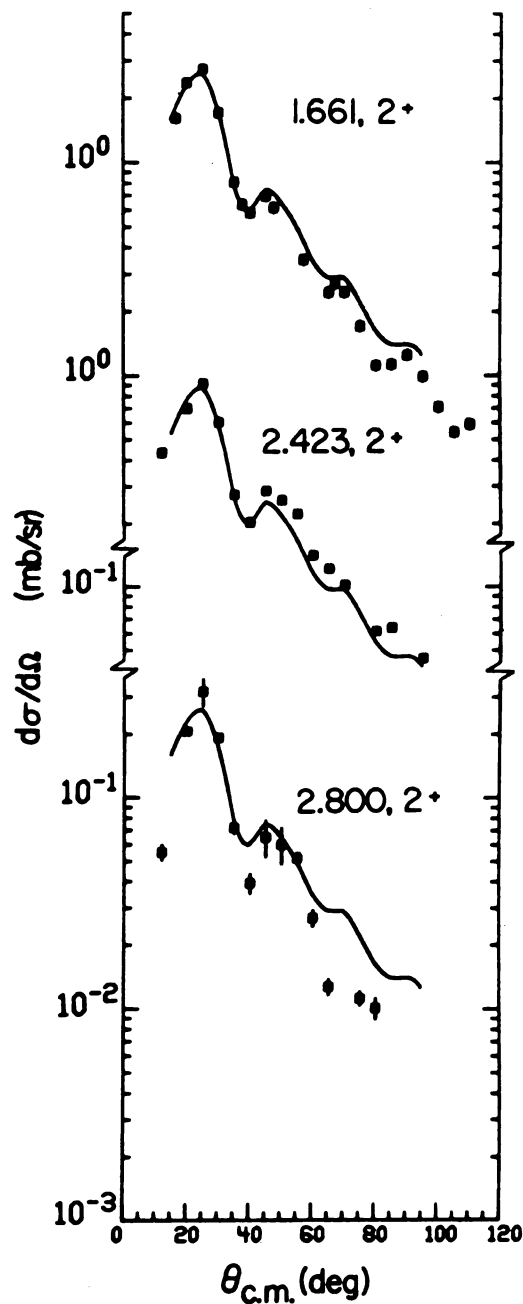


Figure 7. States in  $^{144}\text{Sm}$  which have angular distributions in agreement with the characteristic  $2^+$  shape, which is the line drawn through the data. We assign all of these states  $J^\pi = 2^+$ .

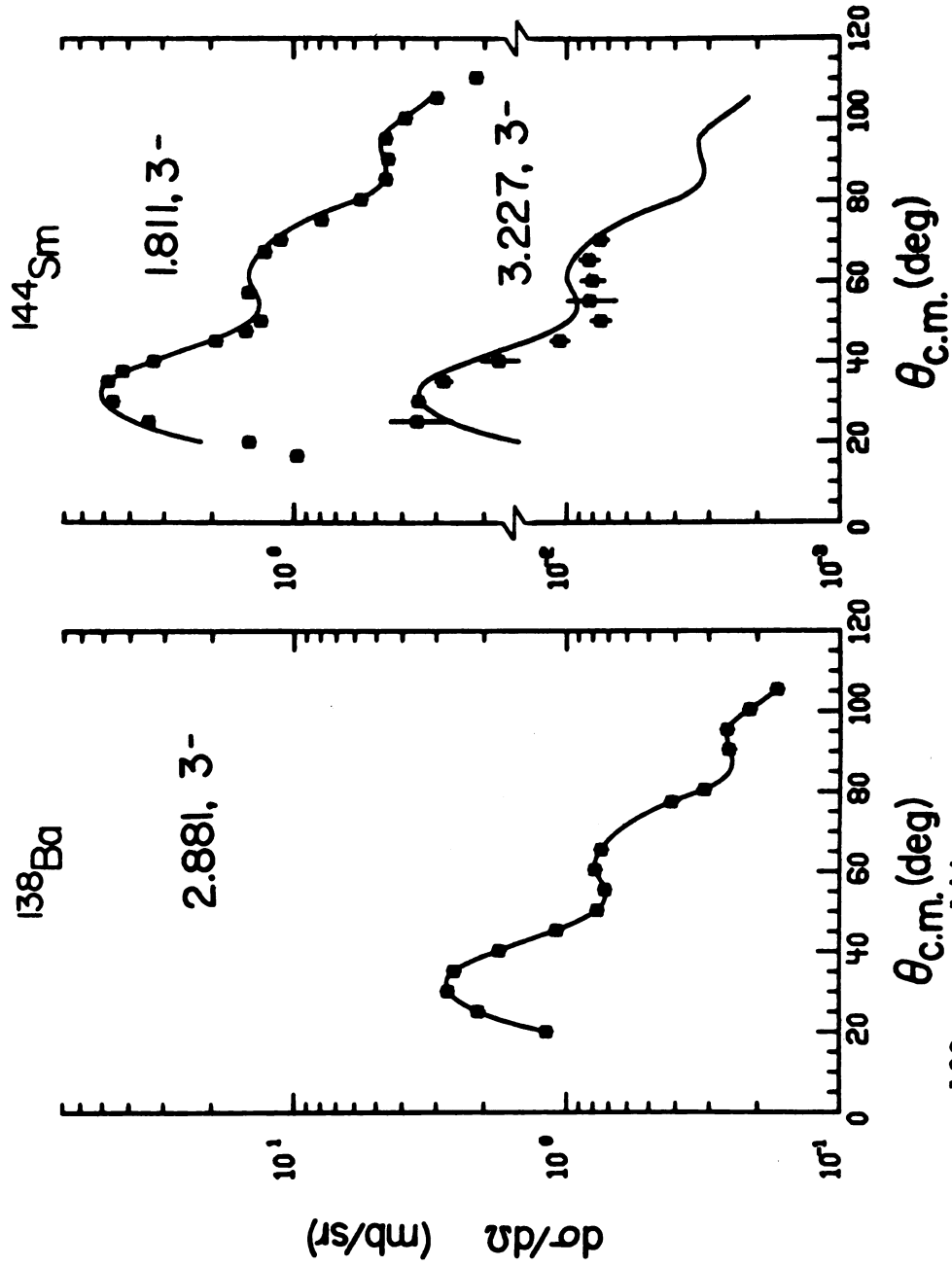


Figure 8. States in  $^{138}\text{Ba}$  and  $^{144}\text{Sm}$  which have angular distributions in agreement with the characteristic  $3^-$  shape, which is the line drawn through the data. We assign these states  $J_{\pi} = 3^-$ .

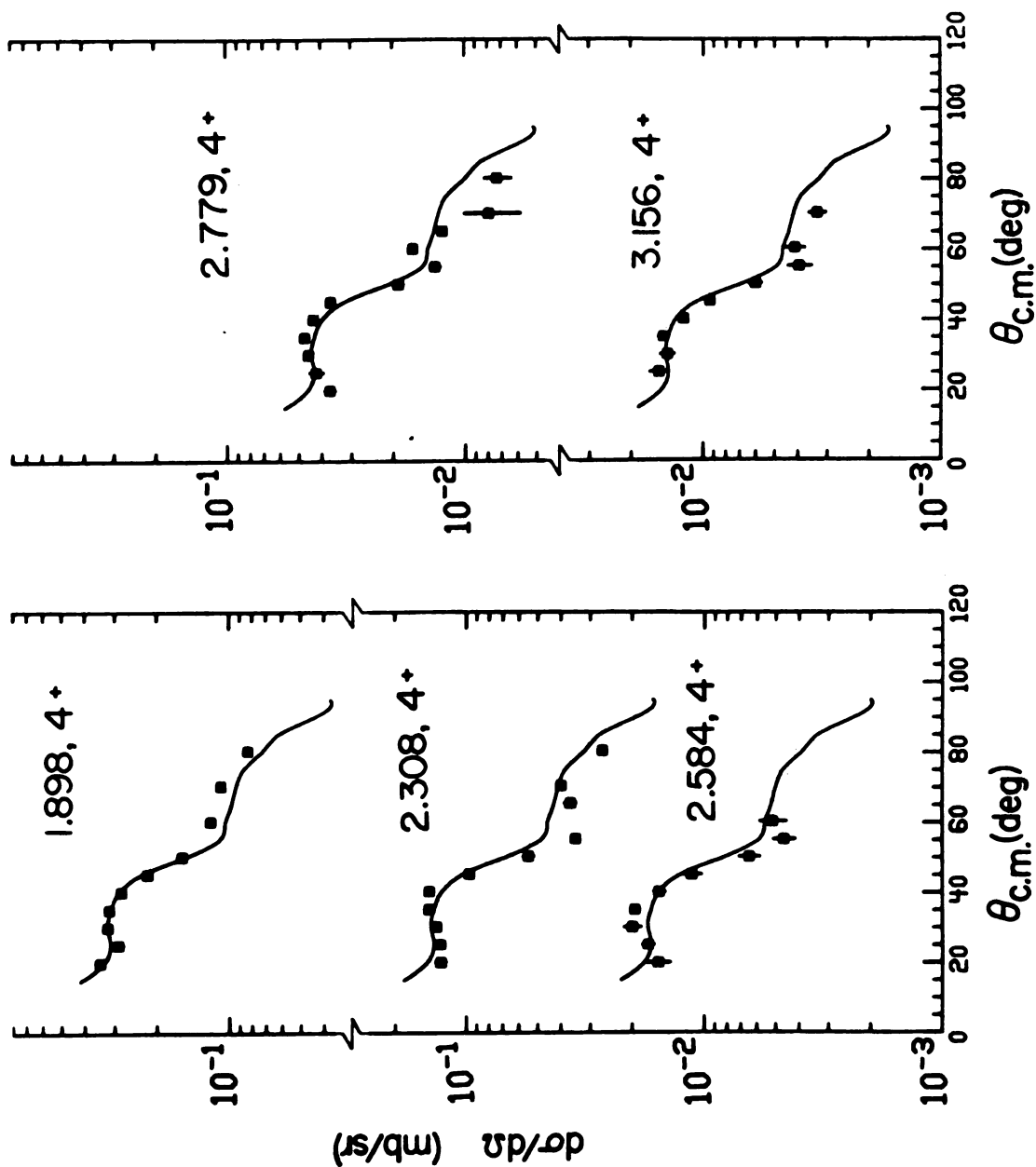


Figure 9. States in  $^{138}\text{Ba}$  which have angular distributions in agreement with the character-  
istic  $4^+$  shape, which is the line drawn through the data. We assign all of these states  $J^\pi = 4^+$ .

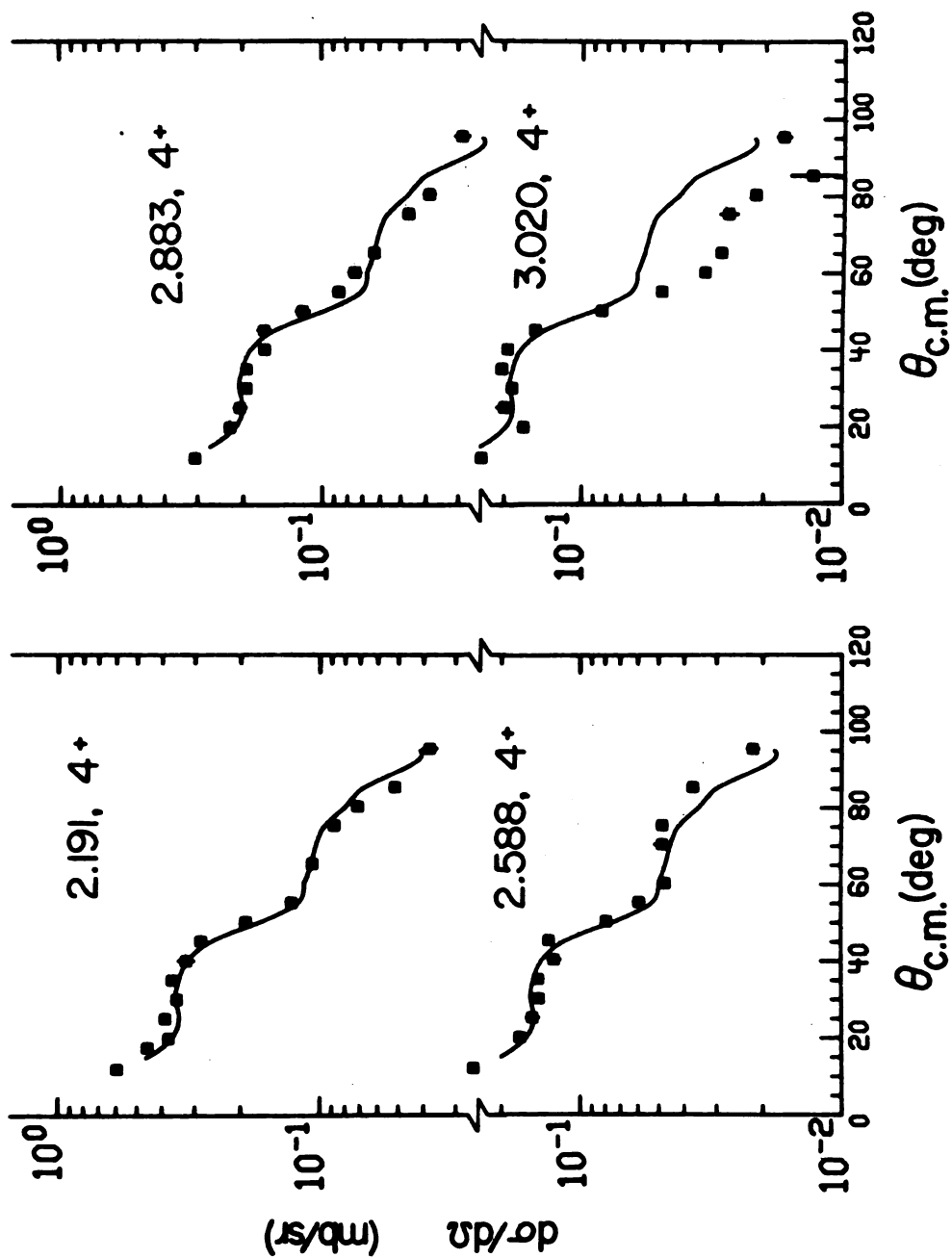


Figure 10. States in  $^{144}\text{Sm}$  which have angular distributions in agreement with the characteristic  $4^+$  shape, which is the line drawn through the data. We assign all of these states  $J^\pi = 4^+$ .

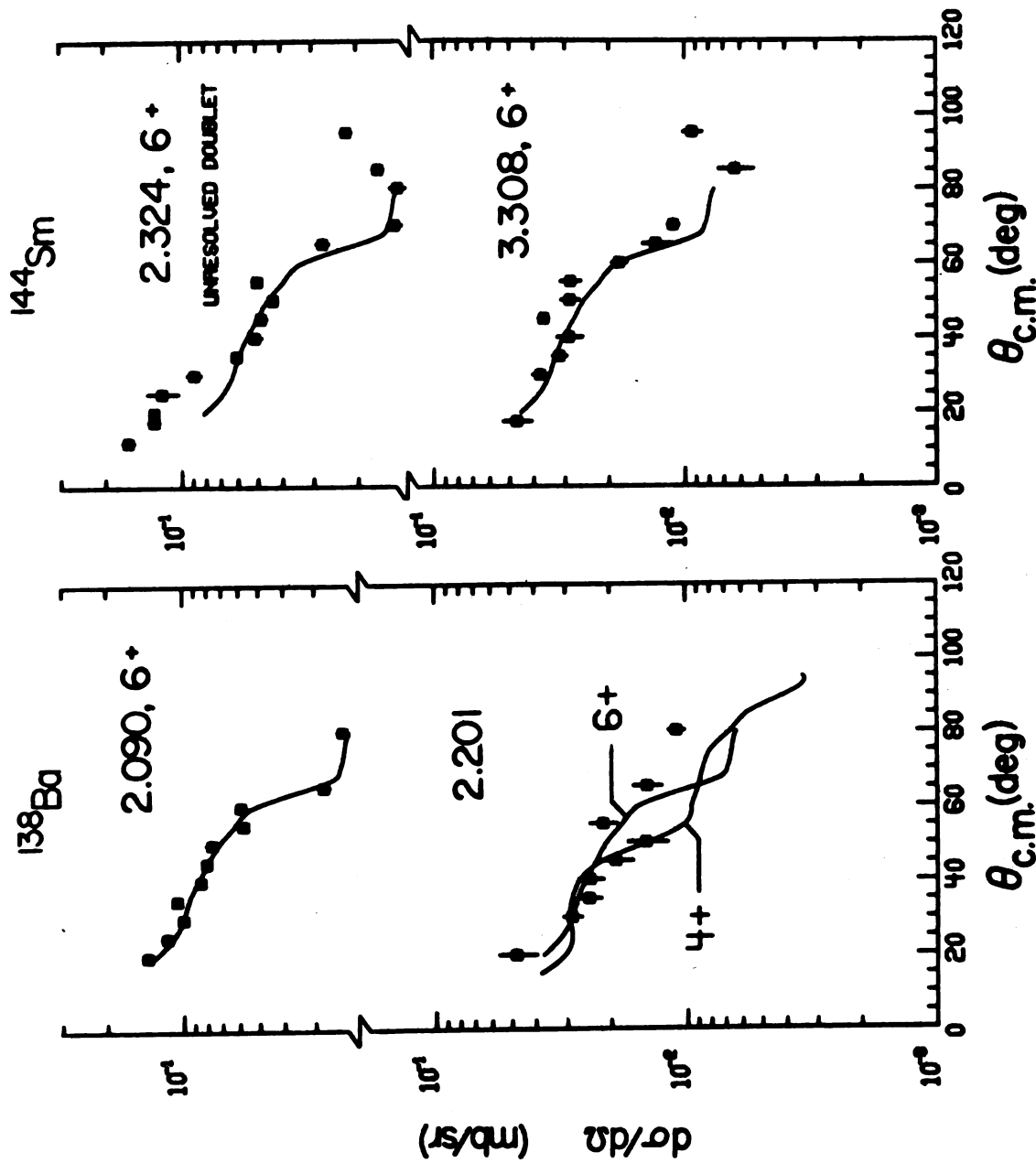


Figure 11. Angular distributions for the previously assigned 6<sup>+</sup> state at 2090 keV, and the weak 2201 keV member of a doublet in <sup>138</sup>Ba. Both the 4<sup>+</sup> and 6<sup>+</sup> characteristic curves are drawn through this angular distribution. The 2324 keV state in <sup>144</sup>Sm has been assigned 6<sup>+</sup>, but due to the rise of the data at forward angles, this state may be a close lying doublet. We assign J<sup>π</sup>=6<sup>+</sup> to the 3308 keV state in <sup>144</sup>Sm.

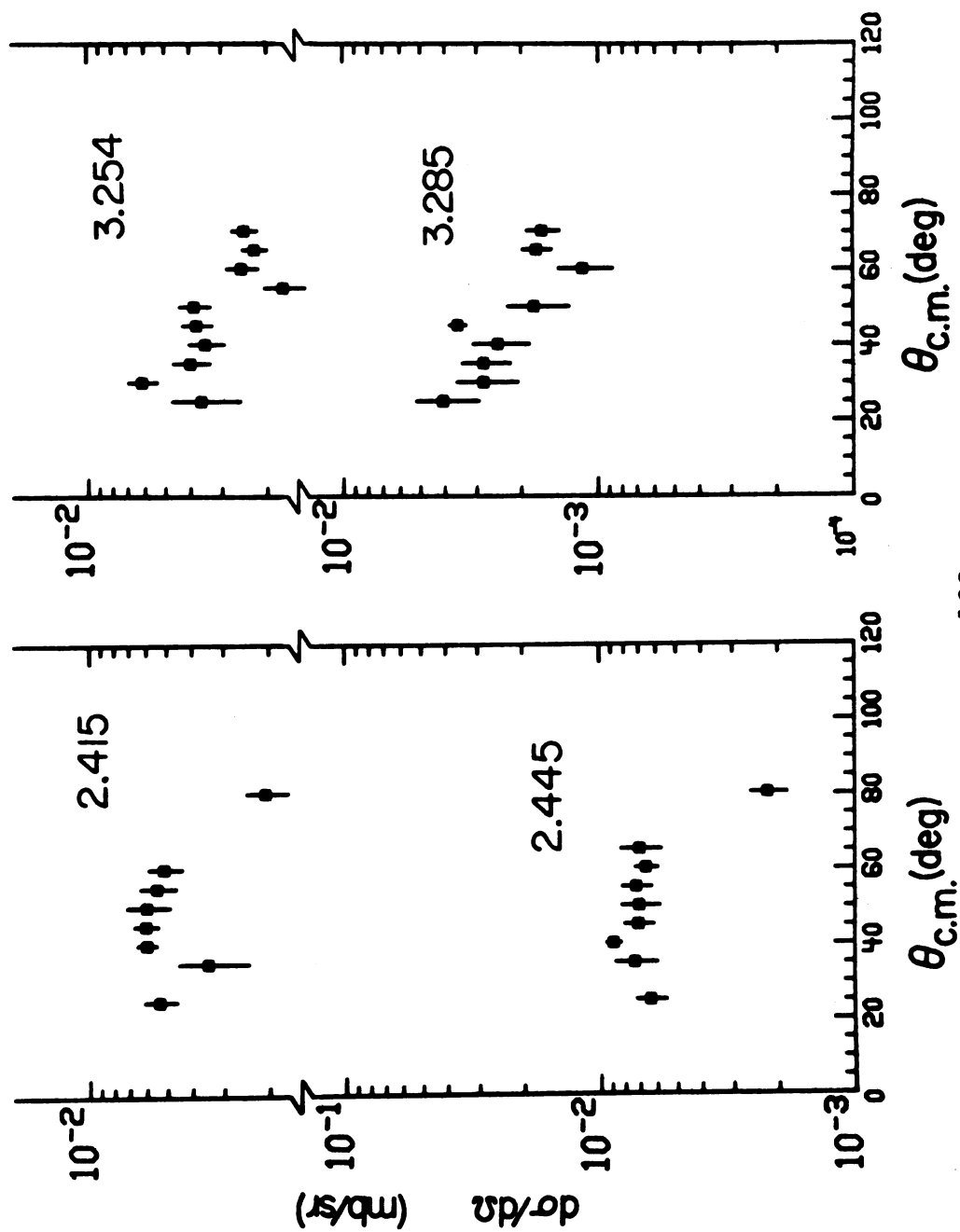


Figure 12. Angular distributions of states in  $^{138}\text{Ba}$  for which no  $J^\pi$  assignment could be made from this work. Spins of 5<sup>+</sup> and 3<sup>+</sup> have been suggested for the states at 2415 and 2445 keV respectively (Ref. 37).



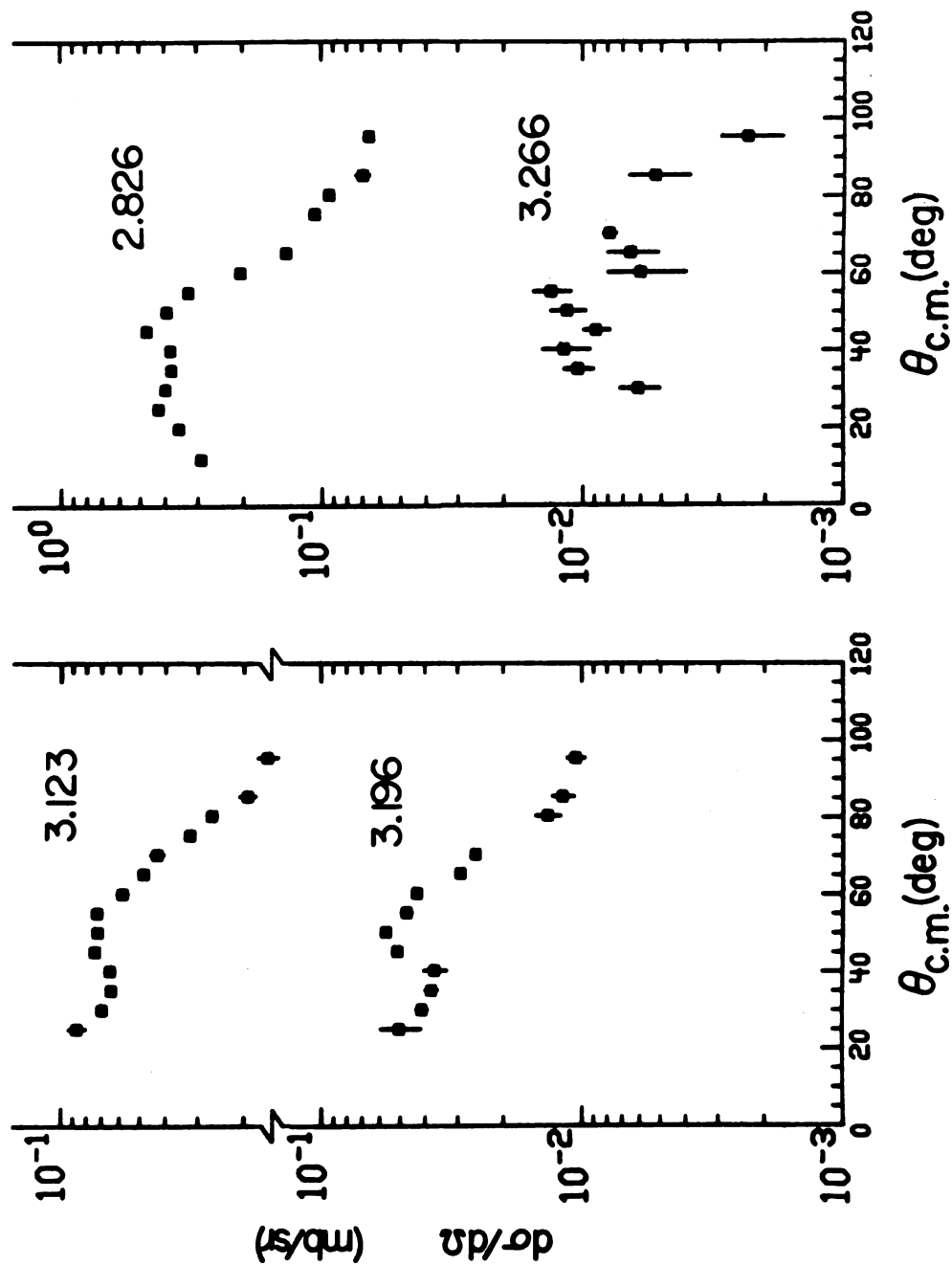


Figure 13. Angular distributions of states in  $^{144}\text{Sm}$  for which no  $J^\pi$  assignment could be made from this work. The state at 3123 keV has been assigned  $J^\pi = (7^-)$  in Ref. 11.



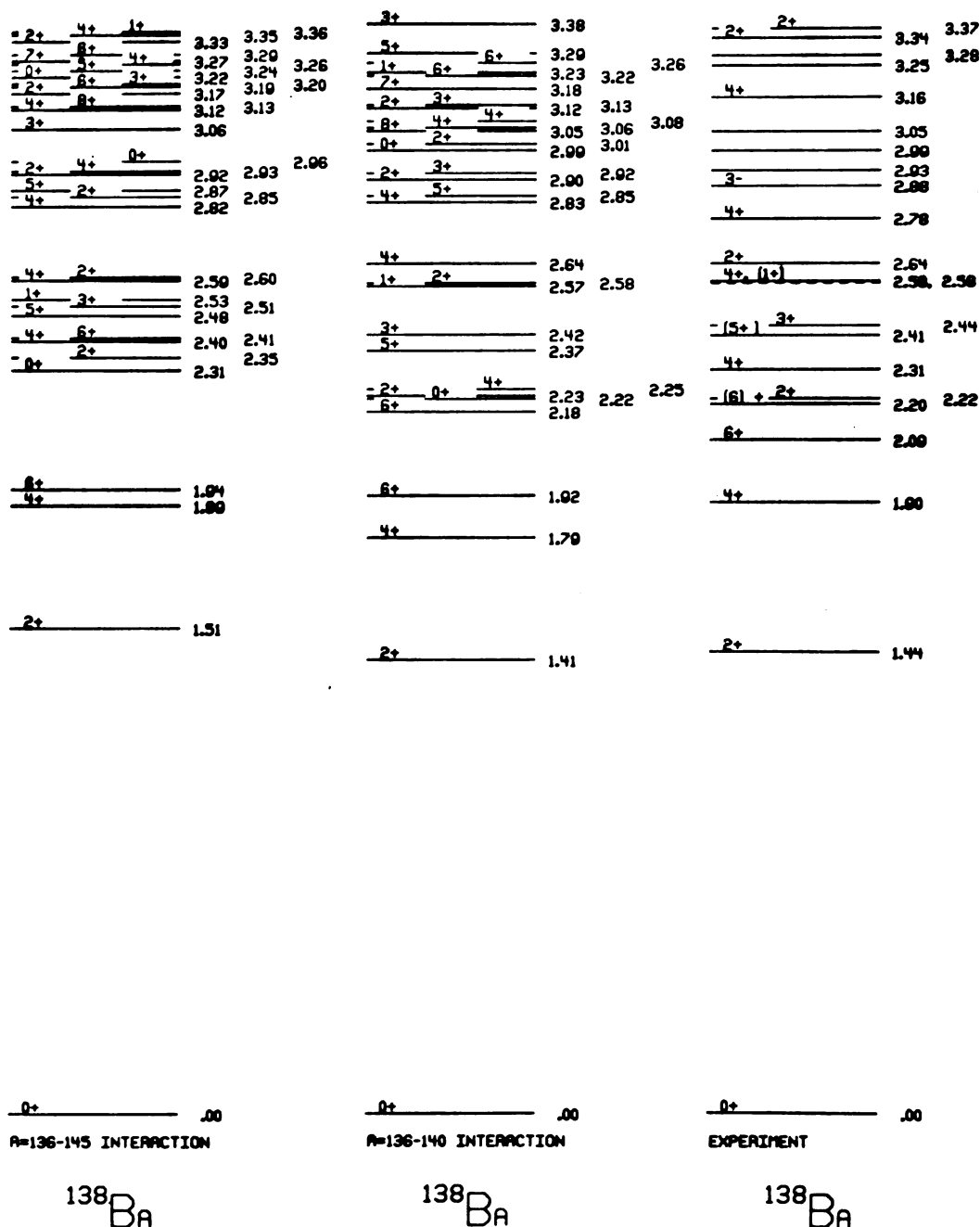


Figure 14. Comparison of results of shell model calculations discussed in Sec. IVA with experimentally known energy levels in  $^{138}\text{Ba}$ .

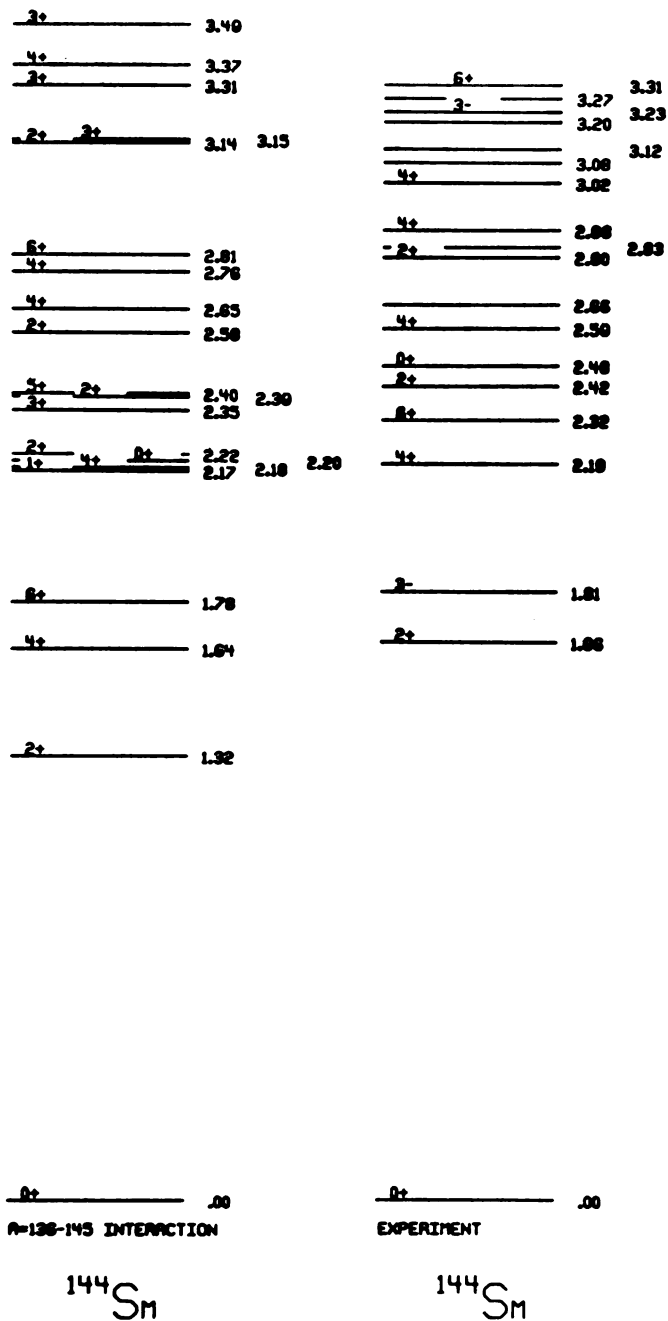


Figure 15. Comparison of results of shell model calculations discussed in Sec. IVA with experimentally known energy levels in  $^{144}\text{Sm}$ .

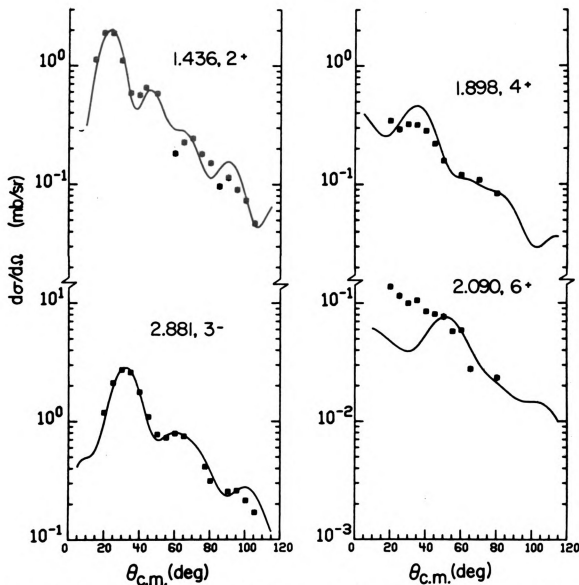


Figure 16. Results of collective model calculations for inelastic scattering on  $^{138}\text{Ba}$ . The optical model parameters given in Table 2, Set SII were used, and both the real and imaginary parts of the optical model were deformed. The calculations shown are for the lowest  $2^+$ ,  $3^-$ ,  $4^+$  and  $6^+$  states.

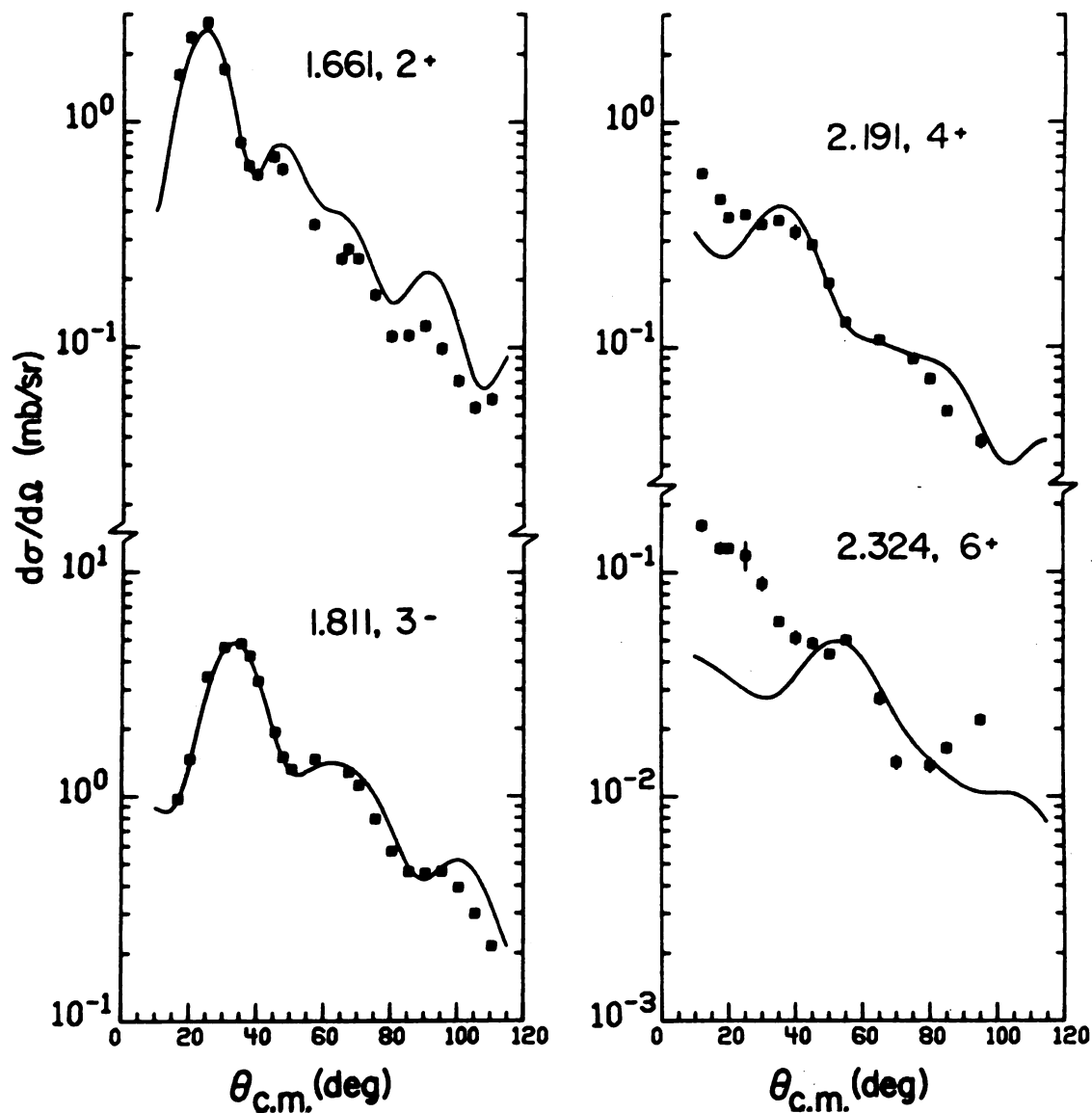


Figure 17. Results of collective model calculations for inelastic scattering on  $^{144}\text{Sm}$ . The optical model parameters given in Table 2, Set SI were used, and both the real and imaginary parts of the optical model were deformed. The calculations shown are for the lowest  $2^+$ ,  $3^-$ ,  $4^+$  and  $6^+$  states.

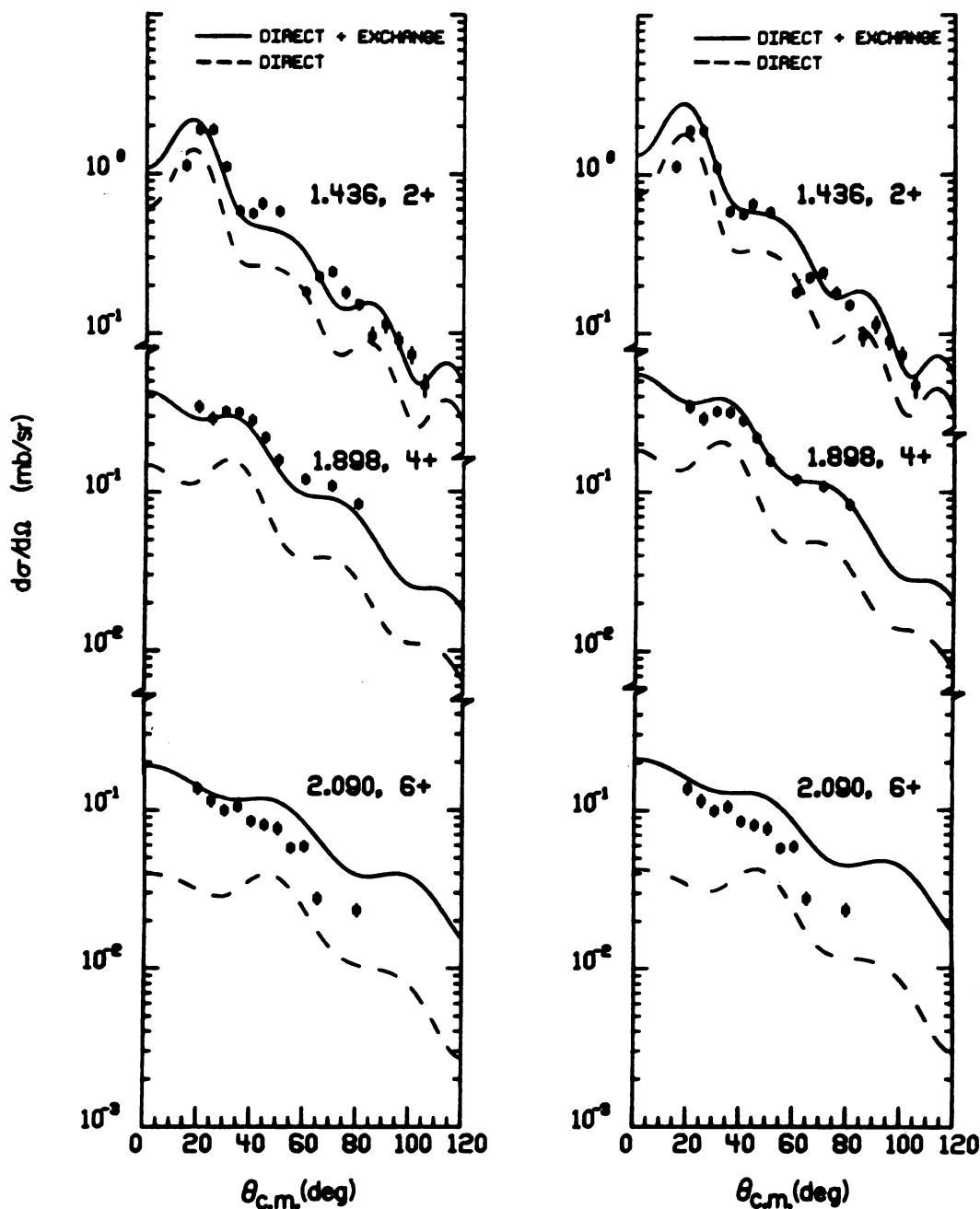


Figure 18. Microscopic model DWBA calculations for the inelastic scattering to the  $2_1^+$ ,  $4_1^+$  and  $6_1^+$  states in  $^{138}\text{Ba}$ . The calculations are identical except for the wave functions; the left hand column employed the A=136-140 set while the A=136-145 set was used for the right hand column. Both sets of wave functions predict very similar angular distributions.

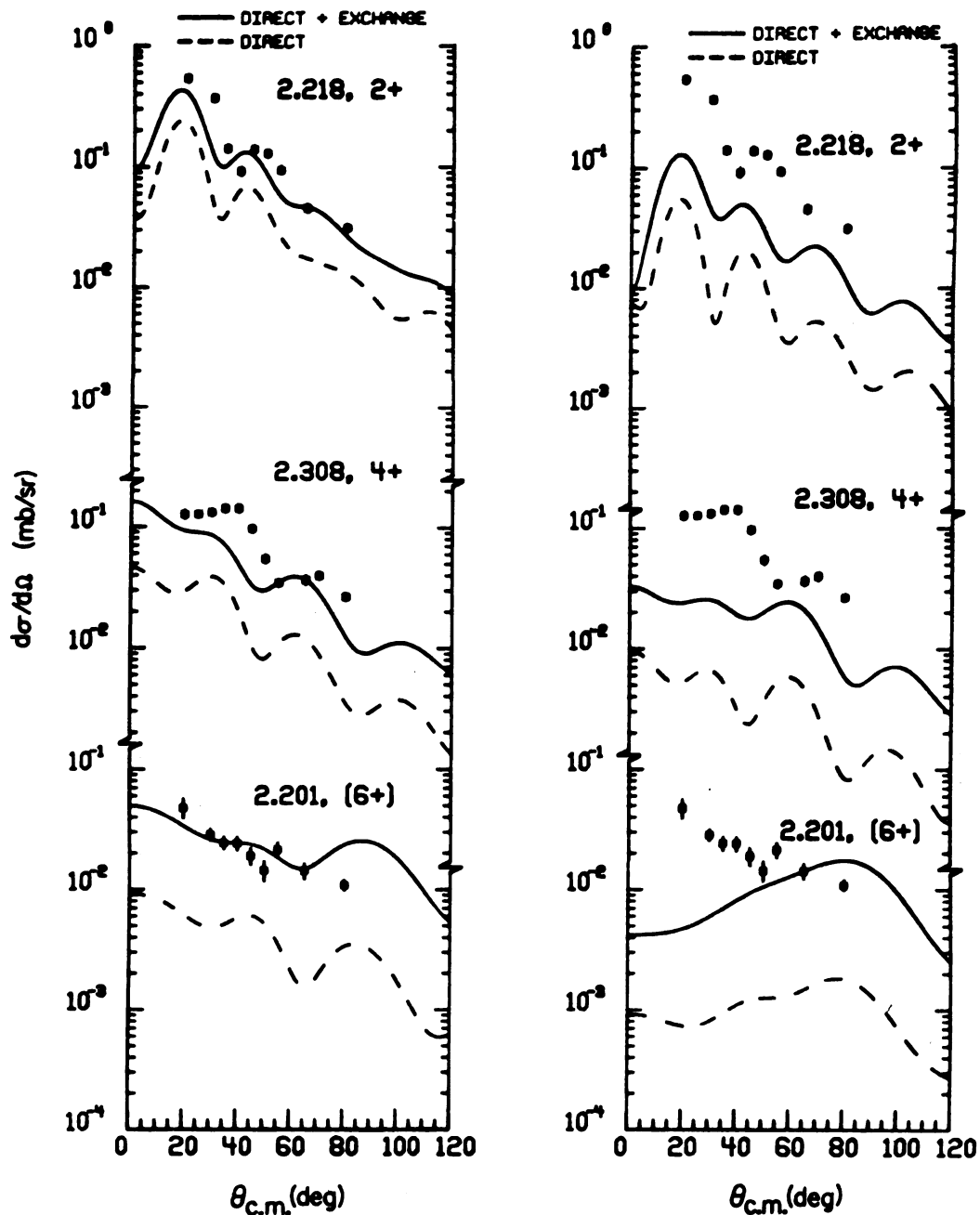


Figure 19. Microscopic model DWBA calculations for the inelastic scattering to the  $2_2^+$ ,  $4_2^+$  and  $6_2^+$  states in  $^{138}\text{Ba}$ . The calculations are identical except for the wave functions; the left hand column employed the A=136-140 set while the A=136-145 set was used for the right hand column. These calculations indicate that the A=136-140 set of wave functions provides the better description of the low lying states in  $^{138}\text{Ba}$ .



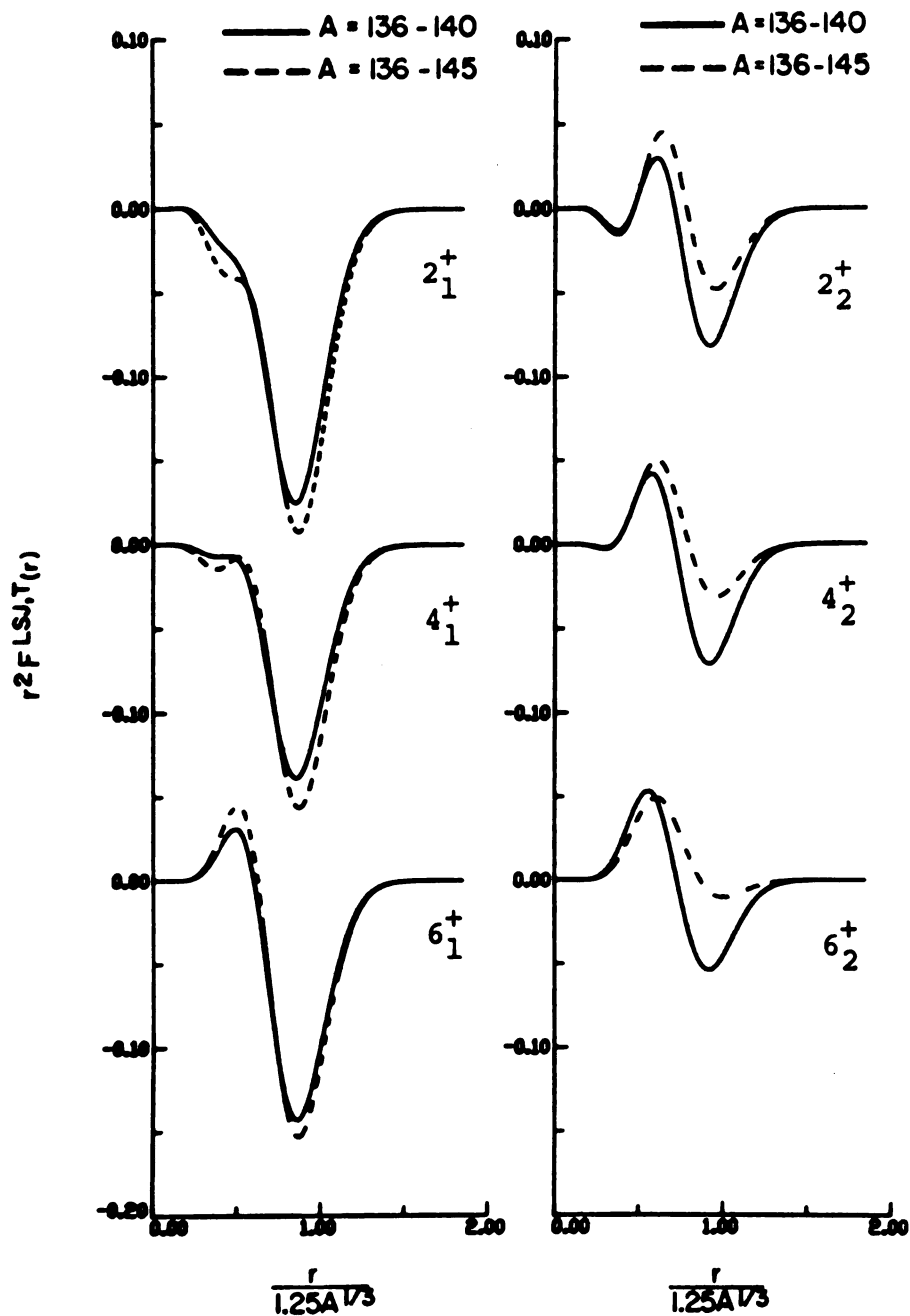


Figure 20. Transition densities for the  $2_1^+$ ,  $2_2^+$ ,  $4_1^+$ ,  $4_2^+$  and  $6_1^+$ ,  $6_2^+$  states in  $^{138}\text{Ba}$  calculated with both sets of wave functions. The  $2_1^+$ ,  $4_1^+$  and  $6_1^+$  densities are very similar, and predict very similar cross sections. The differences in the  $2_2^+$ ,  $4_2^+$  and  $6_2^+$  cross sections are directly related to the differences in the transition densities for these states.



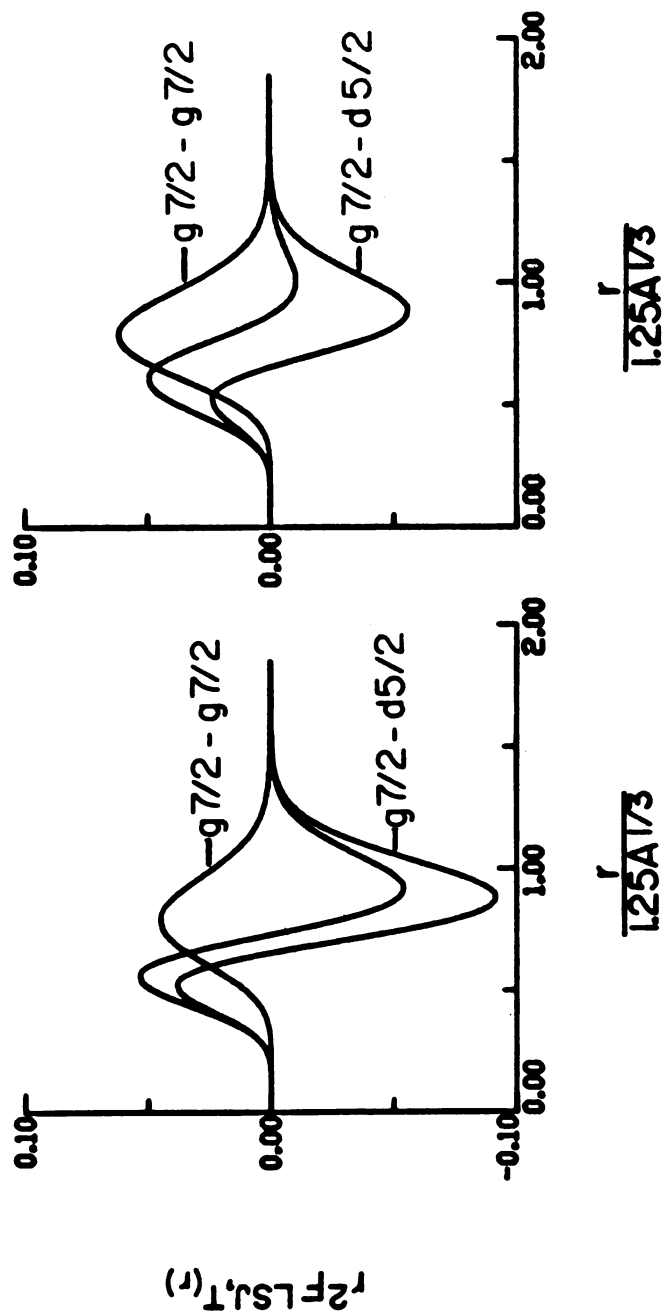


Figure 21. Composition of the  $6_2^+$  transition density in  $^{138}\text{Ba}$ , calculated with both sets of wave functions. The left hand figure is calculated with the A=136-140 set while the right hand column is calculated with the A=136-145 set.

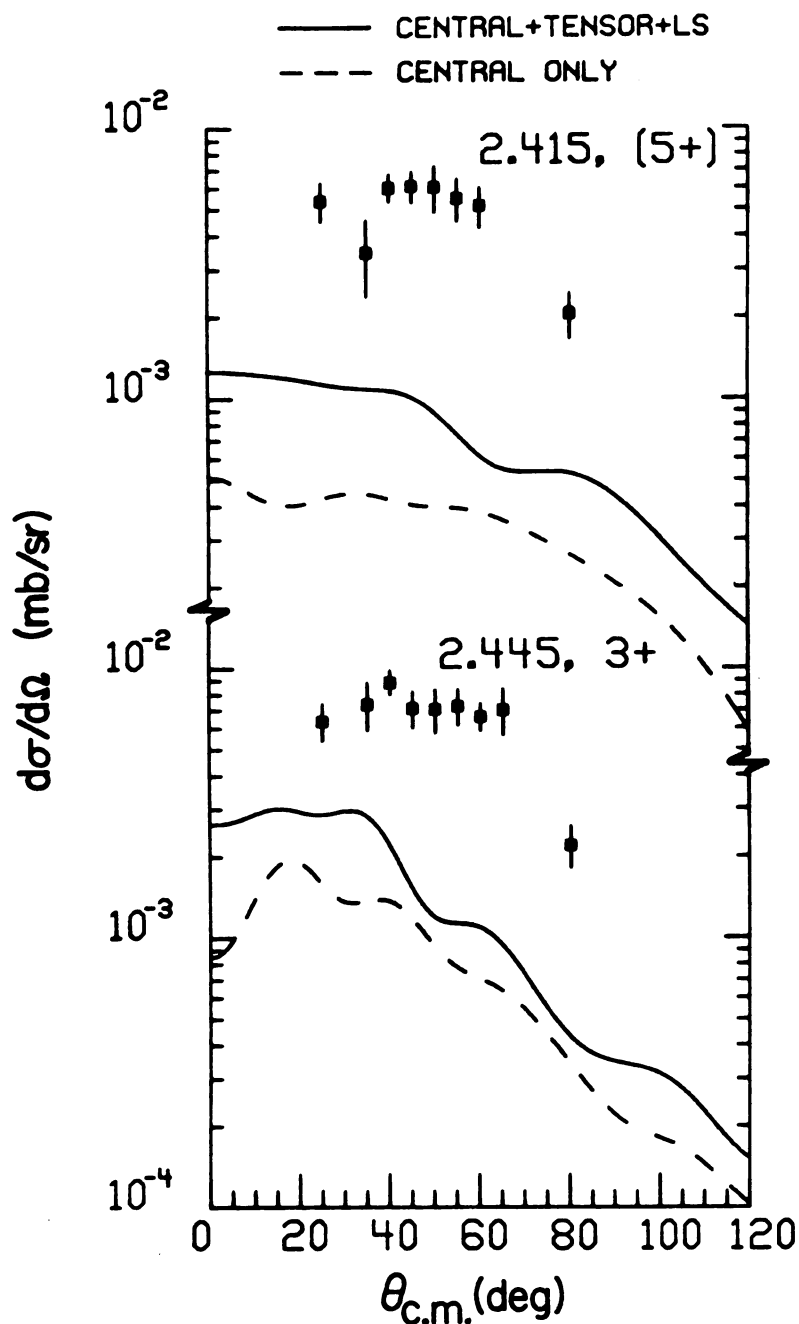


Figure 22. Microscopic model DWBA calculations for inelastic scattering to the  $3^+$  and  $5^+$  states in  $^{138}\text{Ba}$  calculated with the A=136-140 set of wave functions. The two-body force included central, tensor and L-S terms, but no collective enhancement was included. Only the Direct + Exchange calculations are shown.

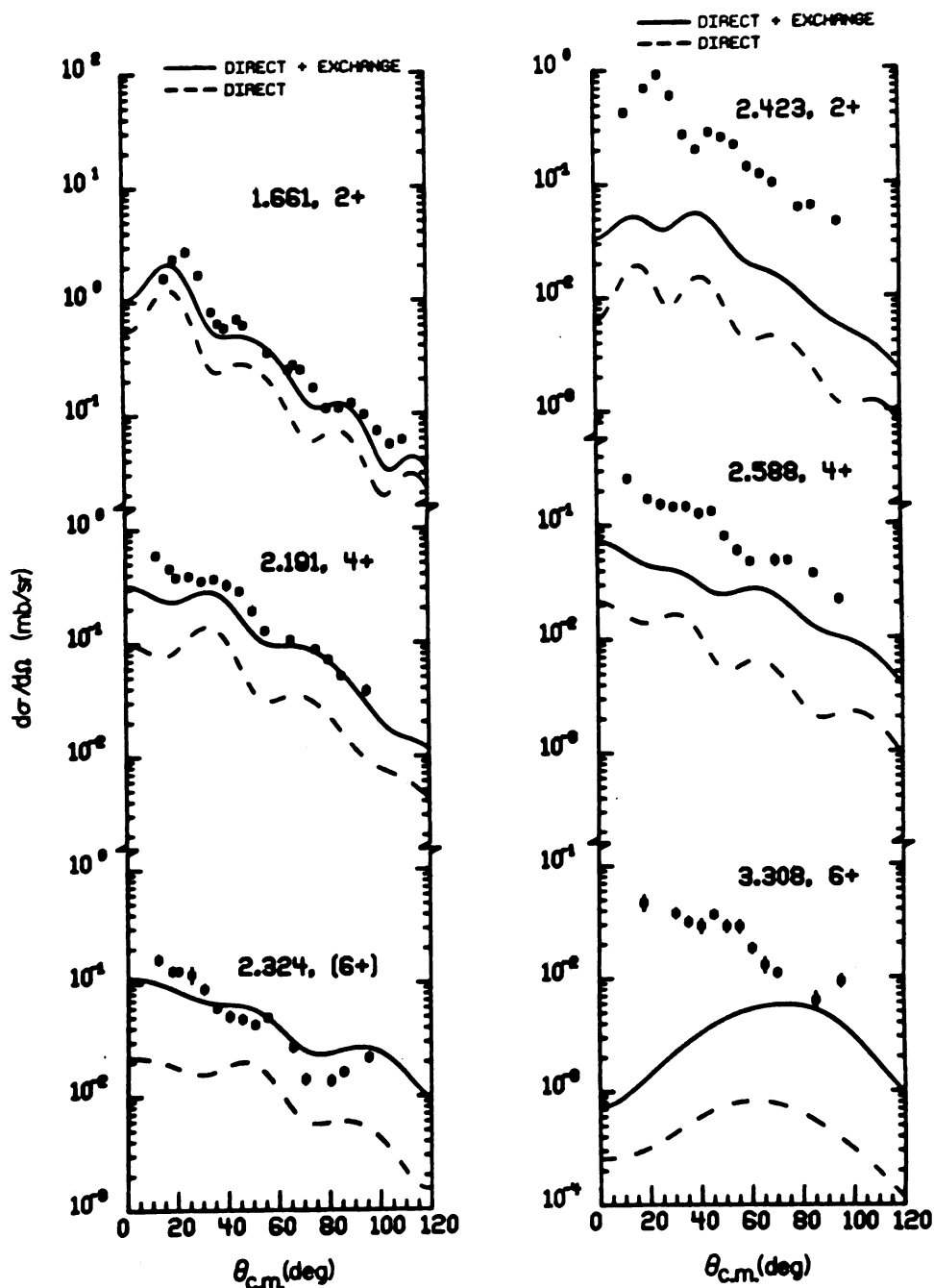


Figure 23. Microscopic model DWBA calculations for inelastic scattering to the  $2^+_{1/2}$ ,  $4^+_{1/2}$  and  $6^+_{1/2}$  states in  $^{144}\text{Sm}$  calculated with the A=136-145 set of wave functions. The inadequacy of the basis space is demonstrated in the calculated angular distributions for the  $2^+_{1/2}$ ,  $4^+_{1/2}$  and  $6^+_{1/2}$  states.

**APPENDIX C**  
**COMPILATION OF EXPERIMENTAL ANGULAR DISTRIBUTIONS**

# BA138(P,P) ELASTIC CROSS SECTION

EP=30.0 MEV. EX= 000 MEV.					
ANG(CM) (DEG)	DSIGMA(CM) (MB/SR)	STAT.ERR. (MB/SR)	TOTAL ERR. (MB/SR)	ANG(LAB) (DEG)	DSIGMA(LAB) (MB/SR)
15.1	1.14E+04	.021E+04	.040E+04	15.0	1.16E+04
20.1	3.39E+03	.045E+03	.111E+03	20.0	3.44E+03
25.2	1.02E+03	.008E+03	.032E+03	25.0	1.04E+03
30.2	4.79E+02	.028E+02	.146E+02	30.0	4.85E+02
35.2	2.08E+02	.017E+02	.065E+02	35.0	2.10E+02
40.3	6.13E+01	.033E+01	.187E+01	40.0	6.20E+01
43.8	3.75E+01	.021E+01	.114E+01	43.5	3.79E+01
45.3	3.52E+01	.025E+01	.103E+01	45.0	3.56E+01
50.3	5.91E+01	.019E+01	.178E+01	50.0	5.96E+01
55.4	5.20E+01	.023E+01	.159E+01	55.0	5.24E+01
60.4	2.94E+01	.018E+01	.090E+01	60.0	2.96E+01
65.4	6.40E+00	.054E+00	.199E+00	65.0	6.44E+00
70.4	3.74E+00	.024E+00	.115E+00	70.0	3.76E+00
75.4	9.67E+00	.063E+00	.297E+00	75.0	9.70E+00
80.4	1.13E+01	.006E+01	.034E+01	80.0	1.13E+01
85.4	8.43E+00	.041E+00	.256E+00	85.0	8.44E+00
90.4	3.15E+00	.013E+00	.095E+00	90.0	3.15E+00
95.4	9.95E+01	.051E+01	.303E+01	95.0	9.94E+01
100.4	1.53E+00	.005E+00	.046E+00	100.0	1.53E+00
105.4	2.55E+00	.008E+00	.077E+00	105.0	2.54E+00

BA138(P,P') 2+

ANG(CM) (DEG)	DSIGMA(CM) (MB/SR)	STAT.ERR. (MB/SR)	TOTAL ERR. (MB/SR)	EX= 1.436 MEV.	ANG(LAB) (DEG)	DSIGMA(LAB) (MB/SR)
15.1	1.13E+00	.030E+00	.085E+00		15.0	1.15E+00
20.2	1.89E+00	.014E+00	.133E+00		20.0	1.32E+00
25.2	1.89E+00	.006E+00	.133E+00		25.0	1.32E+00
30.2	1.11E+00	.005E+00	.078E+00		30.0	1.12E+00
35.3	5.87E-01	.035E-01	.412E-01		35.0	5.34E-01
40.3	5.64E-01	.035E-01	.397E-01		40.0	5.71E-01
43.8	6.52E-01	.166E-01	.486E-01		43.5	5.60E-01
50.3	5.81E-01	.031E-01	.408E-01		50.0	5.87E-01
60.4	1.82E-01	.022E-01	.129E-01		60.0	1.84E-01
65.4	2.26E-01	.025E-01	.160E-01		65.0	2.27E-01
70.4	2.44E-01	.021E-01	.172E-01		70.0	2.45E-01
75.4	1.80E-01	.085E-01	.152E-01		75.0	1.81E-01
80.4	1.51E-01	.022E-01	.108E-01		80.0	1.52E-01
85.4	9.61E-02	1.031E-02	1.231E-02		85.0	9.62E-02
90.4	1.14E-01	.111E-01	.135E-01		90.0	1.14E-01
95.4	9.01E-02	.885E-02	1.087E-02		95.0	9.00E-02
100.4	7.31E-02	.727E-02	.889E-02		100.0	7.29E-02
105.4	4.70E-02	.698E-02	.772E-02		105.0	4.68E-02



BA138(P,P1) 4+

		EP=29.8 MEV.		EX= 1.898 MEV.	
ANG(CM)	DSIGMA(CM)	STAT.ERR.	TOTAL ERR.	ANG(LAB)	DSIGMA(LAB)
(DEG)	(MB/SR)	(MB/SR)	(MB/SR)	(DEG)	(MB/SR)
20.2	3.45E+01	.145E+01	.282E+01	20.0	3.30E+01
25.2	2.91E+01	.153E+01	.254E+01	25.0	2.95E+01
30.2	3.22E+01	.037E+01	.229E+01	30.0	3.27E+01
35.3	3.18E+01	.051E+01	.228E+01	35.0	3.22E+01
40.3	2.83E+01	.095E+01	.220E+01	40.0	2.86E+01
45.3	2.20E+01	.055E+01	.164E+01	45.0	2.23E+01
50.3	1.58E+01	.058E+01	.125E+01	50.0	1.50E+01
60.4	1.20E+01	.029E+01	.089E+01	60.0	1.21E+01
70.4	1.08E+01	.022E+01	.079E+01	70.0	1.09E+01
80.4	8.33E+02	.156E+02	.604E+02	80.0	8.36E+02

HA138(P,P1) 6+

AVG(CM) (DEG)	DSIGMA(CM) (MB/SR)	STAT.ERR. (MB/SR)	TOTAL ERR. (MB/SR)	EX= 2.090 MEV.	AVG(LAB) (DEG)	DSIGMA(LAB) (MB/SR)
20.2	1.38E-01	.067E-01	.117E-01		20.0	1.40E-01
25.2	1.15E-01	.065E-01	.104E-01		25.0	1.17E-01
30.2	9.96E-02	.269E-02	.747E-02		30.0	1.01E-01
35.3	1.06E-01	.037E-01	.083E-01		35.0	1.07E-01
40.3	8.51E-02	.246E-02	.645E-02		40.0	8.61E-02
45.3	8.07E-02	.224E-02	.608E-02		45.0	8.16E-02
50.3	7.66E-02	.448E-02	.699E-02		50.0	7.74E-02
55.4	5.77E-02	.160E-02	.435E-02		55.0	5.82E-02
60.4	5.90E-02	.234E-02	.475E-02		60.0	5.34E-02
65.4	2.77E-02	.138E-02	.238E-02		65.0	2.78E-02
80.4	2.33E-02	.129E-02	.208E-02		80.0	2.34E-02

3A138(P,P1) 2+

ANG(CM) (DEG)	DSIGMA(CM) (MB/SR)	STAT.ERR. (MB/SR)	TOTAL ERR. (MB/SR)	EX= 2.218 MEV.	AVG(LAB) (DEG)	DSIGMA(LAB) (MB/SR)
20.2	5.39E-01	.197E-01	.426E-01		20.0	5.47E-01
30.2	3.70E-01	.072E-01	.268E-01		30.0	3.75E-01
35.3	1.42E-01	.056E-01	.114E-01		35.0	1.44E-01
40.3	9.22E-02	.418E-02	.769E-02		40.0	9.33E-02
45.3	1.40E-01	.050E-01	.110E-01		45.0	1.42E-01
50.3	1.29E-01	.050E-01	.104E-01		50.0	1.31E-01
55.4	9.41E-02	.348E-02	.745E-02		55.0	9.49E-02
65.4	4.57E-02	.206E-02	.381E-02		65.0	4.50E-02
80.4	3.13E-02	.120E-02	.250E-02		80.0	3.14E-02

3A138(P,P') 4+

		EP=29.8 MEV.		EX= 2.308 MEV.	
ANG(CM) (DEG)	DSIGMA(CM) (MB/SR)	STAT.ERR. (MB/SR)	TOTAL ERR. (MB/SR)	AN3(LAB) (DEG)	DSIGMA(LAB) (MB/SR)
20.2	1.28E-01	.069E-01	.113E-01	20.0	1.30E-01
25.2	1.28E-01	.029E-01	.094E-01	25.0	1.30E-01
30.2	1.33E-01	.042E-01	.102E-01	30.0	1.35E-01
35.3	1.44E-01	.034E-01	.106E-01	35.0	1.46E-01
40.3	1.43E-01	.060E-01	.117E-01	40.0	1.45E-01
45.3	9.72E-02	.361E-02	.770E-02	45.0	9.82E-02
50.3	5.47E-02	.299E-02	.486E-02	50.0	5.52E-02
55.4	3.46E-02	.105E-02	.264E-02	55.0	3.49E-02
65.4	3.66E-02	.224E-02	.340E-02	65.0	3.58E-02
70.4	4.00E-02	.166E-02	.326E-02	70.0	4.03E-02
80.4	2.66E-02	.058E-02	.195E-02	80.0	2.67E-02

BA138(P,P') (3+)

		EP=29.8 MEV.		EX= 2.415 MEV.	
ANG(CY)	DSIGMA(CY)	STAT.ERR.	TOTAL ERR.	ANG(LAB)	DSIGMA(LAB)
(DEG)	(MB/SR)	(MB/SR)	(MB/SR)	(DEG)	(MB/SR)
25.2	5.39E+03	.786E+03	.872E+03	25.0	5.47E+03
35.3	3.48E+03	1.074E+03	1.101E+03	35.0	3.52E+03
40.3	6.05E+03	.548E+03	.693E+03	40.0	6.12E+03
45.3	6.10E+03	.659E+03	.785E+03	45.0	6.17E+03
50.3	6.06E+03	1.168E+03	1.243E+03	50.0	6.12E+03
55.4	5.51E+03	.901E+03	.980E+03	55.0	5.56E+03
60.4	5.17E+03	.790E+03	.869E+03	60.0	5.21E+03
80.4	2.07E+03	.391E+03	.417E+03	80.0	2.07E+03

3A138(P,P') 5+

		EP=29.8 MEV.		EX= 2.445 MEV.	
ANG(CM) (DEG)	DSIGMA(CM) (MB/SR)	STAT.ERR. (MB/SR)	TOTAL ERR. (MB/SR)	ANG(LAB) (DEG)	DSIGMA(LAB) (MB/SR)
25.2	6.36E+03	.879E+03	.986E+03	25.0	6.45E+03
35.3	7.35E+03	1.392E+03	1.484E+03	35.0	7.44E+03
40.3	8.87E+03	.606E+03	.867E+03	40.0	8.97E+03
45.3	7.10E+03	.955E+03	1.077E+03	45.0	7.17E+03
50.3	7.04E+03	1.209E+03	1.305E+03	50.0	7.11E+03
55.4	7.24E+03	.976E+03	1.099E+03	55.0	7.30E+03
60.4	6.62E+03	.695E+03	.835E+03	60.0	6.67E+03
65.4	7.02E+03	1.289E+03	1.380E+03	65.0	7.07E+03
80.4	2.20E+03	.365E+03	.397E+03	80.0	2.20E+03

3A138(P,P') 4+

ANG(CM) (DEG)	DSIGMA(CM) (MB/SR)	STAT.ERR. (MB/SR)	TOTAL ERR. (MB/SR)	EX. 2.584 MEV.	ANG(LAB) (DEG)	DSIGMA(LAB) (MB/SR)
20.2	1.55E-02	.179E-02	.209E-02		20.0	1.58E-02
25.2	1.71E-02	.110E-02	.163E-02		25.0	1.74E-02
30.2	2.00E-02	.173E-02	.222E-02		30.0	2.02E-02
35.3	1.95E-02	.094E-02	.166E-02		35.0	1.97E-02
40.3	1.55E-02	.092E-02	.142E-02		40.0	1.56E-02
45.3	1.13E-02	.110E-02	.136E-02		45.0	1.14E-02
50.3	6.46E-03	.673E-03	.811E-03		50.0	6.52E-03
55.4	4.61E-03	.516E-03	.608E-03		55.0	4.65E-03
60.4	5.17E-03	.685E-03	.774E-03		60.0	5.21E-03

BA138(P,P') 2\*

ANG(CM) (DEG)	DSIGMA(CM) (MB/SR)	STAT.ERR. (MB/SR)	TOTAL ERR. (MB/SR)	EX= 2.539 MEV.	ANG(LAB) (DEG)	DSIGMA(LAB) (MB/SR)
20.2	4.02E-02	.201E-02	.346E-02		20.0	4.08E-02
25.2	5.76E-02	.197E-02	.449E-02		25.0	5.84E-02
30.2	4.47E-02	.233E-02	.390E-02		30.0	4.53E-02
35.3	2.14E-02	.243E-02	.286E-02		35.0	2.17E-02
40.3	1.58E-02	.066E-02	.129E-02		40.0	1.50E-02
45.3	1.53E-02	.105E-02	.150E-02		45.0	1.55E-02
50.3	1.12E-02	.090E-02	.119E-02		50.0	1.14E-02
55.4	7.05E-03	.651E-03	.817E-03		55.0	7.11E-03
60.4	7.43E-03	.778E-03	.936E-03		60.0	7.49E-03



3A138(P,P1) 4+

ANG(CM) (DEG)	DSIGMA(CM) (MB/SR)	STAT.ERR. (MB/SR)	TOTAL ERR. (MB/SR)	ANG(LAB) (DEG)	DSIGMA(LAB) (MB/SR)
20.2	3.70E-02	.204E-02	.330E-02	20.0	3.75E-02
25.2	4.21E-02	.295E-02	.417E-02	25.0	4.27E-02
30.2	4.55E-02	.161E-02	.357E-02	30.0	4.51E-02
35.3	4.72E-02	.175E-02	.374E-02	35.0	4.78E-02
40.3	4.34E-02	.193E-02	.360E-02	40.0	4.39E-02
45.3	3.67E-02	.082E-02	.270E-02	45.0	3.71E-02
50.3	1.90E-02	.095E-02	.164E-02	50.0	1.92E-02
55.4	1.33E-02	.073E-02	.118E-02	55.0	1.34E-02
60.4	1.65E-02	.054E-02	.132E-02	60.0	1.56E-02
65.4	1.24E-02	.018E-02	.089E-02	65.0	1.25E-02
70.4	7.93E-03	2.144E-03	2.214E-03	70.0	7.97E-03
80.4	7.30E-03	.985E-03	1.110E-03	80.0	7.32E-03

EP=29.8 MEV. EX= 2.779 MEV.

3A138(P,P') 3-

ANG(CY) (DEG)	DSIGMA(CY) (MB/SR)	STAT.ERR. (MB/SR)	TOTAL ERR. (MB/SR)	EX= 2.881 MEV.	DSIGMA(LAB) (MB/SR)
20.2	1.19E+00	.041E+00	.093E+00	20.0	1.20E+00
25.2	2.11E+00	.066E+00	.162E+00	25.0	2.14E+00
30.2	2.72E+00	.029E+00	.193E+00	30.0	2.76E+00
35.3	2.60E+00	.061E+00	.192E+00	35.0	2.53E+00
40.3	1.77E+00	.039E+00	.130E+00	40.0	1.79E+00
45.3	1.09E+00	.034E+00	.084E+00	45.0	1.11E+00
50.3	7.75E+01	.234E+01	.591E+01	50.0	7.83E+01
55.4	7.28E+01	.315E+01	.599E+01	55.0	7.34E+01
60.4	7.89E+01	.212E+01	.592E+01	60.0	7.36E+01
65.4	7.49E+01	.227E+01	.571E+01	65.0	7.54E+01
77.4	4.13E+01	.176E+01	.339E+01	77.0	4.15E+01
80.4	3.15E+01	.151E+01	.267E+01	80.0	3.15E+01
90.4	2.55E+01	.127E+01	.219E+01	90.0	2.55E+01
95.4	2.59E+01	.104E+01	.209E+01	95.0	2.59E+01
100.4	2.14E+01	.096E+01	.178E+01	100.0	2.14E+01
105.4	1.70E+01	.109E+01	.162E+01	105.0	1.70E+01

BA138(P,P') 1,2

		EP=29.8 MEV.		EX= 3.050 MEV.	
ANG(CM) (DEG)	DSIGMA(CM) (MB/SR)	STAT.ERR. (MB/SR)	TOTAL ERR. (MB/SR)	ANG(LAB) (DEG)	DSIGMA(LAB) (MB/SR)
20.2	2.91E-02	.276E-02	.343E-02	20.0	2.95E-02
25.2	1.72E-02	.155E-02	.196E-02	25.0	1.75E-02
30.2	1.24E-02	.137E-02	.163E-02	30.0	1.26E-02
35.3	7.80E-03	.881E-03	1.037E-03	35.0	7.90E-03
40.3	1.26E-02	.052E-02	.102E-02	40.0	1.27E-02
45.3	1.29E-02	.102E-02	.137E-02	45.0	1.31E-02
50.3	1.06E-02	.082E-02	.110E-02	50.0	1.07E-02
55.4	6.79E-03	.574E-03	.745E-03	55.0	6.85E-03
60.4	4.95E-03	.451E-03	.569E-03	60.0	4.99E-03
65.4	4.78E-03	.378E-03	.505E-03	65.0	4.81E-03
70.4	3.96E-03	.670E-03	.725E-03	70.0	3.98E-03

BA138(P,P1) 4+

ANG(CM) (DEG)	DSIGMA(CM) (MB/SR)	STAT.ERR. (MB/SR)	TOTAL ERR. (MB/SR)	EX. 3.156 MEV.	ANG(LAB) (DEG)	DSIGMA(LAB) (MB/SR)
25.2	1.53E+02	.145E+02	.180E+02	25.0	1.55E+02	
30.2	1.41E+02	.101E+02	.142E+02	30.0	1.43E+02	
35.3	1.47E+02	.076E+02	.128E+02	35.0	1.49E+02	
40.3	1.21E+02	.038E+02	.093E+02	40.0	1.22E+02	
45.3	9.35E+03	.229E+03	.693E+03	45.0	9.45E+03	
50.3	6.05E+03	.399E+03	.582E+03	50.0	6.12E+03	
55.4	3.97E+03	.470E+03	.546E+03	55.0	4.01E+03	
60.4	4.14E+03	.413E+03	.504E+03	60.0	4.18E+03	
70.4	3.34E+03	.292E+03	.374E+03	70.0	3.35E+03	

# BA138(P,P') UNKNOWN

		EP=29.8 MEV.		EX= 3.254 MEV.		
ANG(CM) (DEG)	DSIGMA(CM) (MB/SR)	STAT.ERR. (MB/SR)	TOTAL ERR. (MB/SR)	ANG(LAB) (DEG)	DSIGMA(LAB) (MB/SR)	
25.2	3.62E+03	1.090E+03	1.119E+03	25.0	3.67E+03	
30.2	6.15E+03	.828E+03	.934E+03	30.0	6.24E+03	
35.3	4.00E+03	.675E+03	.731E+03	35.0	4.05E+03	
40.3	3.49E+03	.566E+03	.616E+03	40.0	3.54E+03	
45.3	3.78E+03	.521E+03	.584E+03	45.0	3.82E+03	
50.3	3.86E+03	.544E+03	.607E+03	50.0	3.90E+03	
55.4	1.73E+03	.323E+03	.345E+03	55.0	1.75E+03	
60.4	2.52E+03	.361E+03	.401E+03	60.0	2.54E+03	
65.4	2.24E+03	.256E+03	.300E+03	65.0	2.26E+03	
70.4	2.46E+03	.288E+03	.335E+03	70.0	2.47E+03	

BA138(P,P1) UNKNOWN

ANG(CM) (DEG)	DSIGMA(CM) (MB/SR)	STAT.ERR. (MB/SR)	TOTAL ERR. (MB/SR)	ANG(LAB) (DEG)	DSIGMA(LAB) (MB/SR)
25.2	4.06E-03	1.143E-03	1.178E-03	25.0	4.12E-03
30.2	2.83E-03	.776E-03	.801E-03	30.0	2.87E-03
35.3	2.82E-03	.621E-03	.652E-03	35.0	2.86E-03
40.3	2.49E-03	.637E-03	.660E-03	40.0	2.52E-03
45.3	3.58E-03	.291E-03	.384E-03	45.0	3.52E-03
50.3	1.79E-03	.498E-03	.514E-03	50.0	1.81E-03
60.4	1.15E-03	.285E-03	.296E-03	60.0	1.16E-03
65.4	1.76E-03	.236E-03	.266E-03	65.0	1.77E-03
70.4	1.67E-03	.255E-03	.280E-03	70.0	1.68E-03

EP=29.8 MEV. EX= 3.285 MEV.

3A138(P,P') 2\*

			EP=29.8 MEV.	EX= 3.339 MEV.	
ANG(CM) (DEG)	DSIGMA(CM) (MB/SR)	STAT.ERR. (MB/SR)	TOTAL ERR. (MB/SR)	ANG(LAB) (DEG)	DSIGMA(LAB) (MB/SR)
25.2	2.34E+01	.110E+01	.197E+01	25.0	2.37E+01
30.2	1.68E+01	.046E+01	.126E+01	30.0	1.71E+01
35.3	5.86E+02	.218E+02	.465E+02	35.0	5.94E+02
40.3	3.37E+02	.409E+02	.472E+02	40.0	3.41E+02
45.3	6.37E+02	.224E+02	.499E+02	45.0	6.44E+02
50.3	6.61E+02	.440E+02	.638E+02	50.0	6.58E+02
55.4	4.93E+02	.284E+02	.447E+02	55.0	4.97E+02
60.4	3.69E+02	.243E+02	.355E+02	60.0	3.72E+02
65.4	2.22E+02	.162E+02	.224E+02	65.0	2.23E+02
70.4	1.96E+02	.059E+02	.149E+02	70.0	1.97E+02
80.4	1.86E+02	.130E+02	.184E+02	80.0	1.87E+02

3A138(P,P') 2+

		EP=29.8 MEV.		EX= 3.368 MEV.	
ANG(CM) (DEG)	DSIGMA(CM) (MB/SR)	STAT.ERR. (MB/SR)	TOTAL ERR. (MB/SR)	ANG(LAB) (DEG)	DSIGMA(LAB) (MB/SR)
25.2	2.71E-01	.117E-01	.223E-01	25.0	2.75E-01
30.2	1.81E-01	.047E-01	.135E-01	30.0	1.84E-01
35.3	7.66E-02	.250E-02	.591E-02	35.0	7.76E-02
40.3	5.00E-02	.509E-02	.618E-02	40.0	5.07E-02
45.3	7.27E-02	.251E-02	.572E-02	45.0	7.36E-02
50.3	7.48E-02	.479E-02	.710E-02	50.0	7.56E-02
55.4	5.20E-02	.307E-02	.476E-02	55.0	5.25E-02
60.4	4.09E-02	.269E-02	.393E-02	60.0	4.12E-02
65.4	2.46E-02	.179E-02	.248E-02	65.0	2.47E-02
70.4	2.26E-02	.067E-02	.172E-02	70.0	2.28E-02
80.4	1.86E-02	.121E-02	.177E-02	80.0	1.86E-02



BA138(P,P') (6+)

		EP=29.8 MEV.		EX= 2.201 MEV.	
ANG(CM) (DEG)	DSIGMA(CM) (MB/SR)	STAT.ERR. (MB/SR)	TOTAL ERR. (MB/SR)	ANG(LAB) (DEG)	DSIGMA(LAB) (MB/SR)
20.2	4.78E-02	.839E-02	.903E-02	20.0	4.85E-02
30.2	2.86E-02	.256E-02	.325E-02	30.0	2.30E-02
35.3	2.44E-02	.266E-02	.316E-02	35.0	2.47E-02
40.3	2.42E-02	.286E-02	.333E-02	40.0	2.45E-02
45.3	1.90E-02	.285E-02	.315E-02	45.0	1.92E-02
50.3	1.44E-02	.264E-02	.283E-02	50.0	1.46E-02
55.4	2.15E-02	.273E-02	.312E-02	55.0	2.17E-02
65.4	1.43E-02	.195E-02	.219E-02	65.0	1.44E-02
80.4	1.09E-02	.083E-02	.112E-02	80.0	1.09E-02

# SM144(P,P) ELASTIC CROSS SECTION

EP=30.0 MEV. EX= 000 MEV.					
ANG(CM) (DEG)	DSIGMA(CM) (MB/SR)	STAT.ERR. (MB/SR)	TOTAL ERR. (MB/SR)	ANG(LAB) (DEG)	DSIGMA(LAB) (MB/SR)
15.1	1.26E+04	.035E+04	.052E+04	15.0	1.28E+04
20.1	4.37E+03	.078E+03	.152E+03	20.0	4.43E+03
25.2	1.55E+03	.015E+03	.049E+03	25.0	1.57E+03
30.2	6.41E+02	.067E+02	.204E+02	30.0	6.49E+02
35.2	2.66E+02	.028E+02	.085E+02	35.0	2.59E+02
40.3	7.65E+01	.078E+01	.242E+01	40.0	7.73E+01
42.8	5.03E+01	.056E+01	.161E+01	42.5	5.08E+01
45.3	5.20E+01	.051E+01	.164E+01	45.0	5.25E+01
47.8	6.02E+01	.061E+01	.191E+01	47.5	6.08E+01
50.3	7.07E+01	.057E+01	.220E+01	50.0	7.14E+01
55.3	6.43E+01	.064E+01	.203E+01	55.0	6.48E+01
60.4	3.38E+01	.034E+01	.107E+01	60.0	3.40E+01
65.4	7.80E+00	.099E+00	.254E+00	65.0	7.85E+00
67.9	3.86E+00	.024E+00	.118E+00	67.5	3.88E+00
70.4	4.36E+00	.046E+00	.139E+00	70.0	4.38E+00
75.4	1.07E+01	.014E+01	.035E+01	75.0	1.07E+01
80.4	1.29E+01	.014E+01	.041E+01	80.0	1.29E+01
85.4	8.72E+00	.112E+00	.285E+00	85.0	8.74E+00
90.4	3.53E+00	.039E+00	.113E+00	90.0	3.53E+00
95.4	1.38E+00	.011E+00	.043E+00	95.0	1.37E+00
100.4	1.74E+00	.015E+00	.054E+00	100.0	1.74E+00
105.4	2.86E+00	.024E+00	.089E+00	105.0	2.85E+00
110.4	2.91E+00	.017E+00	.089E+00	110.0	2.90E+00
115.4	2.00E+00	.010E+00	.061E+00	115.0	1.99E+00

SM144(P,P') 2+

		EP=29.9 MEV.		EX= 1.661 MEV.			
ANG(CM) (DEG)	DSIGMA(CM) (MB/SR)	STAT.ERR. (MB/SR)	TOTAL ERR. (MB/SR)	ANG(LAB) (DEG)	DSIGMA(LAB) (MB/SR)		
12.1	1.30E+00	.042E+00	.100E+00	12.0	1.32E+00		
16.6	1.70E+00	.060E+00	.133E+00	16.5	1.72E+00		
20.1	2.48E+00	.021E+00	.175E+00	20.0	2.52E+00		
25.2	2.88E+00	.046E+00	.207E+00	25.0	2.91E+00		
30.2	1.80E+00	.017E+00	.127E+00	30.0	1.82E+00		
35.2	8.50E+01	.098E+01	.603E+01	35.0	8.51E+01		
37.8	6.71E+01	.127E+01	.487E+01	37.5	6.79E+01		
40.3	6.12E+01	.179E+01	.464E+01	40.0	6.19E+01		
45.3	7.35E+01	.088E+01	.522E+01	45.0	7.42E+01		
47.8	6.47E+01	.129E+01	.471E+01	47.5	6.53E+01		
57.4	3.69E+01	.085E+01	.272E+01	57.0	3.71E+01		
65.4	2.59E+01	.036E+01	.185E+01	65.0	2.51E+01		
67.4	2.87E+01	.065E+01	.211E+01	67.0	2.88E+01		
70.4	2.60E+01	.030E+01	.185E+01	70.0	2.62E+01		
75.4	1.80E+01	.034E+01	.130E+01	75.0	1.80E+01		
80.4	1.18E+01	.023E+01	.085E+01	80.0	1.18E+01		
85.4	1.19E+01	.025E+01	.087E+01	85.0	1.19E+01		
90.4	1.31E+01	.032E+01	.097E+01	90.0	1.31E+01		
95.4	1.04E+01	.025E+01	.077E+01	95.0	1.04E+01		
100.4	7.45E+02	.252E+02	.579E+02	100.0	7.43E+02		
105.4	5.67E+02	.202E+02	.445E+02	105.0	5.65E+02		
110.4	6.20E+02	.205E+02	.480E+02	110.0	6.17E+02		

SM144(P,P') 30

		EP=29.9 MEV.		EX= 1.811 MEV.		
ANG(CM) (DEG)	DSIGMA(CM) (MB/SR)	STAT.ERR. (MB/SR)	TOTAL ERR. (MB/SR)	ANG(LAB) (DEG)	DSIGMA(LAB) (MB/SR)	
12.1	6.20E+01	.197E+01	.477E+01	12.0	6.29E+01	
16.6	1.02E+00	.045E+00	.084E+00	16.5	1.03E+00	
17.6	7.78E+01	.305E+01	.624E+01	17.5	7.89E+01	
20.1	1.53E+00	.016E+00	.109E+00	20.0	1.56E+00	
25.2	3.59E+00	.053E+00	.257E+00	25.0	3.64E+00	
30.2	4.86E+00	.031E+00	.342E+00	30.0	4.92E+00	
35.2	5.05E+00	.027E+00	.355E+00	35.0	5.11E+00	
37.8	4.45E+00	.037E+00	.314E+00	37.5	4.50E+00	
40.3	3.43E+00	.047E+00	.245E+00	40.0	3.47E+00	
45.3	2.03E+00	.015E+00	.143E+00	45.0	2.05E+00	
47.8	1.57E+00	.021E+00	.112E+00	47.5	1.59E+00	
50.3	1.38E+00	.012E+00	.098E+00	50.0	1.40E+00	
57.4	1.53E+00	.018E+00	.109E+00	57.0	1.55E+00	
67.4	1.34E+00	.015E+00	.095E+00	67.0	1.35E+00	
70.4	1.17E+00	.007E+00	.082E+00	70.0	1.18E+00	
75.4	8.29E+01	.075E+01	.585E+01	75.0	8.33E+01	
80.4	5.96E+01	.052E+01	.421E+01	80.0	5.98E+01	
85.4	4.84E+01	.051E+01	.342E+01	85.0	4.84E+01	
90.4	4.74E+01	.062E+01	.338E+01	90.0	4.74E+01	
95.4	4.83E+01	.054E+01	.342E+01	95.0	4.82E+01	
100.4	4.10E+01	.059E+01	.293E+01	100.0	4.09E+01	
105.4	3.15E+01	.048E+01	.226E+01	105.0	3.14E+01	
110.4	2.26E+01	.039E+01	.163E+01	110.0	2.25E+01	

SM144(P,P1) 4+

ANG(CM) (DEG)	DSIGMA(CM) (MB/SR)	STAT.ERR. (MB/SR)	TOTAL ERR. (MB/SR)	EX. 2.191 MEV.	DSIGMA(LAB) (MB/SR)
12.1	6.25E-01	.100E-01	.49E-01	12.0	6.34E-01
17.6	4.80E-01	.133E-01	.361E-01	17.5	4.87E-01
20.1	3.98E-01	.093E-01	.294E-01	20.0	4.03E-01
25.2	4.10E-01	.123E-01	.312E-01	25.0	4.15E-01
30.2	3.70E-01	.099E-01	.277E-01	30.0	3.75E-01
35.2	3.86E-01	.038E-01	.273E-01	35.0	3.91E-01
40.3	3.42E-01	.237E-01	.337E-01	40.0	3.46E-01
45.3	3.01E-01	.037E-01	.214E-01	45.0	3.04E-01
50.3	2.02E-01	.067E-01	.156E-01	50.0	2.04E-01
55.3	1.35E-01	.046E-01	.105E-01	55.0	1.36E-01
65.4	1.13E-01	.023E-01	.082E-01	65.0	1.13E-01
75.4	9.28E-02	.269E-02	.703E-02	75.0	9.31E-02
80.4	7.54E-02	.064E-02	.532E-02	80.0	7.56E-02
85.4	5.42E-02	.167E-02	.415E-02	85.0	5.43E-02
95.4	3.99E-02	.270E-02	.388E-02	95.0	3.98E-02

SM144(P,P1) (6+) DOUBLET

EP=29.9 MEV. EX= 2.324 MEV.						
AVG(CM) (DEG)	DSIGMA(CM) (MB/SR)	STAT.ERR. (MB/SR)	TOTAL ERR. (MB/SR)	AVG(LAB) (DEG)	DSIGMA(LAB) (MB/SR)	
12.1	1.70E+01	.095E+01	.152E+01	12.0	1.73E+01	
17.6	1.35E+01	.071E+01	.118E+01	17.5	1.37E+01	
20.1	1.35E+01	.053E+01	.108E+01	20.0	1.36E+01	
25.2	1.25E+01	.181E+01	.201E+01	25.0	1.27E+01	
30.2	9.36E+02	.628E+02	.908E+02	30.0	9.48E+02	
35.2	6.33E+02	.218E+02	.494E+02	35.0	6.41E+02	
40.3	5.36E+02	.357E+02	.518E+02	40.0	5.42E+02	
45.3	5.06E+02	.276E+02	.449E+02	45.0	5.11E+02	
50.3	4.53E+02	.159E+02	.355E+02	50.0	4.37E+02	
55.3	5.23E+02	.118E+02	.385E+02	55.0	5.28E+02	
65.4	2.87E+02	.181E+02	.271E+02	65.0	2.89E+02	
70.4	1.49E+02	.101E+02	.145E+02	70.0	1.50E+02	
80.4	1.44E+02	.106E+02	.147E+02	80.0	1.45E+02	
85.4	1.73E+02	.090E+02	.151E+02	85.0	1.73E+02	
95.4	2.30E+02	.123E+02	.203E+02	95.0	2.30E+02	

SM144(P,P1) 2\*

		EP=29.9 MEV.		EX= 2.423 MEV.	
ANG(CM) (DEG)	DSIGMA(CM) (MB/SR)	STAT.ERR. (MB/SR)	TOTAL ERR. (MB/SR)	ANG(LAB) (DEG)	DSIGMA(LAB) (MB/SR)
12.1	4.51E-01	.086E-01	.327E-01	12.0	4.57E-01
20.1	7.33E-01	.170E-01	.540E-01	20.0	7.43E-01
25.2	9.58E-01	.216E-01	.705E-01	25.0	9.71E-01
30.2	6.30E-01	.316E-01	.543E-01	30.0	6.39E-01
35.2	2.86E-01	.097E-01	.222E-01	35.0	2.89E-01
40.3	2.12E-01	.044E-01	.155E-01	40.0	2.14E-01
45.3	2.98E-01	.100E-01	.231E-01	45.0	3.01E-01
50.3	2.69E-01	.069E-01	.201E-01	50.0	2.72E-01
55.4	2.32E-01	.072E-01	.177E-01	55.0	2.34E-01
60.4	1.48E-01	.066E-01	.123E-01	60.0	1.49E-01
65.4	1.28E-01	.023E-01	.092E-01	65.0	1.29E-01
70.4	1.07E-01	.044E-01	.087E-01	70.0	1.07E-01
80.4	6.46E-02	.129E-02	.470E-02	80.0	6.48E-02
85.4	6.70E-02	.187E-02	.505E-02	85.0	6.71E-02
95.4	4.81E-02	.166E-02	.375E-02	95.0	4.80E-02

SM144(P,P') 4\*

ANG(CM) (DEG)	DSIGMA(CM) (MB/SR)	STAT.ERR. (MB/SR)	TOTAL ERR. (MB/SR)	ANG(LAB) (DEG)	DSIGMA(LAB) (MB/SR)
12.1	2.69E-01	.109E-01	.218E-01	12.0	2.73E-01
20.1	1.79E-01	.035E-01	.130E-01	20.0	1.81E-01
25.2	1.60E-01	.094E-01	.146E-01	25.0	1.62E-01
30.2	1.51E-01	.030E-01	.110E-01	30.0	1.53E-01
35.2	1.52E-01	.069E-01	.126E-01	35.0	1.53E-01
40.3	1.32E-01	.074E-01	.118E-01	40.0	1.33E-01
45.3	1.38E-01	.032E-01	.102E-01	45.0	1.40E-01
50.3	8.33E-02	.168E-02	.607E-02	50.0	8.41E-02
55.4	6.24E-02	.302E-02	.531E-02	55.0	6.30E-02
60.4	4.98E-02	.101E-02	.363E-02	60.0	5.01E-02
70.4	5.08E-02	.365E-02	.510E-02	70.0	5.10E-02
75.4	5.08E-02	.233E-02	.425E-02	75.0	5.10E-02
85.4	3.88E-02	.102E-02	.290E-02	85.0	3.88E-02
95.4	2.29E-02	.121E-02	.200E-02	95.0	2.28E-02

EP=29.9 MEV. EX= 2.588 MEV.



SM144(P,P1) 2\*

		EP=29.9 MEV.		EX= 2.800 MEV.			
ANG(CM)	DSIGMA(CM)	STAT.ERR.	TOTAL ERR.	ANG(LAB)	DSIGMA(LAB)		
(DEG)	(MB/SR)	(MB/SR)	(MB/SR)	(DEG)	(MB/SR)		
12.1	5.79E-02	.507E-02	.649E-02	12.0	5.87E-02		
20.1	2.17E-01	.060E-01	.163E-01	20.0	2.20E-01		
25.2	3.34E-01	.190E-01	.301E-01	25.0	3.39E-01		
30.2	2.03E-01	.077E-01	.161E-01	30.0	2.05E-01		
35.2	7.57E-02	.521E-02	.743E-02	35.0	7.67E-02		
40.3	4.12E-02	.450E-02	.534E-02	40.0	4.17E-02		
45.3	6.82E-02	.556E-02	.733E-02	45.0	6.90E-02		
50.3	6.29E-02	.595E-02	.741E-02	50.0	6.36E-02		
55.4	5.42E-02	.348E-02	.515E-02	55.0	5.47E-02		
60.4	2.82E-02	.262E-02	.328E-02	60.0	2.84E-02		
65.4	1.33E-02	.118E-02	.151E-02	65.0	1.34E-02		
75.4	1.17E-02	.090E-02	.122E-02	75.0	1.18E-02		
80.4	1.06E-02	.125E-02	.145E-02	80.0	1.06E-02		

SM144(P,P1) UNKNOWN

AVG(CM) (DEG)	DSIGMA(CM) (MB/SR)	STAT.ERR. (MB/SR)	TOTAL ERR. (MB/SR)	ANG(LAB) (DEG)	DSIGMA(LAB) (MB/SR)	EP=29.9 MEV. EX# 2.826 MEV.
12.1	3.05E+01	.060E+01	.222E+01	12.0	3.09E+01	
20.1	3.71E+01	.075E+01	.271E+01	20.0	3.77E+01	
25.2	4.45E+01	.207E+01	.374E+01	25.0	4.51E+01	
30.2	4.18E+01	.107E+01	.312E+01	30.0	4.23E+01	
35.2	3.97E+01	.102E+01	.296E+01	35.0	4.02E+01	
40.3	4.00E+01	.085E+01	.292E+01	40.0	4.04E+01	
45.3	4.92E+01	.160E+01	.380E+01	45.0	4.97E+01	
50.3	4.12E+01	.145E+01	.323E+01	50.0	4.16E+01	
55.4	3.39E+01	.084E+01	.252E+01	55.0	3.42E+01	
60.4	2.14E+01	.066E+01	.164E+01	60.0	2.16E+01	
65.4	1.43E+01	.026E+01	.103E+01	65.0	1.44E+01	
75.4	1.11E+01	.021E+01	.080E+01	75.0	1.11E+01	
80.4	9.79E+02	.302E+02	.749E+02	80.0	9.82E+02	
85.4	7.28E+02	.465E+02	.690E+02	85.0	7.29E+02	
95.4	6.89E+02	.283E+02	.559E+02	95.0	6.88E+02	

SM144(P,P1) 4\*

		EP=29.9 MEV.		EX= 2.883 MEV.	
ANG(CM)	DSIGMA(CM)	STAT.ERR.	TOTAL ERR.	ANG(LAB)	DSIGMA(LAB)
(DEG)	(MB/SR)	(MB/SR)	(MB/SR)	(DEG)	(MB/SR)
12.1	3.22E-01	.115E-01	.253E-01	12.0	3.27E-01
20.1	2.36E-01	.061E-01	.176E-01	20.0	2.40E-01
25.2	2.17E-01	.122E-01	.195E-01	25.0	2.19E-01
30.2	2.04E-01	.077E-01	.162E-01	30.0	2.07E-01
35.2	2.04E-01	.074E-01	.161E-01	35.0	2.07E-01
40.3	1.74E-01	.067E-01	.139E-01	40.0	1.76E-01
45.3	1.75E-01	.098E-01	.156E-01	45.0	1.76E-01
50.3	1.24E-01	.078E-01	.117E-01	50.0	1.26E-01
55.4	9.03E-02	.416E-02	.757E-02	55.0	9.11E-02
60.4	7.85E-02	.423E-02	.693E-02	60.0	7.91E-02
65.4	6.60E-02	.178E-02	.495E-02	65.0	6.55E-02
75.4	4.88E-02	.156E-02	.375E-02	75.0	4.90E-02
80.4	4.06E-02	.199E-02	.347E-02	80.0	4.07E-02
95.4	3.04E-02	.207E-02	.297E-02	95.0	3.04E-02

SM144(P,P') 4+

		EP=29.9 MEV.		EX= 3.020 MEV.	
ANG(CM) (DEG)	DSIGMA(CM) (MB/SR)	STAT.ERR. (MB/SR)	TOTAL ERR. (MB/SR)	ANG(LAB) (DEG)	DSIGMA(LAB) (MB/SR)
12.1	2.54E-01	.096E-01	.202E-01	12.0	2.58E-01
20.1	1.75E-01	.080E-01	.146E-01	20.0	1.77E-01
25.2	2.08E-01	.148E-01	.207E-01	25.0	2.11E-01
30.2	1.94E-01	.018E-01	.137E-01	30.0	1.96E-01
35.2	2.12E-01	.068E-01	.163E-01	35.0	2.15E-01
40.3	2.01E-01	.076E-01	.160E-01	40.0	2.04E-01
45.3	1.58E-01	.010E-01	.111E-01	45.0	1.60E-01
50.3	8.76E-02	.153E-02	.632E-02	50.0	8.85E-02
55.4	5.16E-02	.190E-02	.408E-02	55.0	5.20E-02
60.4	3.53E-02	.131E-02	.280E-02	60.0	3.55E-02
65.4	3.07E-02	.064E-02	.224E-02	65.0	3.09E-02
75.4	2.88E-02	.228E-02	.305E-02	75.0	2.89E-02
80.4	2.28E-02	.018E-02	.161E-02	80.0	2.28E-02
85.4	1.38E-02	.298E-02	.313E-02	85.0	1.39E-02
95.4	1.79E-02	.112E-02	.168E-02	95.0	1.78E-02

SM144(P,P1) (7-)

		EP=29.9 MEV.		EX= 3.123 MEV.	
ANG(CM) (DEG)	DSIGMA(CM) (MB/SR)	STAT.ERR. (MB/SR)	TOTAL ERR. (MB/SR)	ANG(LAB) (DEG)	DSIGMA(LAB) (MB/SR)
25.2	9.19E+02	.712E+02	.960E+02	25.0	9.32E+02
30.2	7.35E+02	.264E+02	.578E+02	30.0	7.44E+02
35.2	6.78E+02	.128E+02	.492E+02	35.0	6.87E+02
40.3	6.85E+02	.307E+02	.570E+02	40.0	6.93E+02
45.3	7.81E+02	.279E+02	.614E+02	45.0	7.90E+02
50.3	7.60E+02	.256E+02	.590E+02	50.0	7.68E+02
55.4	7.63E+02	.284E+02	.605E+02	55.0	7.70E+02
60.4	6.10E+02	.317E+02	.532E+02	60.0	6.14E+02
65.4	5.06E+02	.123E+02	.375E+02	65.0	5.10E+02
70.4	4.50E+02	.278E+02	.420E+02	70.0	4.72E+02
75.4	3.37E+02	.109E+02	.260E+02	75.0	3.38E+02
80.4	2.77E+02	.123E+02	.230E+02	80.0	2.78E+02
85.4	2.02E+02	.151E+02	.207E+02	85.0	2.03E+02
95.4	1.70E+02	.161E+02	.200E+02	95.0	1.70E+02

SM144(P,P1) UNKNOWN

		EP=29.9 MEV.		EX= 3.196 MEV.	
ANG(CM) (DEG)	DSIGMA(CM) (MB/SR)	STAT.ERR. (MB/SR)	TOTAL ERR. (MB/SR)	ANG(LAB) (DEG)	DSIGMA(LAB) (MB/SR)
25.2	5.30E-02	.956E-02	1.026E-02	25.0	5.38E-02
30.2	4.33E-02	.227E-02	.379E-02	30.0	4.39E-02
35.2	3.99E-02	.238E-02	.367E-02	35.0	4.04E-02
40.3	3.86E-02	.411E-02	.492E-02	40.0	3.91E-02
45.3	5.37E-02	.224E-02	.438E-02	45.0	5.43E-02
50.3	5.94E-02	.086E-02	.425E-02	50.0	6.00E-02
55.4	4.95E-02	.255E-02	.431E-02	55.0	5.00E-02
60.4	4.52E-02	.168E-02	.359E-02	60.0	4.56E-02
65.4	3.06E-02	.104E-02	.238E-02	65.0	3.08E-02
70.4	2.68E-02	.081E-02	.204E-02	70.0	2.69E-02
80.4	1.42E-02	.164E-02	.192E-02	80.0	1.42E-02
85.4	1.24E-02	.125E-02	.152E-02	85.0	1.24E-02
95.4	1.11E-02	.091E-02	.119E-02	95.0	1.10E-02

SM144(P,P1) 3-

		EP=29.9 MEV.		EX= 3.227 MEV.	
ANG(CM) (DEG)	DSIGMA(CM) (MB/SR)	STAT.ERR. (MB/SR)	TOTAL ERR. (MB/SR)	ANG(LAB) (DEG)	DSIGMA(LAB) (MB/SR)
25.2	3.70E-02	.958E-02	.992E-02	25.0	3.75E-02
30.2	3.66E-02	.199E-02	.324E-02	30.0	3.71E-02
35.2	2.96E-02	.202E-02	.290E-02	35.0	3.00E-02
40.3	1.85E-02	.297E-02	.325E-02	40.0	1.88E-02
45.3	1.11E-02	.085E-02	.115E-02	45.0	1.12E-02
50.3	7.87E-03	.669E-03	.866E-03	50.0	7.94E-03
55.4	8.65E-03	1.803E-03	1.901E-03	55.0	8.72E-03
60.4	8.44E-03	.833E-03	1.071E-03	60.0	8.50E-03
65.4	8.66E-03	.716E-03	.938E-03	65.0	8.72E-03
70.4	7.91E-03	.532E-03	.768E-03	70.0	7.95E-03

SM144(P,P') UNKNOWN

EP=29.9 MEV. EX= 3.266 MEV.

ANG(CM) (DEG)	DSIGMA(CM) (MB/SR)	STAT.ERR. (MB/SR)	TOTAL ERR. (MB/SR)	ANG(LAB) (DEG)	DSIGMA(LAB) (MB/SR)
30.2	6.42E-03	1.158E-03	1.242E-03	30.0	6.51E-03
35.2	1.09E-02	.146E-02	.165E-02	35.0	1.11E-02
40.3	1.24E-02	.261E-02	.275E-02	40.0	1.25E-02
45.3	9.33E-03	1.123E-03	1.299E-03	45.0	9.43E-03
50.3	1.20E-02	.190E-02	.208E-02	50.0	1.21E-02
55.4	1.38E-02	.231E-02	.250E-02	55.0	1.40E-02
60.4	6.28E-03	2.121E-03	2.166E-03	60.0	6.32E-03
65.4	6.88E-03	1.558E-03	1.631E-03	65.0	6.93E-03
70.4	8.26E-03	.523E-03	.779E-03	70.0	8.30E-03
85.4	5.51E-03	1.468E-03	1.518E-03	85.0	5.52E-03
95.4	2.44E-03	.663E-03	.684E-03	95.0	2.44E-03



SM144(P,P1) 6+

		EP=29.9 MEV.		EX= 3.308 MEV.	
ANG(CM) (DEG)	DSIGMA(CM) (MB/SR)	STAT.ERR. (MB/SR)	TOTAL ERR. (MB/SR)	ANG(LAB) (DEG)	DSIGMA(LAB) (MB/SR)
17.6	4.91E+02	.662E+02	.746E+02	17.5	4.99E+02
30.2	3.97E+02	.294E+02	.404E+02	30.0	4.02E+02
35.2	3.32E+02	.224E+02	.323E+02	35.0	3.36E+02
40.3	3.04E+02	.375E+02	.432E+02	40.0	3.07E+02
45.3	3.84E+02	.194E+02	.331E+02	45.0	3.88E+02
50.3	3.01E+02	.274E+02	.345E+02	50.0	3.04E+02
55.4	3.00E+02	.296E+02	.363E+02	55.0	3.02E+02
60.4	1.91E+02	.138E+02	.192E+02	60.0	1.93E+02
65.4	1.37E+02	.181E+02	.205E+02	65.0	1.38E+02
70.4	1.16E+02	.061E+02	.101E+02	70.0	1.17E+02
85.4	6.61E+03	1.096E+03	1.190E+03	85.0	6.62E+03
95.4	9.77E+03	.907E+03	1.136E+03	95.0	9.76E+03

MICHIGAN STATE UNIVERSITY LIBRARIES



3 1293 02546 9374